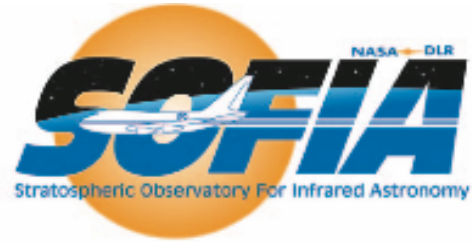

Early Science Test Report: HIPO Ground Operations

SCI-US-TRP-SV03-2012

Date: May 30, 2009
Revision: -

DFRC
Dryden Flight Research Center
Edwards, CA 93523

ARC
Ames Research Center
Moffett Field, CA 94035

German Space Agency, DLR
Deutsches Zentrum für Luft und Raumfahrt

Early Science Test Report: HIPO Ground Operations SCI-US-TRP-SV03-2012

PREPARED BY:

Sybil Adams, USRA SOFIA Mission Operations Specialist	Date
Tom Bida, Lowell Observatory Instrument Scientist	Date
Peter Collins, Lowell Observatory Software Developer	Date
Edward Dunham, HIPO Principal Investigator, Lowell Obs.	Date
Randy Grashuis, USRA SOFIA Mission Operations Specialist	Date
Franziska Harms, DSI Engineer	Date
Holger Jakob, DSI Engineer	Date
Ulrich Lampater, DSI Researcher	Date
Allan Meyer, USRA SOFIA Associate Scientist	Date
Andreas Reinacher, DSI Engineer, Chopper/SMM	Date

Jürgen Wolf, DSI Senior Research Scientist	Date

APPROVAL:

Helen J. Hall, USRA SOFIA Program Director	Date

REVISION HISTORY

REV	DATE	DESCRIPTION
-	5/30/09	Initial Release

Early Science Test Report: HIPO Ground Operations

Version 2.0

SCI-US-TRP-SV03-2012

Table of Contents:

Executive Summary:

A series of ground-based tests and calibrations of the SOFIA Telescope Assembly (TA) using HIPO as a test instrument were carried out during November and December, 2008. These generally followed the procedures in the previously developed test plan, SCI-AR-TPL-PM12-2000 (November 13, 2008 version).

The tests were completed successfully in spite of a greatly compressed schedule. Five nights were available of which four were effectively used, the remaining time being lost to weather and some TA issues. There was a significant reduction in scope for the secondary mirror tests (TC-HIPO-03) as envisioned in the original test plan.

None of the suggested testing was for verification credit. In part, this decision was made in support of the on-going observatory development environment. Future testing for credit under an established configuration will be necessary. It is not envisioned that the HIPO instrument will be required for future early science tests unless first light observations necessitate the investigation and characterization of poorly understood cavity seeing effects.

Highlights of the test results include:

1. A potentially serious problem with the fine drive control system was uncovered during the execution of TC-HIPO-08 part 3. The symptom is that the telescope pointing jumps from place to place when the TA is inertially stabilized (i.e. not tracking) and sufficient mechanical disturbance is applied. This requires further investigation and should be tracked at the Program level.
2. There is an operational issue regarding the manner in which gyro drift is compensated. With proper communication during planning and execution of observations this will not be problematic. It is essential that telescope operators and observers are aware of this situation.
3. At chopper frequencies of greater than 5 Hz and chopper amplitudes of 10 arc-minutes, the chopper settling time is greater than 35% of the overall chopper duty cycle. A retuning of the chopping secondary servo system is required if it is necessary to improve the chopper efficiency for early science.
4. The aperture elevation angle should be set to a position 0.5º higher than the TA elevation angle. There may be a small variation in this value with elevation angle.
5. The optical and gyro alignments are good enough for operational use but could be improved. It may be desirable to tweak the gyro alignment prior to early science. This can be accomplished using the FPI now that the position of the center of the SI flange has been mapped to the FPI.

Introduction:

A series of ground-based tests and calibrations of the SOFIA Telescope Assembly (TA) using HIPO as a test instrument were carried out during November and December, 2008. These tests were executed, by and large, according to the previously developed test plan, SCI-AR-TPL-PM12-2000 (November 13, 2008 version), to which the reader is referred.

The idea of executing tests for formal V&V credit was incorporated into the test plan but this idea was abandoned at the Test Readiness Review since most of the TA systems were still under development to various degrees.

In addition, the schedule during the test period was severely impacted by on-going delays in the development and delivery of the aircraft aperture door controller hardware and software.

In the end the HIPO test work was compressed into a much shorter period than originally planned and many tests were significantly reduced in scope to accommodate the required reductions in the duration of planned testing activities.

Scope:

The original scope of this document was limited to TA performance as required for Early Science and does not include performance requirements relevant to the Early Science configuration of the MCCS hardware and software.

Purpose:

This document describes the tests performed, data obtained, the analysis of the data, the results of each test, and the suggested next steps in the progression toward Early Science.

TC-HIPO-01: HIPO to SI Flange Coordinate Transformation and HIPO Internal Flexure Measurement

Introduction:

This test determines the precise coordinate transformation between HIPO red channel pixel coordinates and the coordinate system centered on the SI flange and oriented with respect to the SI mounting pins that are at top and bottom when the TA is at an elevation angle of 40 degrees. Furthermore this test determines the internal flexure of the HIPO instrument. This flexure as a function of the telescope's elevation is apparent in TC-HIPO-02. This measurement is also a prerequisite to TC-HIPO-06, the Gyro Alignment test.

The mounting of the HIPO flange physically determines the center of the SI flange and, hence, coincides with the origin of the TA reference frame (TARF). The HIPO mounting plate has a close-fitting hole for the top pin and a vertical slot for the bottom pin, so the zero point of the coordinate system is defined with respect to the top pin and the orientation of the coordinate system is defined by the line from top pin to bottom pin.

The test was carried out on 18 November (19 November UT) according to the test plan.

Data Acquired:

A series of single frames were obtained using the HIPO red side optics focused on the flange fiducial. These images were obtained at a number of TA elevation angles to check for internal flexure in HIPO as well as for defining the location of the center of the flange in HIPO pixel coordinates. The detailed data are shown in Table 1-1 below. This was copied and pasted from the notes taken during the test. The interested reader should consult the notes for additional detail.

Although the CCD was stable in temperature, there is a trend with time having very low amplitude in the Y direction that suggests that some other components in the CCD supporting structure may not have quite achieved thermal equilibrium.

Data Analysis:

Centroids were obtained with *iui* on the central hole in the flange fiducial hole pattern, which marks the center of the SI mounting flange (within the machining tolerances) as well as the top center, bottom center, left middle, and right middle holes for definition of the rotation of the HIPO red CCD pixel grid relative to the SI flange coordinate system as described in the Introduction section.

Results:

The results given in the data table above are shown below in graphical form.

The top two frames of the figure show the X and Y (HIPO pixel coordinates) of the central hole in the flange fiducial pattern as a function of telescope elevation angle. The Y position shows a trend with time, the highest point being the earliest one and the lowest being the latest. The HIPO pixels map to approximately 0.325 arcsec on the sky, so the 0.6 pixel X motion corresponds to a little less than ±0.1 arcsec mapped to the sky.

Table 1-1: Flange Fiducial Results

OS	Nom El	Act. El.	Xc	Yc	Rot1	Rot2
2	35	34.95	542.70	480.43	0.182	0.191
3	35	34.95	542.69	480.37	0.182	0.192
4	35	34.95	542.69	480.37	0.182	0.192
5	35	34.95	542.69	480.37	0.182	0.192
6	60	60.16	543.03	480.33	0.186	0.195
7	60	60.16	543.03	480.33	0.186	0.195
8	60	60.16	543.04	480.33	0.186	0.195
9	50	49.85	542.89	480.25	0.185	0.195
10	50	49.85	542.88	480.25	0.185	0.195
11	50	49.85	542.89	480.26	0.185	0.194
12	40	40.11	542.74	480.25	0.183	0.194
13	40	40.11	542.74	480.25	0.183	0.194
14	40	40.11	542.74	480.26	0.183	0.193
15	30*	29.79	542.58	480.25	0.181	0.192
16	30*	29.79	542.58	480.25	0.181	0.192
17	30*	29.79	542.57	480.25	0.181	0.192
18	20*	20.05	542.45	480.25	0.179	0.190
19	20*	20.05	542.45	480.25	0.179	0.190
20	20*	20.05	542.45	480.25	0.179	0.190
21	20	20.05	542.45	480.25	0.179	0.190
22	20	20.05	542.45	480.24	0.179	0.190
23	20	20.05	542.45	480.24	0.179	0.190
24	30	29.79	542.60	480.24	0.181	0.192
25	30	29.79	542.60	480.23	0.181	0.192
26	30	29.79	542.60	480.24	0.181	0.192
27	40	40.11	542.76	480.22	0.183	0.194
28	40	40.11	542.77	480.22	0.183	0.194
29	40	40.11	542.78	480.22	0.183	0.194
30	50	49.85	542.91	480.21	0.185	0.195
31	50	49.85	542.91	480.20	0.185	0.194
32	50	49.85	542.91	480.20	0.185	0.195
33	60	60.16	542.99	480.18	0.187	0.196
34	60	60.16	542.99	480.17	0.187	0.196
35	60	60.16	542.99	480.18	0.187	0.196

* The comment in the headers for OS 15-20 incorrectly indicates an elevation of 40 degrees.

The bottom two frames show the angular offset in degrees of the HIPO pixel grid relative to the flange fiducial hole pattern. The lower left frame shows the angular offset between

the CCD rows and the rows of holes in the flange fiducial while the lower right frame shows the corresponding column angular offset. There is a deviation between the two angles that is significant compared to the noise level of the data. It is probably due to optical distortion in the red camera lens. The magnitude of this effect is 0.01° or 0.29 mrad, or 0.30 pixel across our 1K CCD grid. Neglecting this effect will result in an error on the 0.1 arcsec level.

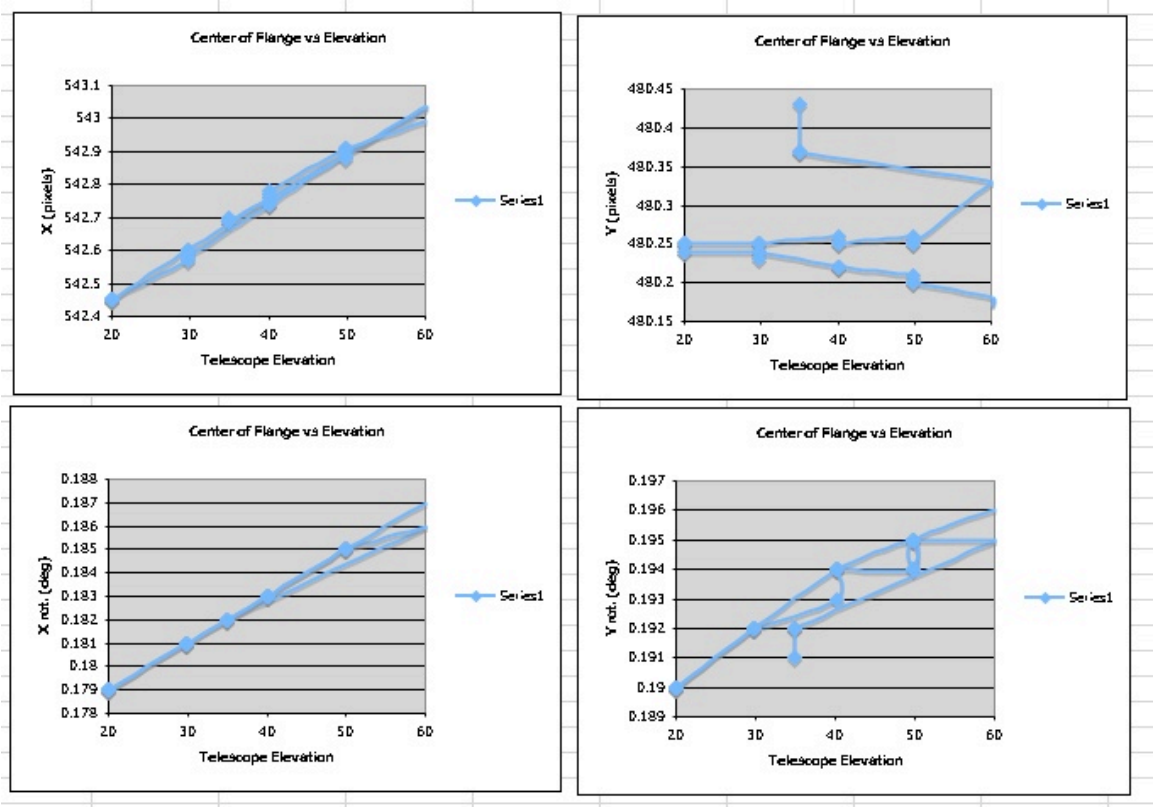

Figure 1-1: Flange fiducial test results. Note that the image scale for HIPO is approximately 0.325 arcsec/pixel. See text for discussion.

Conclusions:

We conclude that:

1. The HIPO X/Y coordinates of the location of the center of the flange are (542.8,480.2) ±1.5 pixels or about 0.5 arcsec. The uncertainty in this position is dominated by the machining tolerance stackup of the HIPO front plate, the SI flange parts, and the flange fiducial, estimated to be approximately 0.005 inch.
2. The HIPO pixel grid is misaligned with the SI flange pins by 0.19° ±0.01° in the sense that the angle between the HIPO rows and the W (or rot_V) axis of the TA is 39.81°.
3. Flexure internal to HIPO results in systematic deviations in the position of the center of the flange on the HIPO pixel grid but at the level of 0.1 arcsec.

4. Flexure internal to HIPO results in systematic deviation in the orientation of the HIPO pixel grid relative to the flange at the level of 0.1 arcsec at the edge of the 8 arcminute SOFIA field of view.

Next steps:

Since this test is an internal characterization of HIPO, no additional actions are required by the final test results. These measurements, however, factor into the analysis of test results for TC-HIPO-02 and TC-HIPO-06.

TC-HIPO-02: Pupil imaging and Door Alignment

Preface:

The test plan envisioned use of the test target for the door alignment activity. Due to the pressures of the schedule a "quick and dirty" version of the test was developed to allow the HIPO ground operations to proceed expeditiously. The results of both tests are described here.

Part 1: Quick and Dirty Aperture Alignment

Introduction:

This procedure was developed on the fly due to a scheduling problem that resulted in postponing the originally planned aperture alignment until the end of the test period. The intent of this test was to insure that we could proceed with the tests using stars, the optical alignment in particular, without blocking part of the telescope aperture with the structural aperture. The test was carried out in the hangar just prior to towing the aircraft out for the first night of line operations.

In this test the TA was set to a coarse elevation of 40.17°, where it remained for the duration of the test. The aperture was set to 40°, then 53°, and finally 27°. Images were obtained using the HIPO pupil viewing capability, and deviation from symmetry relative to the central obscuration (which was fixed at (X,Y) = (602,472)) in the 53° and 27° images indicated an offset between the aperture and TA elevation coordinate systems. Additional images were obtained with the aperture at elevation angles including the offset to verify the offset. Images at ±2.5° in LOS were also obtained to get a feel for the LOS vignetting effect. This test was not able to detect variation in the scale of the two elevation angle coordinate systems; this was left to the originally planned aperture alignment test.

Data Acquired:

All the images involved were taken on 12/10/08 UT with the I filter, a 50 ms exposure time, and a focus position of 2500 steps. The URD was out of the way at an elevation of 66.2°. HIPO Observation Sequence (OS) 23 was the first image taken with the final filter and focus position, and with the SMA at its nominal position. Table 2-1 contains the list of images used for this test. Images 24-32 were taken with the aperture assembly at 53° and three LOS positions, and 33-41 were the same but at a 27° aperture assembly elevation angle. Images 42-47 were taken at LOS=0 with the aperture at corrected high and low positions. Finally, images 48-56 were taken at the corrected aperture elevation corresponding to the TA elevation and show no evidence of the aperture in the pupil images for the ±2.5° range of LOS explored.

Figure 2-1 shows sample images taken with varying aperture elevation angles and Figure 2-2 shows images taken at varying LOS positions at an aperture elevation of 53°. The outlines of the field of view of the pupil viewing optics and the edge of the secondary

mirror are shown in the center panel of Figure 2-1. Most of the structure seen reflected in the secondary mirror is ceiling structure in the hangar.

Table 2-1: Quick and Dirty Aperture Alignment Data

OS	Aperture Elevation	LOS	X1	Y1	X2	Y2	Perp. Distance	Adopted Distance
23	40.0							
24	53.0	0	399	312	690	58	254	
25	53.0	0	402	310	672	75	254	254
26	53.0	0	366	343	683	64	253	
27	53.0	2.5	384	272	660	52	292	
28	53.0	2.5	383	274	645	64	292	292
29	53.0	2.5	374	281	656	55	292	
30	53.0	-2.5	417	349	714	67	217	
31	53.0	-2.5	419	348	702	79	216	216
32	53.0	-2.5	422	346	709	72	215	
33	27.0	0	663	717	1000	447	229	
34	27.0	0	664	718	1000	447	230	230
35	27.0	0	663	718	1000	448	230	
36	27.0	2.5	647	679	978	434	193	
37	27.0	2.5	647	679	977	434	193	193
38	27.0	2.5	647	678	976	435	192	
39	27.0	-2.5	722	723	983	493	268	
40	27.0	-2.5	719	726	988	489	268	268
41	27.0	-2.5	722	723	988	489	268	
42	27.6	0	648	745	1005	458	242	
43	27.6	0	646	743	1007	457	240	242
44	27.6	0	649	746	1011	454	243	
45	53.6	0	375	346	695	70	244	
46	53.6	0	378	344	688	76	243	243
47	53.6	0	377	345	689	75	243	
48	40.8	0						
49	40.8	0						
50	40.8	0						
51	40.8	2.5						
52	40.8	2.5						
53	40.8	2.5						
54	40.8	-2.5						
55	40.8	-2.5						
56	40.8	-2.5						

Data Analysis:

For each image showing an edge of the aperture the position of the central obscuration was estimated by eye using a circular overlay in the *ds9* image display utility as a guide. This position was unchanged throughout the test, at a location (X,Y) = (502,472). Two points along the edge of the aperture were also estimated by finding points halfway in brightness between the edge of the aperture and the adjacent area on the hangar ceiling. The perpendicular distance from the line of the aperture edge to the center of the central obscuration was then found (thanks to Allan Meyer for this calculation) and is recorded in Table 2-1. An adopted perpendicular distance for each set of three images is shown in

the last column of Table 2-1. Note that the coordinates used are in HIPO pixels, including the 8 prescan pixels.

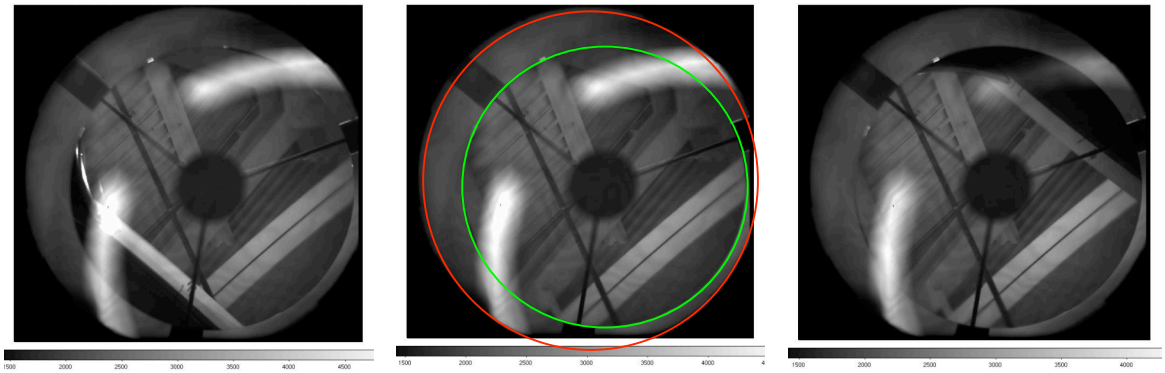

Figure 2-1. OS24, 23, and 33 (Aperture elevations 53°, 40°, and 27°, respectively) are shown from left to right. It is easy to pick out the lower edge of the aperture in OS24 (toward lower left in the left panel) and the upper edge in OS33 (upper right in the right panel). The outline of the field of view of the HIPO pupil viewing optics (red) and the secondary mirror (green) are shown in the center panel. The bright fuzzy arcs seen to the top and left are the edge of the second tertiary mirror seen through the dichroic tertiary. The aft direction is toward the upper left as can be seen from the curved aft ramp in the aperture assembly.

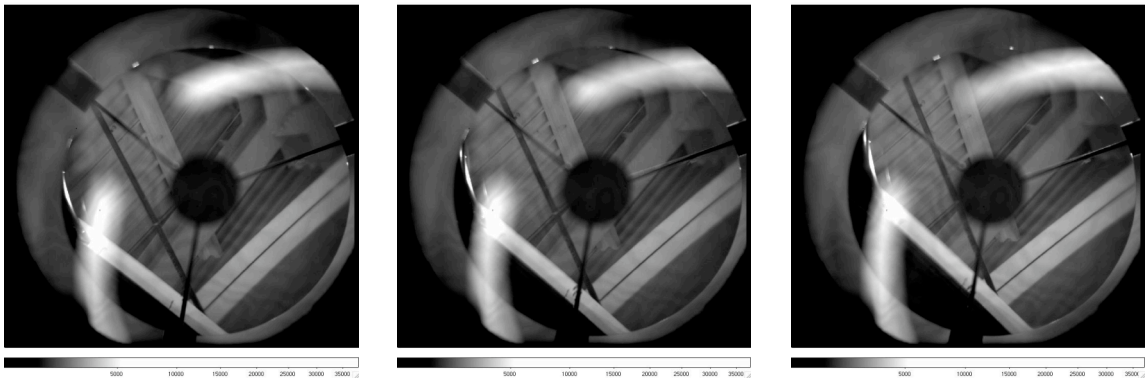

Figure 2.2. OS27, 24, and 30 (LOS = +2.5°, 0°, and -2.5°, respectively) are shown left to right in this figure. The aperture elevation is 53° in all of these images.

Results:

There is a clear asymmetry between the perpendicular distances for the 53° and 27° cases (254 vs 230 pixels). The estimated scale was 18.5 pixels per degree of aperture motion so this corresponds to an offset of half of 24/18.5 = 0.6°. This correction was applied to the aperture position for images 42-47 and the perpendicular distance became nearly the same for the low and high aperture locations. Since the TA elevation was 40.17° throughout the test the aperture elevation minus TA elevation correction is actually 0.4°.

This is a real detection in the sense that the positions of the lines and central obscuration are reproducible at a ~2 pixel level, corresponding to ~0.1°. However there may be systematic errors in the definitions of the measured points in the images so this should not be taken as a definitive result.

From the ±2.5° LOS images the LOS scale is 15.1 pixels per degree of LOS. A degree of LOS motion results in an equivalent elevation motion of 15.1/18.5=0.82°.

The fact that the aperture structure was not visible in OS51-56 (nearly aligned aperture and ±2.5° LOS) was sufficient to allow us to proceed with the remaining ground test work.

Part 2: Originally Planned Aperture Alignment

Introduction:

This test calibrates the alignment of the TA with the aircraft aperture. It provides optical imaging of the telescope pupil to reduce the likelihood that FORCAST and GREAT will encounter variable background emission due to variable vignetting by the aperture. For this HIPO test an aperture alignment mask is installed in the aircraft aperture in order to provide fiducial holes to enable a precise measurement of the relative positions of the telescope pupil and the aircraft aperture.

The mask configuration and installation is shown in Figure 2-3 below. The diameter of the fiducial hole pattern is 1016mm with 25.4mm fiducial hole sizes. The test is carried out in the hangar with the cavity door open. Note that the hole pattern is such that a) it is visible with the flight secondary mirror in place, and b) the hole pattern is not obscured for LOS rotations of the TA.

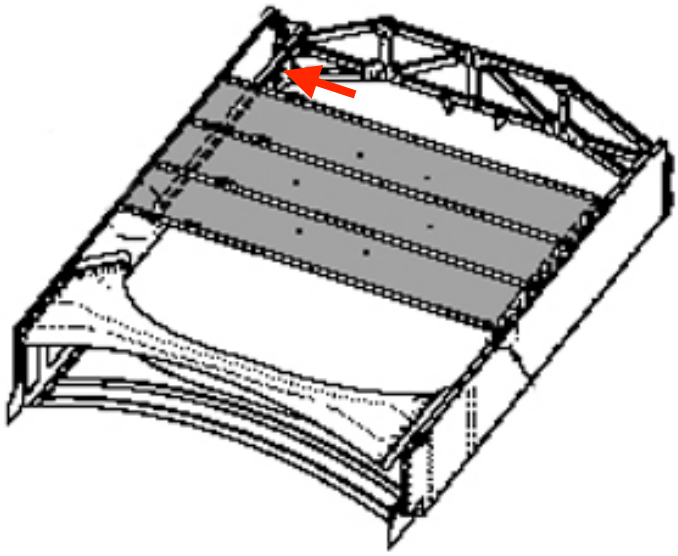

Figure 2-3. The mask is 1575mm across the aperture opening in the XEL direction, and 2895mm from top to bottom of the aperture in the EL direction. The red arrow indicates the horizontal positioning arm of the mask that centers it in the aperture fore to aft.

The TA was uncaged and centered as well as possible using the vacuum pump to manually center the VIS. It is estimated that the VIS was centered to within ~3mm axially and tangentially.

Positioning accuracy of the aperture is expected to be ~0.1º-0.2º in flight, with ~0.1º due to the size of one gear tooth on the CDDS and ~0.1º expected to be due to flexure in the fuselage and gear track when the aperture is open during flight (as per discussions with the Ames CDDS design team).

Data Acquired:

All images were taken with a HIPO focus of 1300 steps as the best compromise between getting the central obscuration in focus and not having the holes in the mask too out of focus. The I filter, 0.2 sec exposures were used with the hangar lights off in the direction the TA was pointed. No additional masking inside HIPO was required.

Table 2-2: Summary of TA/Aperture alignment data taken on Dec 15, 2008 UT .

HIPO OS	TA EL	TA XEL	TA LOS	Demanded AA EL	Achieved AA EL	AA X (pix)	AA Y (pix)	M2 X (pix)	M2 Y (pix)	ΔX (pix)	ΔY (pix)	ΔEL (pix)	ΔXEL (pix)	ΔEL (deg)	ΔXEL (deg)
14	40.0	0.0	0.0	40.0	40.04	638.9	425.2	606.7	463.9	32.2	-38.7	-9.1	49.5	-0.49	2.81
15	40.0	1.0	0.0	40.0	40.04	624.8	438.2	606.7	463.9	18.1	-25.7	-8.2	30.3	-0.44	1.72
16	40.0	3.0	0.0	40.0	40.04	599.1	459.8	606.7	463.9	-7.6	-4.1	-8.0	-3.3	-0.43	-0.18
17	40.0	3.0	0.0	42.5	42.55	628.0	494.1	606.7	463.9	21.3	30.2	36.8	-3.0	1.99	-0.17
18	40.0	3.0	0.0	37.5	37.47	569.0	424.2	606.7	463.9	-37.7	-39.7	-54.6	-3.5	-2.95	-0.20
19	40.0	3.0	0.0	39.5	39.54	593.4	452.8	606.7	463.9	-13.3	-11.1	-17.0	-3.1	-0.92	-0.18
20	40.0	3.0	0.0	40.5	40.54	604.9	466.6	606.7	463.9	-1.9	2.7	0.9	-3.1	0.05	-0.18
21	40.0	3.0	0.0	40.3	40.33	602.5	464.3	606.7	463.9	-4.3	0.4	-2.4	-3.6	-0.13	-0.20
22	40.0	2.7	0.0	40.3	40.33	606.9	460.3	606.7	463.9	0.2	-3.6	-2.6	2.5	-0.14	0.14
23	40.0	2.8	0.0	40.3	40.33	605.4	461.8	606.7	463.9	-1.3	-2.1	-2.4	0.4	-0.13	0.02
24	40.0	2.8	0.0	40.5	40.48	606.9	464.0	606.7	463.9	0.2	0.1	0.2	0.1	0.01	0.01
25	24.5	2.8	0.0	25.0	24.96	604.5	461.7	605.6	463.6	-1.1	-1.9	-2.1	0.4	-0.12	0.02
26	52.5	2.8	0.0	53.0	53.04	608.6	465.2	608.3	465.5	0.3	-0.3	0.0	0.4	0.00	0.02
27	52.5	0.0	0.0	53.0	53.04	645.8	434.7	608.3	465.5	37.5	-30.8	0.4	48.5	0.02	2.76
28	52.5	0.0	2.5	53.0	53.04	621.5	406.5	608.3	465.5	13.2	-59.0	-36.9	48.0	-1.99	2.73
29	52.5	0.0	-2.5	53.0	53.04	670.1	463.2	608.3	465.5	61.8	-2.3	37.8	48.9	2.04	2.78
30	39.5	0.0	0.0	40.0	39.97	644.0	432.9	606.7	463.9	37.3	-31.0	0.1	48.5	0.00	2.75
31	39.5	0.0	2.5	40.0	39.97	621.0	403.9	606.7	463.9	14.3	-60.0	-36.9	49.4	-2.00	2.81
32	39.5	0.0	-2.5	40.0	39.97	667.9	461.7	606.7	463.9	61.1	-2.2	37.4	48.4	2.02	2.75
33	24.5	0.0	0.0	25.0	24.97	642.7	430.9	605.6	463.6	37.2	-32.7	-1.3	49.5	-0.07	2.81
34	24.5	0.0	2.5	25.0	24.97	618.9	401.3	605.6	463.6	13.4	-62.3	-39.3	50.1	-2.12	2.85
35	24.5	0.0	-2.5	25.0	24.97	667.6	459.6	605.6	463.6	62.0	-4.0	36.7	50.2	1.98	2.85
36	39.5	0.0	0.0	40.0	40.03	644.9	433.8	606.7	463.9	38.2	-30.1	1.3	48.6	0.07	2.76
38	39.5	2.8	0.0	40.0	40.03	605.3	465.7	606.7	463.9	-1.5	1.8	0.5	-2.3	0.02	-0.13

* OS37 is not included because only 3 holes were visible at the XEL=-2.8º position due to the TA/aperture offset described below.

From TC-HIPO-01 the angle between the X axis of HIPO and the EL axis on the TA is 39.81º and can be used to derive ΔEL and ΔXEL on the TA from ΔX and ΔY on HIPO.

Between OS17 and OS18 the AA was moved 5º in EL in order to establish the scale of HIPO pixels to degrees of TA elevation motion which results in 18.5 pix/º.

Unfortunately only three of the fiducial holes were visible on OS37 so the offset between OS37 and OS38 could not be used to calculate the scale in XEL. OS14 and OS16 were used instead which yields 17.6 pix/º to convert ΔXEL from pixels to degrees. The reason why the scale in elevation does not match the scale in cross elevation is related to the fact that there is an offset of 2.5m between the center of the spherical bearing and the line of sight axis for the TA which does not affect the elevation axis.

The mask was designed to be centered fore to aft in the aperture with the mask center 1635.8mm from the truss at the fore and the same distance from the center of the ramp at the aft. HIPO images taken during this test confirm structural models of the TA location in the cavity which show that the TA is not centered in the cavity fore to aft. There is a 137.2mm offset between the center of the aperture and the center of the TA with the center of the TA being aft of the center of the aperture. This offset was derived from the HIPO images using a pixel scale of 2.8mm/pixel at the mask and a ΔXEL between the center of the TA and the center of the mask of 49 pixels. For future use, the mask should be modified so that the horizontal positioning arm of the mask is 137.2mm longer than it currently is. Figure 2-4 shows the size and sense of the offset between the center of the aperture and center of the TA.

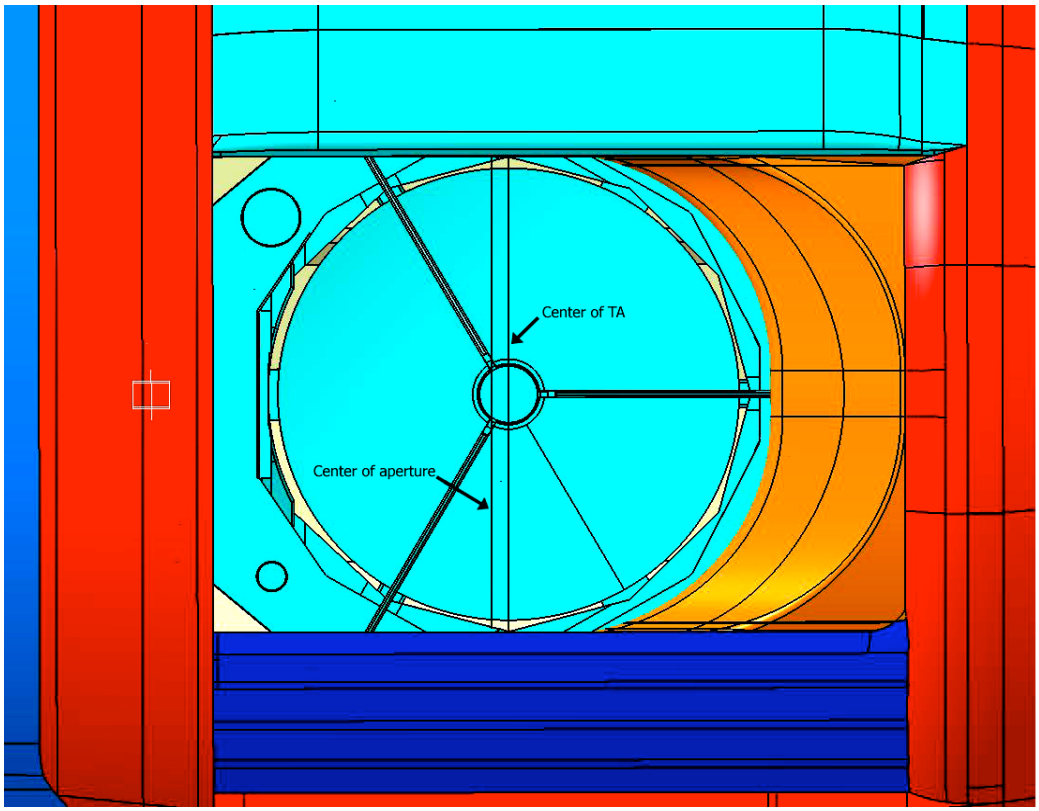

Figure 2-4. Two vertical lines indicate the center of the TA and the center of the aperture, the TA center is aft of the aperture center by 137.2 mm

The offset between the TA and the aperture mask in the XEL direction can also be clearly seen in the HIPO images shown in Figure 2-5.

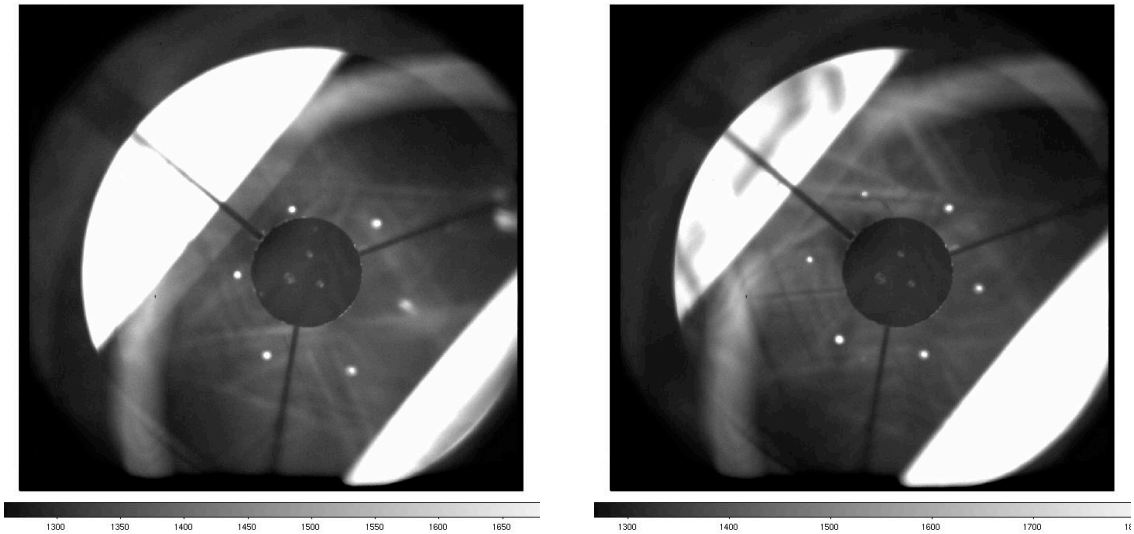

Figure 2-5. The image at the left (OS14) is with XEL=0º while the right image (OS16) has XEL=+3.0º.

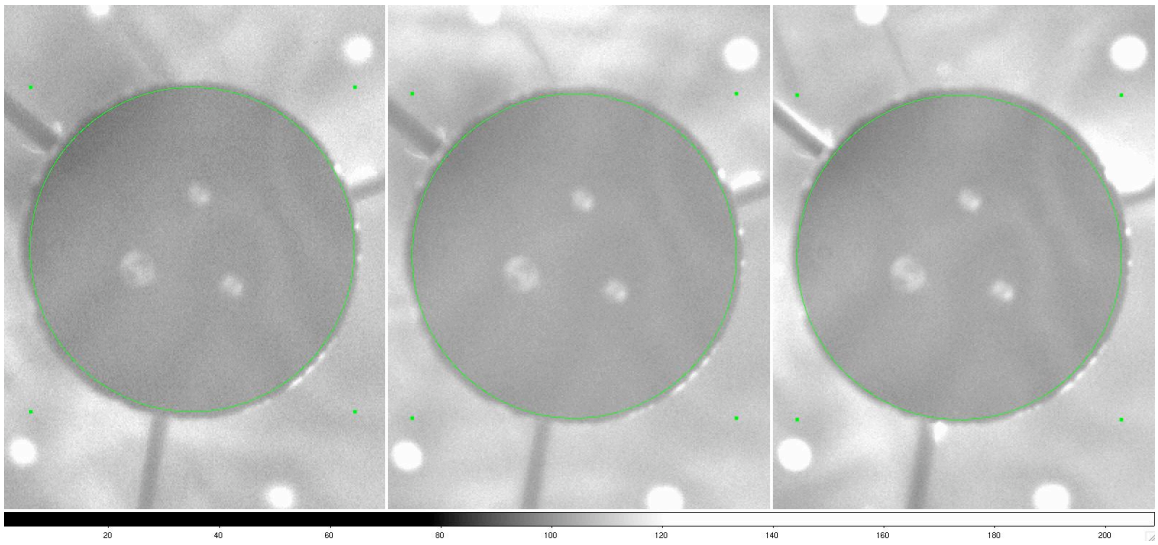

Figure 2-6. The images from left to right, are at a TA elevation of 24.5º (OS25), 40.0º (OS24), and 52.5º (OS26). These show the spherical mirror button in the center of the secondary and have an overlaid circle 224 pixels in diameter centered at HIPO pixel coordinates (607,464). This circle is well centered in the 40º case but is slightly offset in opposite directions in the other two cases. The best center for the 24.5º case is (605.6,463.6) and (608.3,465.5) for the 52.5º case. "Up" on the sky is toward the upper right so the central obscuration appears to sags in the "down" direction at lower elevation angles as a result of HIPO's internal flexure.

This test appears to show a shift in the position of the central obscuration of the SMA as a function of elevation. The SMA obscuration center was measured in pixels on HIPO by

positioning a circle outlining the shadow of the SMA against the aperture mask, then all of the central obscuration positions at each of the three TA elevations used were averaged. This was done by eye with an accuracy of ~1 pixel. Figure 2-6 shows the results of these measurements.

Data Analysis:

Initial data analysis was done "on the fly" to establish the center of the mask by measuring and averaging the centroids of the fiducial holes on the mask and comparing that to the measured center of the SMA central obscuration. It was quickly established that the offsets in X and Y on HIPO would have to be transformed into offsets in elevation and cross elevation in order to get the proper TA to aperture alignment. Afterwards a second analysis was done in an attempt to improve on the precision and accuracy of the measurements of both the fiducial centroids and the SMA central obscuration. In the second iteration the elevation specific central obscuration positions were used to calculate the offset between TA and aperture.

Results:

The starting position of the TA and aperture for the test is shown for OS14 in Table 2-3 below. From there the elevation and cross elevation offsets were calculated in order to minimize the offset between the central obscuration of the SMA and the center of the aperture mask. OS24 show very nice alignment of the TA and aperture using a +0.5º offset applied to the aperture position along with XEL=+2.8º in order to eliminate the XEL component of the measurement. This aperture offset also works nicely at TA elevation of 52.5ºs indicated by OS26.

Unfortunately the offset is less accurate at the 24.5 elevation. Both OS25 and OS33 show an additional offset of -0.12º and -0.07º respectively, implying that the best offset for the aperture at low elevation would be more accurate at +0.6º instead of +0.5º which works for the higher elevations. Despite this it's important to recall that the expected uncertainty in the aperture positioning is expected to be ~0.1º on the ground due to the size of the CDDS actuator gear teeth and could be as much as ~0.2º in flight due to flexure in the fuselage and/or gear track.

Another interesting revelation in the data is the XEL offset of -0.13º on OS38 after moving from XEL=-2.8º to +2.8º. OS38 was taken after several moves across the full range of LOS from OS27 to OS35 as well as full move across the XEL range from OS37 to OS38. This indicates a potential inconsistency in the positioning of the TA XEL axis which may be more thoroughly discussed in successive HIPO test reports.

Table 2-3: Summary of the optimal TA to aperture alignment positions

OS	TA EL	TA XEL	AA EL	ΔEL (deg)	ΔXEL (deg)
14	40.0	0.0	40.04	-0.49	2.81
24	40.0	2.8	40.48	0.01	0.01
25	24.5	2.8	24.96	-0.12	0.02
26	52.5	2.8	53.04	0.00	0.02
27	52.5	0.0	53.04	0.02	2.76
33	24.5	0.0	24.97	-0.07	2.81
38	39.5	2.8	40.03	0.02	-0.13

At TA EL=24.5º, 39.5º, and 52.5º and the TA was moved from LOS=+2.5º to -2.5º to investigate evidence of vignetting of the TA pupil by the upper or lower edges of the aperture across the LOS range. At the LOS=-2.5º position the horizontal positioning arm along the bottom of the mask is faintly visible, indicated by the red arrow in figure 2-7.

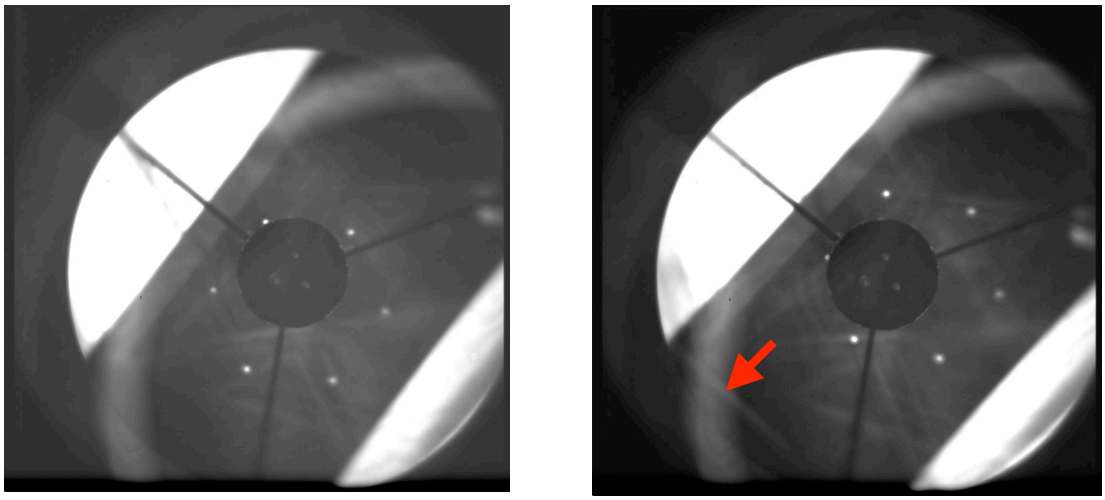

Figure 2-7. The image at the left (OS31) is with LOS=+2.5º and the right image (OS32) has LOS=-2.5º. Again +EL is to the upper right and +XEL is to the bottom right. These images were taken at EL=39.5º and XEL=0º, the results are consistent with EL=24.5º and 52.5º. No vignetting is visible.

From table 2-3 a scale of 0.81º relative EL motion for 1º of LOS motion can be derived, as well a scale of (0.81*18.5pix/º)=15pix/º for LOS motion in the EL direction, which is consistent with the results in part 1 of this test.

Table 2-3: Effective EL motion for LOS

OS	TA EL	AA EL	LOS	ΔEL (deg)
28	52.5	53.04	2.5	-1.99
29	52.5	53.04	-2.5	2.04
31	39.5	39.97	2.5	-2.00
32	39.5	39.97	-2.5	2.02
34	24.5	24.97	2.5	-2.12
35	24.5	24.97	-2.5	1.98

In figure 2-8 the full range of XEL from -2.8º to +2.8º is explored at TA El=39.5º and LOS=0º without visible evidence of vignetting of the TA pupil by the front truss or the aft ramp of the aperture. Recall from the measurements between OS14 and OS16 the scale of 17.6pix/º for XEL motion.

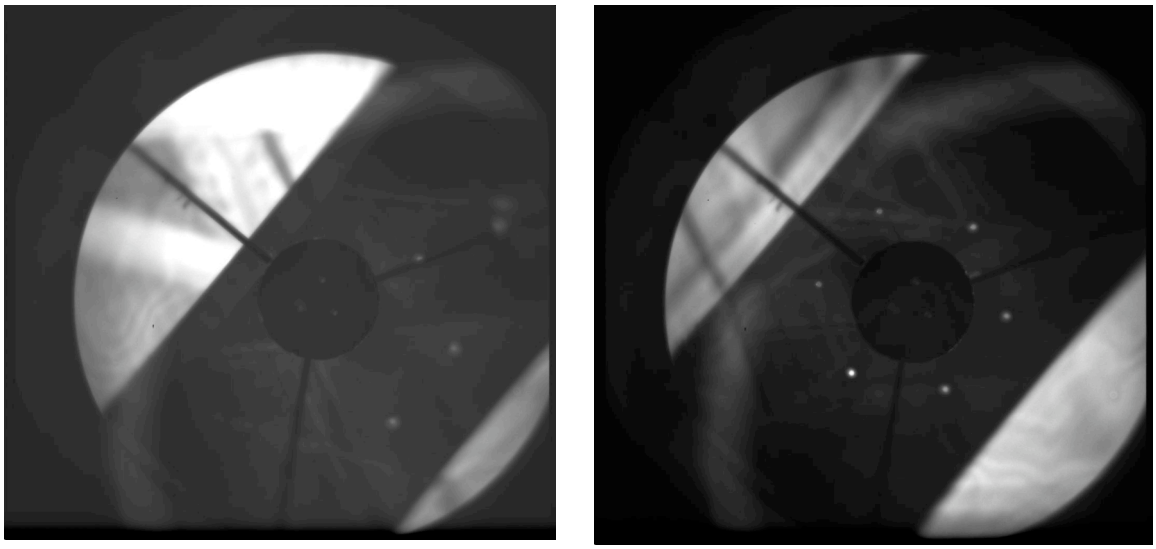

Figure 2-8. The image at the left (OS37) is with XEL=-2.8º while the right image (OS38) has XEL=+2.8º. Note that three of the fiducial holes are not visible at the XEL= -2.8º position. No vignetting is visible.

Conclusions:

From part 1 an offset between the TA and aperture of +0.4º was derived such that the AA EL=TA EL+0.4º with the full range of LOS available without adjusting the aperture at a given elevation. In part 2 a more rigorous analysis was conducted using the aperture mask that revealed an offset of +0.5º at a TA elevation of 52.5º and 40º, and an offset of closer to +0.6º at TA elevation 24.5º. The implication is that the aperture sags more at lower elevation than it does at higher elevations. Despite this, given the ~0.1º-0.2º uncertainty in aperture positioning that will be expected during flight an adopted offset for the system that works for all elevations should be AA EL=TA EL+0.5º. Alternatively

a linear function can be fit from 40º to 24.5º that changes the offset from +0.5º to +0.6º as the TA elevation decreases.

A summary of the scale of pixels of HIPO pupil images per degree of TA motion are presented in table 2-4.

Table 2-4: HIPO pupil image pixel scales for the 3 TA axes

Axis	pixel/degree
EL	18.5
XEL	17.6
LOS	15.0

Given the 1016mm (361.7 pixel) diameter of the fiducial hole pattern a scale of 2.8mm/pix of motion at the mask can also be established.

The available envelope of ±2.5º LOS and ±2.8º XEL motion was also checked for obvious vignetting of the TA pupil by the aperture and none was visually detected.

Next steps:

1) In most cases in the future if a quick and dirty "sanity" check of the TA and aperture alignment is needed the technique from part 1 will be sufficient.

2) Despite (1) the aperture mask should be modified by lengthening the horizontal positioning arm by 137.2mm in order to eliminate the XEL offset between the center of the TA line of sight and the center of the aperture and it should be kept in storage at DAOF.

3) The +0.5º offset between the TA elevation angle and aperture elevation angle needs to be incorporated into the CDDS section of the MCCS.

4) The observed sag in the central obscuration of the secondary mirror as a function of elevation is a consequence of HIPO's internal instrument flexure. Between TA elevation 52.5º and 24.5º, the observed secondary mirror drift matches what is expected based upon TC-HIPO-01 boresight flexures.

TC-HIPO-03: SMA Operations

Preface:

These four tests cover the combined operation of the focusing centering mechanism (FCM) and the tilt chopping mechanism (TCM) of the secondary mirror assembly. In the first two tests, HIPO will monitor the repositioning of the secondary mirror through use of a retroreflection LED and a spherical "button" mounted at the location of the secondary mirror. These two tests can be conducted in the hangar with the aperture door closed, or outside when it is too cloudy to do other tests. The third test is an analysis activity that will determine the FCM focus range based on the results of other tests. The fourth test consists of two simple measurements of in-focus chopped image quality on the sky at night. The measured image quality will be compared with expected image quality calculated from the results of the Shack-Hartmann tests TC-HIPO-05.

TC-HIPO-03 Part 1: FCM stability and motion reproducibility

Introduction:

Because of the schedule constraints imposed on the line-op test the scope of this test was reduced to a comparison between the FCM position readouts and the observed retroreflection image position. As a result of configuration management issues, formal requirements verification is postponed to later in the observatory's development schedule. This test was done entirely in the hangar on 14 December, 2008 UT.

The retroreflection light source is an illuminated pinhole at the TA focus that shines out from HIPO onto a concave spherical mirror button mounted on the secondary mirror, and is reflected back onto the HIPO array where it forms an image of the pinhole. The mirror button has the same radius of curvature as the primary mirror. As a result, the optical effect of tilting the secondary is the same as for the actual secondary when observing stars, but the decenter effect is quite different.

Data Acquired:

Table 3.1-1 lists the images obtained for this test together with the FCM positions and HIPO coordinates (in pixels) of the image formed by the retroreflection mirror on the HIPO array. The tilt behavior of the FCM was tested first at a fixed decenter, which was not recorded, and the decenter behavior was tested second at a fixed tilt, which was not recorded. Additional analysis results are included in the table as well and are discussed in the Data Analysis section.

Data Analysis:

Positions of the retroreflected pinhole image were derived using the *imexam* photometry function in IRAF. In all cases but one this was straightforward since the images were bright and isolated. The case for OS50 was complicated because the image was close to the center of the field and was embedded in a ghost reflection of the retroreflection LED. The ghost reflection was removed by subtracting the OS51 image from the OS50 image.

This almost perfectly subtracted the ghost image and the retroreflected pinhole image was then easy to work with.

The expected position of the retroreflected image was derived based on the expected image scale and orientation as derived from TC-HIPO-01 and the optical design of HIPO and the SOFIA telescope. It was observed that the correspondence between the observed and calculated positions was not as good as expected, particularly for the case of the decenter images, so a crude least-squares fit was carried out by hand. The observed minus calculated HIPO X and Y position residuals were found and the standard deviation of the X and Y residuals as well as the standard deviation of both X and Y residuals together were found. These are shown in Table 3.1-1. The angle between the HIPO coordinate system and the R/S coordinate system was varied to minimize the standard deviation of the X and Y residuals taken together. This process was repeated for the scale factor and iterated to be certain that the optimum combination of the two parameters had been found. This process was done independently for the tilt and decenter images.

Table 3.1-1: FCM Calibration Data

HIPO	FCM Positions (microns & arcsec)				Obs. HIPO		Calc. HIPO		O-C HIPO	
OS	R	S	rot_R	rot_S	X	Y	X	Y	X	Y
50			0	120	523.1	467.3	523.1	467.3	0	0
51			107	-715	31.2	998.8	30.838	999.68	0.3622	-0.8827
52			144	-670	80.8	998.1	81.015	999.23	-0.215	-1.1341
53			-668	7	80.2	89.5	79.099	88.641	1.1009	0.8587
54			-66	729	889.7	85.3	888.78	86.962	0.9155	-1.6622
55			693	172	941.9	895.8	940.64	896.2	1.2591	-0.399
							STDEV of O-C		0.61	0.8941
							STDEV, X&Y		0.931	
60	0	0			390.9	141.8	390.9	141.8	0.0	0.0
61	1000	0			370.0	155.2	369.5	155.2	0.5	0.0
62	-1000	0			411.8	128.6	412.3	128.4	-0.5	0.2
63	0	1000			404.3	162.6	404.3	163.2	0.0	-0.6
64	0	-1000			378.0	120.3	377.5	120.4	0.5	-0.1
65	2500	0			339.4	174.4	337.5	175.3	1.9	-0.9
66	-2500	0			446.0	107.0	444.3	108.3	1.7	-1.3
67	0	2500			426.5	195.3	424.4	195.2	2.1	0.1
68	0	-2500			359.5	87.6	357.4	88.4	2.1	-0.8
							STDEV of O-C		1.0	0.5
							STDEV, X&Y		1.0339	

Results:

Table 3.1-2 gives the best fit scale factor and orientation angle (as described in the TC-HIPO-01 section). For tilt, the scale factor is given in arcseconds per HIPO pixel and for decenter it is given in microns of decenter per HIPO pixel. The orientation angles are in degrees. Following the best fit values are the initially expected values, the scale factors being from the TA and HIPO optical models and the angle being from TC-HIPO-01. Finally, the ratio of the observed to expected scale and difference in the angles is shown at the right side of Table 3.1-2. The scale values are close to the expected values with

discrepancies on the order of 1.5%, and the angle for FCM tilt motions is also quite close to the expected value. There is a substantial difference in the orientation angle for decenter motions, however, that is difficult to understand.

Table 3.1-2: FCM Calibration Values

	Best Fit		Expected		Scale	Delta
	Scale	Angle, °	Scale	Angle, °	Ratio	Angle, °
Tilt	1.16	39.9	1.17	39.8	0.988	0.13
Decenter	39.6	32.1	39.0	39.8	1.016	-

The orientation of the tilt axes of the secondary is operationally important since FCM tilt will be used to offset the chop position for asymmetric chopping. The decenter capability of the FCM, on the other hand, will only be used during optical alignment, so the observed misalignment will have little effect. It is a puzzle, but not one that needs to be solved at the present time.

Conclusions:

1. The scale values are slightly different from the calculated values, but agree within about 1.5%.
2. The orientation of the R and S rotation axes (the chop directions) is aligned extremely well with the expected orientation.
3. The orientation of the R and S decenter motions appears to be significantly different (~8°) from the expected value and from the R and S tilt axis orientation. The origin of this orientation discrepancy is not known. It has no significant operational effect, so does not need to be understood in the near future.

Next Steps:

1. Doing nothing is acceptable for Early Science. Eventually it would be of interest to understand the origin of the observed angular misalignment of the decenter coordinate system.

TC-HIPO-03 Part 2: TCM settling time, end point stability, chop throw accuracy and chop angle accuracy

Introduction:

Because of the decision to skip formal verification at this point and the schedule constraints, the scope of the test was reduced to a comparison between the TCM position readouts and the observed retroreflection image position on the HIPO array. This was done both with static TCM offsets and while chopping. Analog_R and analog_S voltages corresponding to TCM position were measured using the LabView SI simulator unit.

Data Acquired:

HIPO images and LabView voltages were recorded between 2:20 and 4:32, December 14th UTC. There were a total of 42 images recorded for this test, though some were acquisition images used to align the chop on the HIPO array. LabView files were recorded during most but not all HIPO images. EGSE housekeeping data is available from 2:20 UT until 3:07 UT, but is missing after that time, possibly due to running out of disk space during the recording.

HIPO Images, LabView files and EGSE files acquired for TCM test

Image #	HIPO image description	LabView file name	Commanded TCM position
OS 2 – 12	2 second exposure of chop with 1 arcmin throw, 0° &50° chop angle on HIPO	081213_163912 - 081213_183816	Recorded by EGSE
OS 13 - 25	"Fast-dots" images of chop with 1 arcmin throw, 50.2° chop angle on HIPO	081213_185926 – 081213_190254	Recorded by EGSE
OS 28 – 30	2 second exposure of chop with 1 arcmin throw, 140.2° chop angle	081213_192734 - 081213_193343	From HIPO observing notes, not recorded by EGSE
OS 32 – 34	2 second exposure of small throw, upper right corner	N/A	Not recorded by EGSE
OS 37	One endpoint of 10 arcmin, 90° chop, centered on beam splitter, while chopping	081213_193354 – 081213_193424	TCM and FCM positions from HIPO observing notes
OS 43 – 45	2 second exposure of small chop, lower right corner	N/A	Not recorded by EGSE
OS 48	Other endpoint of 10 arcmin, 90° chop, centered on beam splitter	081213_193434	TCM and FCM positions from HIPO observing notes

Configurations tested

Throw arcmin	Freq Hz	Angle deg	Sync source	Waveform source
1	2.5	0	external	internal
1	2.5	50	external	internal
1	2.5	50.1	external	internal
1	2.5	50.2	external	internal
10	2	140.2	external	internal
10	5	140.2	external	internal

This TCM test contains eight subsections:

(1) Chop throw accuracy, calculated from images and (2) from voltages

(3) Chop angle accuracy, calculated from images and (4) from voltages

(5) Settle time, calculated from images and (6) from voltages

(7) End point stability, calculated from images (8) and voltages.

(1) Chop throw accuracy, calculated from the images

Analysis:

Chop amplitude error is the absolute difference between the commanded peak-to-peak amplitude, ∅c, and the achieved peak-to-peak amplitude, ∅a. ∅a is measured using the average end-point displacement during the period following the end of the settle time, t_s, in each half chop cycle. The peak-to-peak chop amplitude should ideally be adjustable from 2 arcsec to 10 arcminutes (on the sky), in increments of 0.5 arcseconds or less. It is hoped that the amplitude error, |∅c -∅a |, will be within +/-10% of the commanded amplitude.

There were 11 usable 'stare' images and 10 'fast-dots' images taken of the 60 arcsecond throw. There were also three 'stare' images taken of the 10 arcminute throw. The 60 arcsecond throw should be accurate to within 6 arcseconds, and the 10 arcmin throw should be accurate to within 60 arcsec. Since only one end of the 10 arcminute throw could be fit on the HIPO array at a time, only SM voltages can be used to examine the accuracy of the 10 arcminute throw.

Chop amplitude repeatability after interruption periods of five minutes at other chop settings was not measured in these tests. The chopper ran for 13 minutes with a 60 arcsec throw, and for 26 minutes with a 10 arcmin throw, but these settings weren't repeated after they were changed.

For each image, the X, Y pixel positions of the retroreflected spot image were measured with the iraf function *imexam*, at the both end-points of the chop. The distance in pixels between the end-points was converted to arcseconds on the sky using the HIPO plate scale 0.327 arcsec/pixel.

Stare images, chop angle < 90°

	Commanded TCM position					Observed		Observed		Observed	O-C
	chop	predicted	throw	throw	chop	endpoint, HIPO		endpoint, HIPO		throw	throw
OS	angle	HIPO angle	(mirror arcsec)	(sky arcsec)	freq, Hz	X	Y	X	Y	(sky ")	(sky ")
2	0	50.19	112.5	60.09	0.5	333.8	45.661	455.09	194.607	62.81	2.7226
3	0	50.19	112.5	60.09	0.5	135.4	132.4	256.6	281.2	62.76	2.6735
4	50.0	0.2	112.5	60.09	0.5	101.3	205.7	290.4	206.5	61.83	1.7475
6	50.2	-0.01	112.5	60.09	0.5	101.3	205.9	290.3	206.1	61.82	1.7368
7	50.2	-0.01	112.5	60.09	0.5	101.4	205.8	290.5	206.0	61.82	1.7319
10	50.2	-0.01	112.5	60.09	0.5	299.7	120.6	488.8	120.9	61.82	1.7290
11	50.2	-0.01	112.5	60.09	0.5	261.1	1012.6	450.2	1012.9	61.84	1.7496
12	50.2	-0.01	112.5	60.09	0.5	261.1	1004.9	450.4	1005.2	61.89	1.8052
										STDEV of observed - commanded throw:	0.4397

Stare images, chop angle > 90°

	Commanded TCM position					Observed		Observed		Observed	O-C
	chop	predicted	throw	throw	chop	endpoint, HIPO		endpoint, HIPO		throw	throw
OS	angle	HIPO angle	(mirror arcsec)	(sky arcsec)	freq, Hz	X	Y	X	Y	(sky ")	(sky ")
28	140.2	90.01	112.5	60.09	2	200.8	618.6	200.3	424.4	63.51	3.4206

29	140.2	90.01	112.5	60.09	2	200.8	618.6	200.4	424.4	63.51	3.4278
30	140.2	90.01	112.5	60.09	2	200.8	618.7	200.4	424.4	63.54	3.4530
										STDEV of observed - commanded throw:	0.0170

Fast-dots images, chop angle 50.2°

OS	Commanded throw (sky ")	left spot X	left spot Y	right spot X	right spot Y	Observed throw (pixels)	Observed throw (sky ")	O-C throw (sky ")
14	60.09	260.624	18.764	449.22	16.886	188.61	61.67	1.584
16	60.09	261.189	17.812	450.563	16.611	189.378	61.927	1.837
17	60.09	261.122	17.924	450.579	16.547	189.462	61.954	1.864
18	60.09	261.134	17.932	450.533	16.549	189.404	61.935	1.845
19	60.09	261.07	17.869	450.54	16.494	189.475	61.958	1.868
20	60.09	261.299	17.629	450.594	15.607	189.306	61.903	1.813
21	60.09	261.344	17.106	450.693	15.602	189.355	61.919	1.829
22	60.09	261.434	17.485	450.787	15.298	189.366	61.923	1.833
23	60.09	261.405	17.375	450.747	15.344	189.353	61.918	1.828
24	60.09	261.352	17.083	450.686	15.275	189.343	61.915	1.825
						STDEV of observed - commanded throw:		0.082

Results:

For the 11 images at 60.09 arcsec commanded throw, the amplitude error |∅c -∅a | was at most 3.45 arcsecs, well below the ≤ 6 arcsec error goal. The error was slightly greater when the chop angle was changed to 140° than when the chop angle was less than 90°. The amplitude error measured on the fast-dots images (60.09 arcsec commanded throw) was at most 1.87 arcsec, also well within the expected range.

Conclusions:

If this test with HIPO had been a verification of requirements in SOF-1011 Revision 7 for Verification for Early Science, the secondary mirror controller software would have met the accuracy requirement in section 3.3.14.3.2 (a): "*Chop amplitude adjustable from 2" to 10' in increments no greater than 0.5' with accuracy of +/- 10%*". The range and increment requirement in 3.3.14.3.2 (a) was not checked as part of this test. Section 3.3.14.3.2 (b), "*Chop amplitude repeatable to 1% of previous amplitude (or 0.2", whichever is greater) after 5 minutes of operation at other amplitudes and frequencies*" was also not checked as part of this test.

(2) Chop throw accuracy from voltages

Analysis

The average analog_R voltage was measured (after the commanded settle time) at the positive and negative end-points of the chop. The average analog_S voltage was also

calculated. Using 124.8 mirror-arcseconds per volt, and $\text{sky angle} = \frac{\text{mirror angle}}{3.7446}$, the chop throw was then

$\sqrt{analog\_S^2 + (analog\_R\_pos - analog\_R\_neg)^2}$. For a 0° chop angle, 60 arcsec throw on the sky, analog_R should ideally be ± 0.9V. analog_S should be zero.

0° chop angle, 60 arcsec throw

LabView filename	(+) endpoint analog_R	(-) endpoint analog_R	analog_S	commanded throw, sky "	calculated throw, sky	c-a, throw
_180027.010.bin	0.8989	-0.9085	0.0025	60.09	60.2365	-0.1465
_180038.096.bin	0.9000	-0.9100	0.0025	60.09	60.3216	-0.2316
_180048.331.bin	0.8999	-0.9086	-0.0045	60.09	60.2721	-0.1821
_180058.315.bin	0.8991	-0.9087	0.0025	60.09	60.2499	-0.1599
_180216.749.bin	0.9002	-0.9090	0.0025	60.09	60.2980	-0.2080
_180227.844.bin	0.8985	-0.9099	0.0025	60.09	60.2716	-0.1816
_180707.276.bin	0.8991	-0.9094	0.0025	60.09	60.2744	-0.1844
_182916.417.bin	0.9031	-0.9103	0.0026	60.09	60.4360	-0.3460
_182927.855.bin	0.9021	-0.9083	0.0027	60.09	60.3365	-0.2465
_182938.098.bin	0.9026	-0.9096	0.0027	60.09	60.3943	-0.3043
_182948.083.bin	0.8996	-0.9079	0.0027	60.09	60.2399	-0.1499
					STDEV of commanded - achieved throw:	0.0644

For a 60 arcsec 50.2° degree chop, analog_R should be ± 0.691 V, and analog_S should be ± 0.576 V.

50.2° chop angle, 60 arcsec throw (during 'fast-dots' images)

LabView filename	(+) endpoint analog_R	(-) endpoint analog_R	(+) endpoint analog_S	(-) endpoint analog_S	analog_R total range	analog_S total range	commanded throw, sky "	calculated throw, sky"	c-a throw
_185926.660	0.5740	-0.5804	0.6984	-0.6932	1.1544	1.3916	60.09	60.2604	0.17045
_185937.756	0.5750	-0.5853	0.6985	-0.6931	1.1603	1.3916	60.09	60.3857	0.29567
_185948.001	0.5757	-0.5835	0.6979	-0.6927	1.1592	1.3906	60.09	60.3380	0.24804
_185957.986	0.5723	-0.5826	0.6982	-0.6932	1.1549	1.3914	60.09	60.2648	0.17478
_190007.970	0.5731	-0.5843	0.6980	-0.6936	1.1574	1.3917	60.09	60.3253	0.23527
_190017.954	0.5750	-0.5837	0.6989	-0.6929	1.1587	1.3918	60.09	60.3572	0.26723
_190124.049	0.5727	-0.5841	0.6988	-0.6929	1.1568	1.3916	60.09	60.3115	0.22151
_190135.125	0.5758	-0.5819	0.6988	-0.6933	1.1577	1.3921	60.09	60.3431	0.25307
_190145.370	0.5762	-0.5842	0.6983	-0.6934	1.1604	1.3917	60.09	60.3905	0.30047
_190155.355	0.5766	-0.5834	0.6987	-0.6932	1.1600	1.3919	60.09	60.3878	0.29784
_190205.338	0.5744	-0.5840	0.6986	-0.6933	1.1585	1.3919	60.09	60.3545	0.26455
_190222.894	0.5748	-0.5832	0.6980	-0.6926	1.1580	1.3905	60.09	60.3091	0.21905
_190233.980	0.5771	-0.5838	0.6980	-0.6926	1.1608	1.3905	60.09	60.3700	0.28000
_190244.224	0.5741	-0.5833	0.6981	-0.6922	1.1574	1.3904	60.09	60.2924	0.20237
_190254.210	0.5749	-0.5850	0.6981	-0.6923	1.1599	1.3904	60.09	60.3482	0.25823
							STDEV of commanded - achieved throw:		0.0417

For a 60 arcsec 140.2° degree chop, analog_R should be ± 0.691 V, and analog_S should be ± 0.576 V.

140.2° chop angle, 60 arcsec throw

LabView filename	(+) endpoint analog_R	(-) endpoint analog_R	(+) endpoint analog_S	(-) endpoint analog_S	analog_R total range	analog_S total range	commanded throw, sky "	calculated throw, sky	c-a throv
_192734.016	0.6882	-0.7015	0.5815	-0.5764	1.3897	1.1579	60.09	60.2867	-0.1967
_192745.112	0.6905	-0.7005	0.5822	-0.5758	1.3910	1.1579	60.09	60.3188	-0.2288
_192755.348	0.6913	-0.6993	0.5819	-0.5761	1.3906	1.1581	60.09	60.3118	-0.2218
								STDEV of commanded - achieved throw:	0.0169

For a 10 arcmin (the maximum possible chop throw), 0° chop, analog_R should be ±9.0 V, and analog_S should be zero. For a 10 arcmin, 140.2° chop, analog_R should be ±6.91 V, and analog_S should be ± 5.76 V.

140.2° chop angle, 600 arcsec throw

LabView filename	(+) endpoint analog_R	(-) endpoint analog_R	(+) endpoint analog_S	(-) endpoint analog_S	analog_R total range	analog_S total range	commanded throw, sky "	calculated throw, sky"	c-a throw
_193343.267	7.0035	-7.0103	5.8413	-5.8448	14.0139	11.6862	600	608.1373	8.1373
_193354.333	6.9945	-7.0119	5.8395	-5.8366	14.0064	11.6761	600	607.7297	7.7297
_193404.578	7.0126	-7.0141	5.8452	-5.8543	14.0267	11.6995	600	608.7506	8.7506
_193414.562	7.0035	-7.0146	5.8459	-5.8476	14.0182	11.6935	600	608.4032	8.4032
_193424.547	7.0043	-7.0130	5.8478	-5.8493	14.0173	11.6970	600	608.4571	8.4571
_193434.532	7.0053	-7.0204	5.8500	-5.8507	14.0257	11.7006	600	608.7504	8.7504
								STDEV of commanded - achieved throw:	0.3905

Results

A 60 arcsec throw should be accurate to within 0.09V (6 arcsec) and a 10 arcmin throw should be accurate to within 0.9V (60 arcsec).

The LabView data taken during a 60 arcsec, 0° chop angle, show an amplitude error | ∅c-∅a | < 0.34 arcsec, well within the expected range. There appears to be a small offset in the analog_S voltage in the 0° chop. Analog_S should be zero but is 0.0019 on average.

The voltage data taken during 50.2° degree chop, 60 arcsec commanded throws show an amplitude error | ∅c-∅a | < 0.298 arcsec

The LabView data taken during a 60 arcsec, 140.2° chop shows |∅c-∅a | < 0.23 arcsec. The 600 arcsec, 140.2° chop shows | ∅c-∅a | < 8.76 arcsec. These amplitude errors are all within the expected values.

Image #	HIPO image description	|∅c-∅a | images	LabView file name	|∅c-∅a | voltages

OS 2 – 12	60 arcsec throw, 0° &50° chop angle on HIPO	< 2.73 arcsec	081213_163912 - 081213_183816	< 0.346 arcsec
OS 13 - 25	60 arcsec throw, 50.2° chop angle on HIPO. "Fast-dots"	< 1.87 arcsec	081213_185926 – 081213_190254	< 0.298 arcsec
OS 28 – 30	60 arcsec throw, 140.2° chop angle on HIPO	< 3.46 arcsec	081213_192734 - 081213_193343	< 0.230 arcsec
OS 37, 48	Endpoints of 10 arcmin, 90° chop on HIPO	N/A	081213_193354 – 081213_193424	< 8.760 arcsec

There is a slightly smaller throw error in the voltage measurements than measured in images because the average voltage is not calculated until after the commanded settle time has elapsed, which leaves out the effect of overshoot (if any). The measurement of the throw on the images would include overshoot. The throw error is very small however, whether measured using images or voltages. When the tuning of the new mirror controller has been completed, throws measured from images and from voltages will be the same.

Conclusions:

If this test with HIPO had been a verification of requirements in SOF-1011 Revision 7 for Verification for Early Science, the secondary mirror controller software would have met the accuracy requirement in section 3.3.14.3.2 (a): "*Chop amplitude adjustable from 2" to 10' in increments no greater than 0.5' with accuracy of +/- 10%*". The range and increment requirement in 3.3.14.3.2 (a) was not checked as part of this test. Section 3.3.14.3.2 (b), "*Chop amplitude repeatable to 1% of previous amplitude (or 0.2", whichever is greater) after 5 minutes of operation at other amplitudes and frequencies*" was also not checked as part of this test.

(3) Chop angle accuracy, from images

The chop angle is measured counter-clockwise from the EL axis (+R) toward the (-S) XEL axis on the SM, as seen from the primary mirror.

Analysis:

Used results from TC-HIPO-01 to calculate predicted chop angle on the HIPO array. Angle between HIPO rows and the (rot_v) of the TA is 39.81°. So, to convert chop angle to angle on HIPO: *HIPO angle = (90-39.81)-(SM chop angle)*

Stare images, chop angle 0° & 50°

	Commanded TCM position					Observed		Observed		Observed	O-C
	chop	predicted	throw	throw	chop	endpoint, HIPO		endpoint, HIPO		angle	angle
OS	angle	HIPO angle	(mirror arcsec)	(sky arcsec)	freq, Hz	X	Y	X	Y	seen by HIPO	
2	0	50.19	112.5	60.09	0.5	333.8	45.661	455.09	194.607	50.8459	0.6559
3	0	50.19	112.5	60.09	0.5	135.4	132.4	256.6	281.2	50.8375	0.6475

4	50.0	0.2	112.5	60.09	0.5	101.3	205.7	290.4	206.5	0.2651	0.0751
6	50.2	-0.01	112.5	60.09	0.5	101.3	205.9	290.3	206.1	0.0797	0.0897
7	50.2	-0.01	112.5	60.09	0.5	101.4	205.8	290.5	206.0	0.0509	0.0609
10	50.2	-0.01	112.5	60.09	0.5	299.7	120.6	488.8	120.9	0.0834	0.0934
11	50.2	-0.01	112.5	60.09	0.5	261.1	1012.6	450.2	1012.9	0.0800	0.0900
12	50.2	-0.01	112.5	60.09	0.5	261.1	1004.9	450.4	1005.2	0.0869	0.0969
									st dev of observed - commanded:		0.2629

Stare images, chop angle 140.2°

	Commanded TCM position					Observed endpoint, HIPO		Observed endpoint, HIPO		Observed angle	O-C angle
OS	chop angle	predicted HIPO angle	throw (mirror arcsec)	throw (sky arcsec)	chop freq, Hz	X	Y	X	Y	seen by HIPO	
28	140.2	90.01	112.5	60.09	2	200.8	618.6	200.3	424.4	89.8749	-0.1351
29	140.2	90.01	112.5	60.09	2	200.8	618.6	200.4	424.4	89.8850	-0.1250
30	140.2	90.01	112.5	60.09	2	200.8	618.7	200.4	424.4	89.8773	-0.1327
									STDEV of observed - commanded:		0.0052

Fast-dots images, chop angle 50.2° (0° on HIPO)

OS	Commanded angle mirror	left spot		right spot		predicted angle on HIPO	Observed angle on HIPO	O-C throw
		X	Y	X	Y			
14	50.2	260.624	18.764	449.22	16.886	0.00	-0.571	-0.571
16	50.2	261.189	17.812	450.563	16.611	0.00	-0.363	-0.363
17	50.2	261.122	17.924	450.579	16.547	0.00	-0.416	-0.416
18	50.2	261.134	17.932	450.533	16.549	0.00	-0.418	-0.418
19	50.2	261.07	17.869	450.54	16.494	0.00	-0.416	-0.416
20	50.2	261.299	17.629	450.594	15.607	0.00	-0.612	-0.612
21	50.2	261.344	17.106	450.693	15.602	0.00	-0.455	-0.455
22	50.2	261.434	17.485	450.787	15.298	0.00	-0.662	-0.662
23	50.2	261.405	17.375	450.747	15.344	0.00	-0.615	-0.615
24	50.2	261.352	17.083	450.686	15.275	0.00	-0.547	-0.547
						STDEV of observed - commanded:		0.105

Results:

The stare images of SM chop angle of 0° have an angle error of < 0.66°. A commanded SM chop angle of 50.2° has angle error of <0.67°. A commanded SM angle of 140.2° has an error in angle of < 0.14°.

Conclusions:

If this test with HIPO had been a verification of requirements in SOF-1011 Revision 7 for Verification for Early Science, the secondary mirror controller software would not have

failed the range requirement in section 3.3.14.3.8(a), "*Chop angle adjustable through 180 degrees with 0.2 degree resolution*". The entire 180 degree range and the 0.2 degree resolution was not checked as part of this test. Section 3.3.14.3.8(b), "*Chop angle stable to within +/- 0.5 degrees over 1 hour*" was also not verified as part of this test.

(4) Chop angle accuracy, from voltages

Angle error, 0° commanded chop angle

LabView filename	(+) endpoint analog_R	(-) endpoint analog_R	analog_S	calculated chop angle	commanded cmd sm angle	c-a, angle
_180027.010.bin	0.8989	-0.9085	0.0025	0.0796	0.0000	0.0796
_180038.096.bin	0.9000	-0.9100	0.0025	0.0778	0.0000	0.0778
_180048.331.bin	0.8999	-0.9086	-0.0045	-0.1421	0.0000	-0.1421
_180058.315.bin	0.8991	-0.9087	0.0025	0.0777	0.0000	0.0777
_180216.749.bin	0.9002	-0.9090	0.0025	0.0777	0.0000	0.0777
_180227.844.bin	0.8985	-0.9099	0.0025	0.0781	0.0000	0.0781
_180707.276.bin	0.8991	-0.9094	0.0025	0.0794	0.0000	0.0794
_182916.417.bin	0.9031	-0.9103	0.0026	0.0830	0.0000	0.0830
_182927.855.bin	0.9021	-0.9083	0.0027	0.0842	0.0000	0.0842
_182938.098.bin	0.9026	-0.9096	0.0027	0.0844	0.0000	0.0844
_182948.083.bin	0.8996	-0.9079	0.0027	0.0844	0.0000	0.0844
					STDEV of commanded - achieved:	0.0672

Angle error, 140.2° commanded chop angle, 60 arcsec throw

LabView filename	(+) endpoint analog_R	(-) endpoint analog_R	(+) endpoint analog_S	(-) endpoint analog_S	analog_R total range	analog_S total range	calculated angle, SM	commanded angle, SM	c-a angle
_192734.016	0.6882	-0.7015	0.5815	-0.5764	1.3897	1.1579	-50.051751	-50.2	0.1482
_192745.112	0.6905	-0.7005	0.5822	-0.5758	1.3910	1.1579	-50.176364	-50.2	0.0236
_192755.348	0.6913	-0.6993	0.5819	-0.5761	1.3906	1.1581	-50.193846	-50.2	0.0062
								STDEV of commanded - achieved:	0.0775

Angle error, 140.2° commanded chop angle, 600 arcsec throw

LabView filename	(+) endpoint analog_R	(-) endpoint analog_R	(+) endpoint analog_S	(-) endpoint analog_S	analog_R total range	analog_S total range	calculated angle, SM	commanded angle, SM	c-a angle
_193343.267	7.0035	-7.0103	5.8413	-5.8448	14.0139	11.6862	-50.153154	-50.2	-0.0468
_193354.333	6.9945	-7.0119	5.8395	-5.8366	14.0064	11.6761	-50.156548	-50.2	-0.0435
_193404.578	7.0126	-7.0141	5.8452	-5.8543	14.0267	11.6995	-50.144128	-50.2	-0.0559
_193414.562	7.0035	-7.0146	5.8459	-5.8476	14.0182	11.6935	-50.139797	-50.2	-0.0602
_193424.547	7.0043	-7.0130	5.8478	-5.8493	14.0173	11.6970	-50.134734	-50.2	-0.0653
_193434.532	7.0053	-7.0204	5.8500	-5.8507	14.0257	11.7006	-50.132084	-50.2	-0.0679
								STDEV of commanded - achieved:	0.0098

Angle error, 50.2 commanded chop angle, 60 arcsec throw, during 'fast dots' images

LabView filename	(+) endpoint analog_R	(-) endpoint analog_R	(+) endpoint analog_S	(-) endpoint analog_S	analog_R total range	analog_S total range	calculated angle, SM	commanded angle, SM	c-a angle
_185926.660	0.5740	-0.5804	0.6984	-0.6932	1.1544	1.3916	50.5821	50.2	0.38211
_185937.756	0.5750	-0.5853	0.6985	-0.6931	1.1603	1.3916	50.5386	50.2	0.33859
_185948.001	0.5757	-0.5835	0.6979	-0.6927	1.1592	1.3906	50.4799	50.2	0.27990
_185957.986	0.5723	-0.5826	0.6982	-0.6932	1.1549	1.3914	50.6594	50.2	0.45943
_190007.970	0.5731	-0.5843	0.6980	-0.6936	1.1574	1.3917	50.6161	50.2	0.41612
_190017.954	0.5750	-0.5837	0.6989	-0.6929	1.1587	1.3918	50.5553	50.2	0.35529
_190124.049	0.5727	-0.5841	0.6988	-0.6929	1.1568	1.3916	50.6634	50.2	0.46345
_190135.125	0.5758	-0.5819	0.6988	-0.6933	1.1577	1.3921	50.5093	50.2	0.30929
_190145.370	0.5762	-0.5842	0.6983	-0.6934	1.1604	1.3917	50.4733	50.2	0.27326
_190155.355	0.5766	-0.5834	0.6987	-0.6932	1.1600	1.3919	50.4701	50.2	0.27005
_190205.338	0.5744	-0.5840	0.6986	-0.6933	1.1585	1.3919	50.5705	50.2	0.37054
_190222.894	0.5748	-0.5832	0.6980	-0.6926	1.1580	1.3905	50.5292	50.2	0.32919
_190233.980	0.5771	-0.5838	0.6980	-0.6926	1.1608	1.3905	50.4165	50.2	0.21651
_190244.224	0.5741	-0.5833	0.6981	-0.6922	1.1574	1.3904	50.5667	50.2	0.36674
_190254.210	0.5749	-0.5850	0.6981	-0.6923	1.1599	1.3904	50.5275	50.2	0.32745
								STDEV of commanded – achieved::	0.0698

Results:

Angle error, 0° commanded chop angle, 60 arcsec throw is < 0.15°
Angle error, 140.2° commanded chop angle, 60 arcsec throw is < 0.15°
Angle error, 140.2° commanded chop angle, 600 arcsec throw is < 0.7°
Angle error, 50.2° commanded chop angle, 60 arcsec throw, during 'fast dots' images is < 0.5°

Ideally, chop angle should be commandable with 0.2° resolution, and should be stable to within ± 0.5° over periods of one hour. The chop angle was stable to within 0.5° over 26 minutes during the 'fast dots' images, but was not tested for longer. The angle error is a little larger at the commanded for a chop throw of 600 arcsec, than at smaller chop distances.

Conclusions:

If this test with HIPO had been a verification of requirements in SOF-1011 Revision 7 for Verification for Early Science, the secondary mirror controller software would not have failed the range requirement in section 3.3.14.3.8(a), "*Chop angle adjustable through 180 degrees with 0.2 degree resolution*". The entire 180 degree range and the 0.2 degree resolution was not checked as part of this test. Section 3.3.14.3.8(b), "*Chop angle stable to within +/- 0.5 degrees over 1 hour*" was also not verified as part of this test.

(5) Settle time and (7) End point stability, from images

To find the end-point stability and settle time, the IRAF function imexam was used to find pixel positions of retroreflected spots in the 10 fast-dots images, OS 12 – 14. The

fast-dots images are of 60 arcsecond chop throws, taken over a period of 13 minutes. The overall end-point stability (ΔØ) error circle radius should ideally be ≤3% of the commanded chop amplitude, or 0.6 arcsec on the sky, for periods of at least one hour. Δ∅i is the motion of the IR beam from the end of the commanded settle time until the end of an individual half-chop cycle. The end-point stability is measured at each half cycle only after the end of the commanded settling time. The overall stability includes jitter, end point drift, cycle-to-cycle non-repeatability, and center point drift. Overall stability does not include the transients before the end of the commanded settle time. The width of the error band determines the settle time. After the commanded settle time has elapsed and the spot position is within the error band (Δ∅I), the mirror can be considered settled.

Chop settling time, t_s, is defined as the time elapsed between the instant of initiation of a throw to a new position and the instant when the end point stability is achieved at the new position. Referring to Figure 1, ΔØi is the single half-chop cycle end point stability error band. It is the error band which determines settling time for any single chop position response. The chop settling time should ideally be: ≤5 milliseconds for ≤1 arcminute amplitude; ≤7 milliseconds for 4 arcminute amplitude; and ≤10 milliseconds for 10 arcminute amplitude.

Figure 1, Schematic definitions of stability error band and settle time

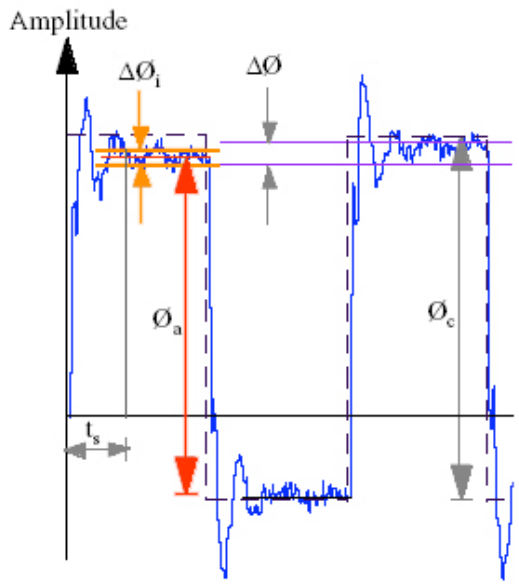

∅a is the achieved peak to peak chop amplitude

∅c is the commanded peak to peak chop amplitude

Δ∅i is the chop end-point stability for a single chop position during a half chop cycle

Δ∅ is the overall chop end-point stability error band over multiple chop cycles

t_s is the chop settle time

To find the frame that corresponds to 10 ms commanded settle time, calculate the mid-exposure time for each frame using:

$$T = T0 + (N-1)*.001 + 0.0002621 + .0007379/2$$

*T0 is start time (*UTCSTART from the HIPO image header)

N is image frame number

The time needed to shift the charge down by 42 rows is 262.1 microseconds

The exposure time is 1000 – 262.1 microseconds = 737.9 microseconds

Frame number 11 corresponds to the 10ms commanded exposure time, so the average X and Y pixel positions are measured from Frame 12 through Frame 48. The STDEV of the X and Y positions in Frames 12 through 48 is the width of the error band, Δ∅i , and the average of the pixel positions in Frames 12 – 48 is the center of the error band. The top of the error band is equal to the average pixel position + ½ width of the error band, and the bottom of the error band is equal to the average pixel position – ½ width of the error band. To find the error in X and Y, convert the STDEV from pixels to arcseconds. The radius of the error circle is then

(x_error^2)+(y_error^2)^0.5. The achieved settle time can be found by noting where the X or Y pixel position first crosses into the observed error band.

Error band, Δ∅, and error circle radius

OS	avg position after command settle time		width of error band stdev		top of error band, x	bottom of error band x	top of error band, y	bottom of error band y	arcsec error		Δ∅, error circle radius
	x	y	x	y					x	y	arcsec
14	259.67	19.23	1.81	0.72	260.57	258.76	19.58	18.87	0.59	0.23	0.64
16	449.85	18.61	13.40	2.75	459.60	446.20	20.37	17.61	4.38	0.90	4.47
17	264.08	17.37	13.68	2.59	270.92	257.24	18.66	16.07	4.47	0.85	4.55
18	264.09	18.94	11.03	0.75	266.01	254.97	19.32	18.57	3.61	0.25	3.62
19	450.29	19.90	8.14	1.27	454.36	446.22	20.54	19.26	2.66	0.42	2.69
20	262.41	18.45	8.28	0.38	266.55	258.27	18.64	18.26	2.71	0.13	2.71
21	261.90	18.35	7.79	0.72	265.79	258.00	18.71	17.99	2.55	0.24	2.56
22	262.33	17.46	8.56	1.31	266.61	258.05	18.11	16.80	2.80	0.43	2.83
23	262.05	18.32	7.74	0.77	265.92	258.18	18.70	17.94	2.53	0.25	2.54
24	262.17	17.69	8.44	0.82	266.38	257.95	18.10	17.28	2.76	0.27	2.77
										average:	2.94

Using the commanded settle time of 10 ms, the error circle radius would be on average 2.94 arcsec and not more than 4.6 arcseconds. But the mirror is still clearly moving 10ms after the start of the throw so the real achieved settle time should be used to calculate the error circle radius.

Finding settle time, X

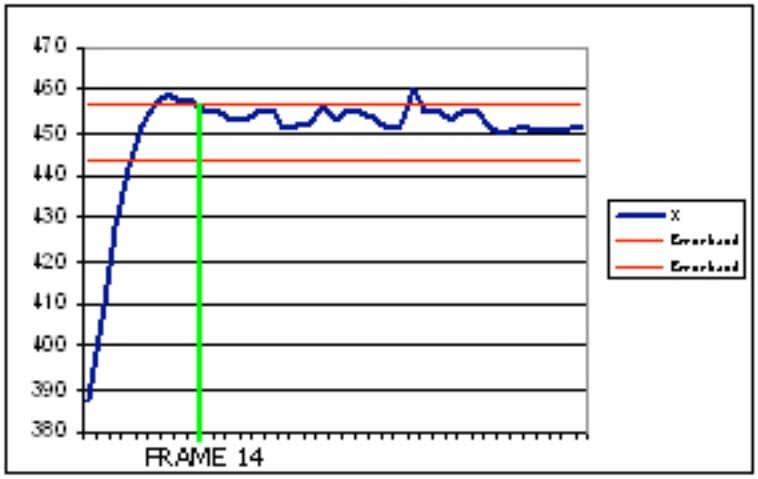

This plot of the X position in OS#16 is an example of the mirror crossing into the error band and reaching the settled condition.

The point where the plot of X position crosses into the error band corresponds to Frame #14, which has a 13.63 ms mid-time. That means the settle time for this image is 13.63 ms.

This method was repeated for X and Y positions in all of the fast-dots images. The average achieved settle time is 13.83 ms.

Settle time

OS	avg position after command settle time		width of error band stdev		top of error band, x	bottom of error band x	top of error band, y	bottom of error band y	arcsec error		ΔØ, error circle radius	settled in frame	settle time
	x	y	x	y					x	y	arcsec	#	(ms)
14	259.67	19.23	1.81	0.72	260.57	258.76	19.58	18.87	0.59	0.23	0.64	10	9.63
16	449.85	18.61	13.40	2.75	459.60	446.20	20.37	17.61	4.38	0.90	4.47	14	13.63
17	264.08	17.37	13.68	2.59	270.92	257.24	18.66	16.07	4.47	0.85	4.55	13	12.63
18	264.09	18.94	11.03	0.75	266.01	254.97	19.32	18.57	3.61	0.25	3.62	15	14.63
19	450.29	19.90	8.14	1.27	454.36	446.22	20.54	19.26	2.66	0.42	2.69	15	14.63
20	262.41	18.45	8.28	0.38	266.55	258.27	18.64	18.26	2.71	0.13	2.71	15	14.63
21	261.90	18.35	7.79	0.72	265.79	258.00	18.71	17.99	2.55	0.24	2.56	15	14.63
22	262.33	17.46	8.56	1.31	266.61	258.05	18.11	16.80	2.80	0.43	2.83	15	14.63
23	262.05	18.32	7.74	0.77	265.92	258.18	18.70	17.94	2.53	0.25	2.54	15	14.63
24	262.17	17.69	8.44	0.82	266.38	257.95	18.10	17.28	2.76	0.27	2.77	15	14.63
											average settle time:		13.83

Now, using the achieved settle time of 14 ms, the real average error circle radius is 0.80 arcseconds, and is not more than 1.3 arcseconds. Once the mirror has settled, it stays settled nicely. Error bands for positive and negative ends of chop look similar.

Error circle, using 14 ms settle time

OS	avg position after command settle time		width of error band stdev		top of error band, x	bottom of error band x	top of error band, y	bottom of error band y	arcsec error		$\Delta\varnothing$, error circle radius
	x	y	x	y					x	y	arcsec
14	260.07	19.21	1.40	0.70	260.77	259.36	19.56	18.86	0.46	0.23	0.51
16	453.65	18.51	2.63	2.88	454.96	452.33	20.40	17.52	0.86	0.94	1.28
17	260.19	17.17	2.08	2.68	261.23	259.15	18.51	15.84	0.68	0.88	1.11
18	260.51	18.97	2.03	0.62	261.46	259.43	19.28	18.66	0.66	0.20	0.69
19	452.30	19.90	2.07	1.30	453.34	451.27	20.55	19.25	0.68	0.42	0.80
20	260.32	18.46	2.00	0.33	261.32	259.32	18.63	18.30	0.66	0.11	0.66
21	259.98	18.29	2.24	0.70	261.10	258.86	18.64	17.94	0.73	0.23	0.77
22	260.14	17.40	1.89	1.34	261.09	259.19	18.07	16.73	0.62	0.44	0.76
23	260.12	18.37	1.82	0.77	261.03	259.21	18.76	17.99	0.60	0.25	0.65
24	260.05	17.76	2.24	0.68	261.17	258.93	18.10	17.42	0.73	0.22	0.76
										average:	0.80

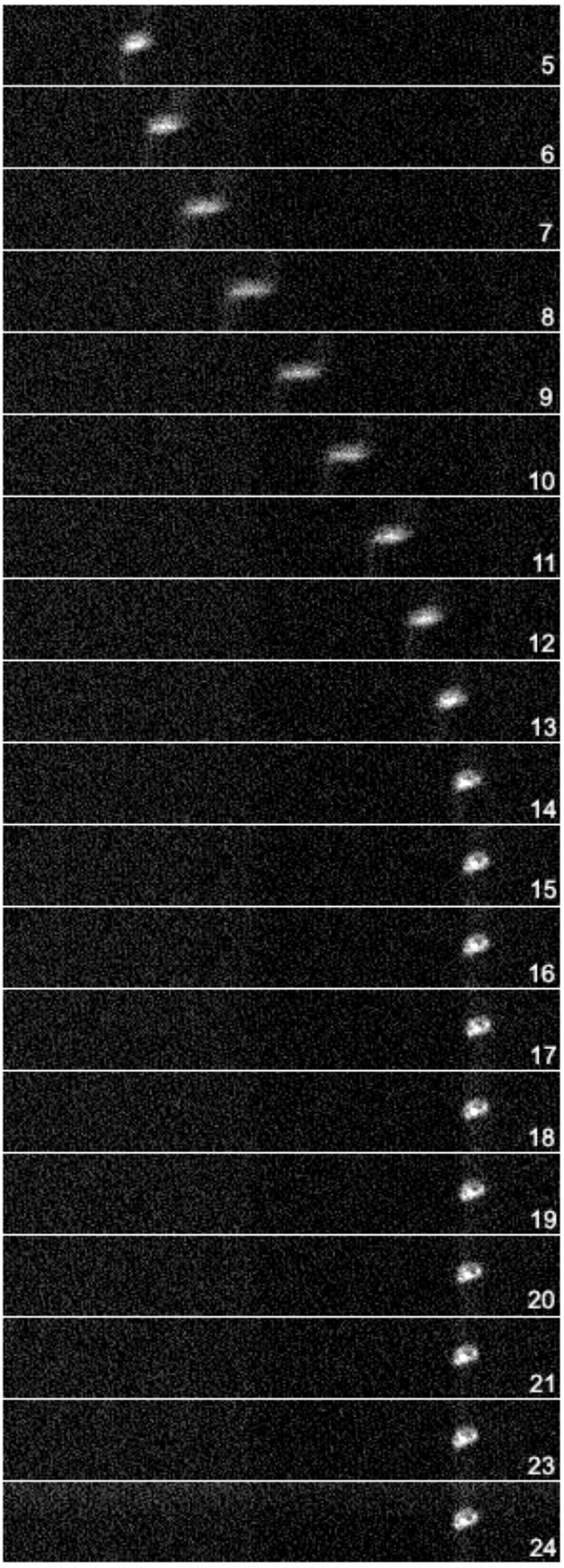

This is a subset of frames from ‘ fast-dots’ HIPO image 20081214_0019.fits, taken of one end of a 60 arcsec- throw, 2.5 Hz chop. A full fast-dots image has 48 frames, but this sub-set shows frames 5 –24.

Frame #1 was recorded at the exact second the chop was initiated by a signal from HIPO. The interval between each dot in a fast-dots image is exactly 1 millisecond.

The mirror meets the settled condition in Frame #15. The mid-exposure time for Frame #15 is 14.63 ms, so the settle time in this image is 14.63 ms.

(6) Settle time and (8) End point stability, from voltages

The overall stability goal of ≤1% of the commanded chop amplitude, or 0.2 arcsec on the sky refers to an image motion circle radius in object space which includes at two axes. For one axis, 3% peak-to-peak and 0.6 arcsecond peak-to-peak is the goal.

The error band for the positive and negative ends of the chop throw were found separately. The half-chop throw was averaged over five chop cycles, then 3% of the whole chop throw was applied to that average voltage to determine the top and bottom edge of the error band. The initiation of the chop throw is the instant the voltage value exits the error band at one end of the throw. The mirror is settled when the voltage value enters and stays within the error band at the other end of the chop throw. The settle time is measured from the initiation of a throw to the instant when the end point stability is achieved at the new position. This method of determining settle time and end point stability was used by CSEM during acceptance tests.

Voltage value leaves lower band at point 23, settles at point 36 = 13 ms settle time

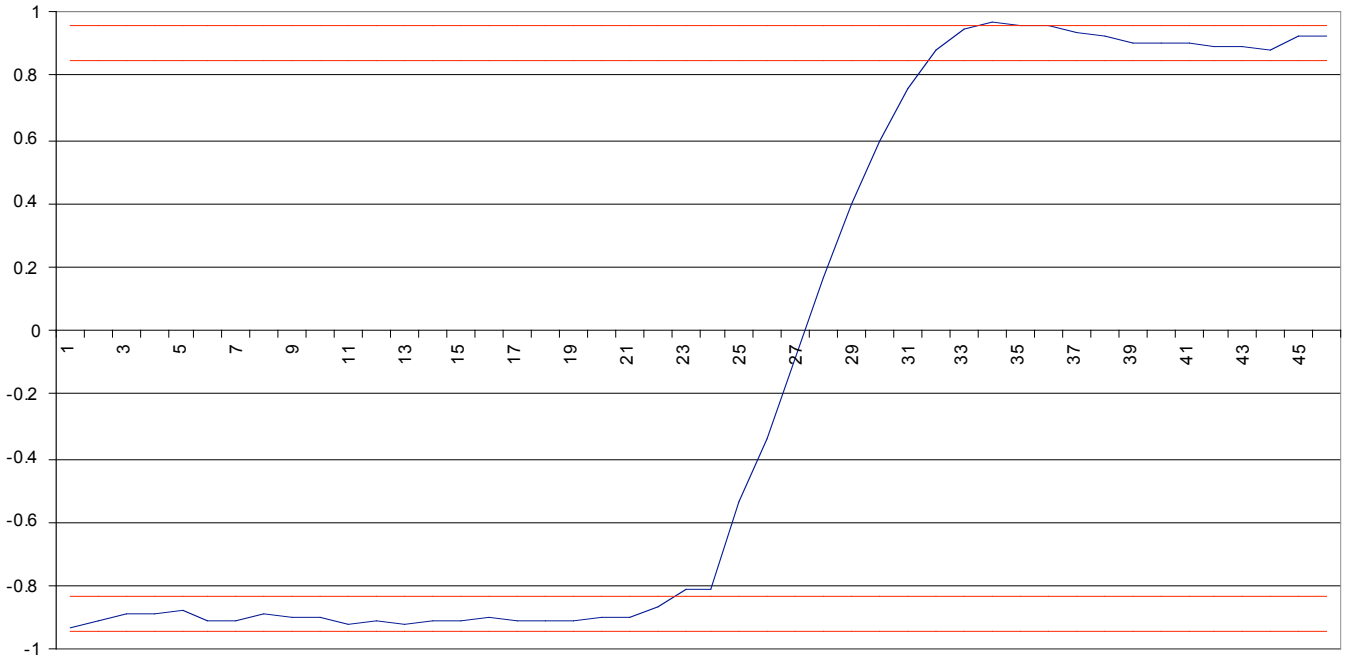

Error bands, settle times, from voltages- 1 arcmin chop throw

LabView file chop throw	analog_R, V avg of 5 cycles	avg throw arcsec, mirror	avg throw arcsec, sky	3% of whole throw, V	stability error band, top	stability error band, lower	Settle time Ts, ms
_180027.010	0.89986	112.30257	29.99054	0.05371	0.95357	0.84615	
1 arcmin	-0.89042	-111.12447	-29.67593	0.05371	-0.83671	-0.94413	13
_180038.096	0.89982	112.29808	29.98934	0.05369	0.95351	0.84613	
1 arcmin	-0.88985	-111.05359	-29.65700	0.05369	-0.83616	-0.94354	13
-180048.331	0.89292	111.43686	29.75935	0.05383	0.94676	-0.84763	

1 arcmin	-0.90147	-112.50294	-30.04405	0.05383	0.83909	-0.95530	12

Error bands, settle times, from voltages – 10 arcmin chop throw

LabView file name:	_193343.267	_193354.333	_193404.578
average throw, volts (both axes)	17.61005	17.61087	17.56019
mirror arcsec	2197.735	2197.837	2191.51111
throw, sky arcsec	586.908	586.935	585.246
3% of the throw, in sky arcsec	17.607	17.608	17.557
3% of the throw, in mirror arcsec	65.93204	65.93510	65.74533
3% of the throw, in volts	0.52830	0.52833	0.52681
analog_R, (+), avg of 5 chop cycles	6.75331	6.74812	6.72253
stability error band, top, +V	7.01746	7.01228	6.98593
stability error band, bottom, +V	6.48916	6.48395	6.45912
analog_R, (-), avg of 5 chop cycles	-6.76402	-6.76952	-6.75428
stability error band, top, -V	-6.49987	-6.50536	-6.49087
stability error band, bottom, -V	-7.02817	-7.03368	-7.01768
analog_S, (+), avg of 5 chop cycles	5.64451	5.64891	5.63791
stability error band, top, +V	5.90867	5.91307	5.90132
stability error band, bottom, +V	5.38036	5.38475	5.37451
analog_S (-), avg of 5 chop cycles	-5.64245	-5.63897	-5.61979
stability error band, top, -V	-5.37830	-5.37481	-5.35638
stability error band, bottom, -V	-5.90661	-5.90314	-5.88319
settle time, R from (-) to (+) chop end	36	41	46
settle time, S from (-) to (+) chop end	34	38	34
settle time, R from (+) to (-) chop end	36	34	41
settle time, S from (+) to (-) chop end	31	22	34

60 arcsecond, 0°, 2 Hz chop, analog_R waveform

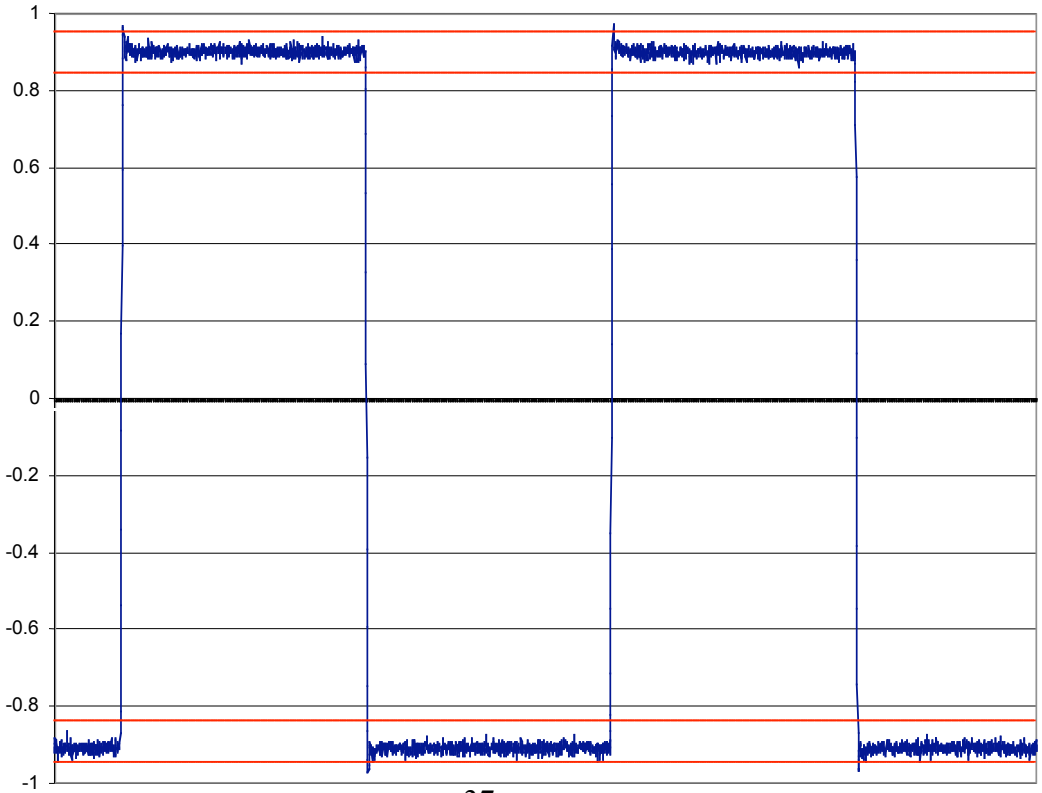

Conclusions:

Settle times and error bands found from voltages are similar to those found from fast-dots images. The error bands for the positive and negative ends of the chop are similar.

If this test with HIPO had been a verification of requirements in SOF-1011 Revision 7 for Verification for Early Science, the secondary mirror would not have met the settle time requirement in section 3.3.14.3.6: "*Chop settling time:<=5ms for <1' chop; <=7ms for 4' chop; <=10ms for 10' chop*". The LabView data and the fast-dots images show that the settle time for a 1' chop is 13ms, and for a 10' throw the settle time is on average 35ms. Had this test been a verification of section 3.3.14.3.5: "*Chop end point stability <= 1% of chop amplitude (or 0.2", whichever is greater)*" the secondary mirror would have met the stability requirement.

Next Steps:

Tune up the TCM controller for faster settle times, and retest settle time using LabView equipment.

Part 3: FCM focus range

Introduction:

This analysis task verifies that the focus range of the FCM is sufficient to meet the SOF-1011, Rev 7, focus range requirement. The required range of the FCM T axis is derived using a ZEMAX model of the SOFIA telescope together with the 19 mm offset of the HIPO focal plane from the nominal position, and the required ±600 mm back focus range relative to the nominal focal position, which is 300 mm forward in the aircraft from the SI mounting flange.

Data Acquired:

The T-axis position for the best HIPO focus and its temperature dependence was determined in TC-HIPO-07 for the SiC secondary mirror. This corresponds to the secondary mirror position for a back focus position 319mm forward of the SI mounting flange. The observed T axis positions for HIPO focus as a function of temperature follows the relationship:

$$t = 620 - 15.6T \qquad \text{(TC-HIPO-07)}$$

where t is the T axis position and T is the temperature in degrees C. Following the test plan, we use this to calculate the T axis position to focus HIPO at +30C and -40C (Table 3.3-1).

Table 3.3-1: Extrapolated HIPO focus positions

Temperature	T axis position
+30 C	+ 152 microns

-40 C	+ 1244 microns

Results:

The secondary mirror position in a ZEMAX model of the telescope was found for several back focus positions, and these secondary positions were converted to offsets from the secondary position for the HIPO back focus of 319 mm forward of the SI flange. A small error was found in the ZEMAX file used in development of the test plan, so these positions differ slightly (up to 15 microns) from those presented in the test plan. The T axis positions for HIPO focus at the temperature extremes given in Table 3.3-1 were then used to calculate the offsets from nominal HIPO focus to the other back focus positions at the two temperature extremes. These results are presented in Table 3.3-2.

Table 3.3-2: T Axis Positions vs. Back Focal Distance

Back Focal Position	HIPO Focus T offset (μm)	T position +30C (μm)	T position -40C (μm)
600 mm aft	+2943	+3095	+4187
300 mm aft	+1453	+1605	+2697
Nominal focus	+83	+235	+1327
19 mm forward	0	+152	+1244
300 mm forward	-1181	-1029	+63
600 mm forward	-2350	-2198	-1106

Conclusions:

The extreme back focus positions, ±600 mm from the nominal focal position, can be reached at both temperature extremes since the T axis limits of the FCM are ±5000 microns. If this HIPO test had been a verification of the requirements in section 3.3.7 (a), the secondary mirror would have met the requirement.

Next Steps:

None.

Part 4: Chop endpoint stability and image quality on the sky at night

Introduction:

This tests measures in-focus chopped image quality, while tracking, on the sky at night. Image quality will be measured for a 10 arcmin chop amplitude and compared with expected image quality calculated from the results of the Shack-Hartmann tests TC-HIPO-05.

Data Acquired:

On December 13th, , 41 two-second images were taken of a star at night; 10 images at each end-point while chopping, 10 static images at each end-point, and one image at the center point.

Data Analysis:

Compared ZEMAX artificial star images to images of a real star taken while chopping and while stationary at the center and 10 arcmin chop position.

Results:

Static images at negative endpoint of 10 arcmin chop:

From one image to the next, the peak brightness moves by at most 0.2% of the chop throw.

Average IQ measured in vertical direction is 6.34 arcsec, and in the horizontal direction is 5.96 arcsec. The real star image closely resembles the ZEMAX model, and is comatic. Chop angle appears to be 51 deg on HIPO.

\

Comparison of Zemax model and actual static image at negative endpoint of 10 arcmin chop:

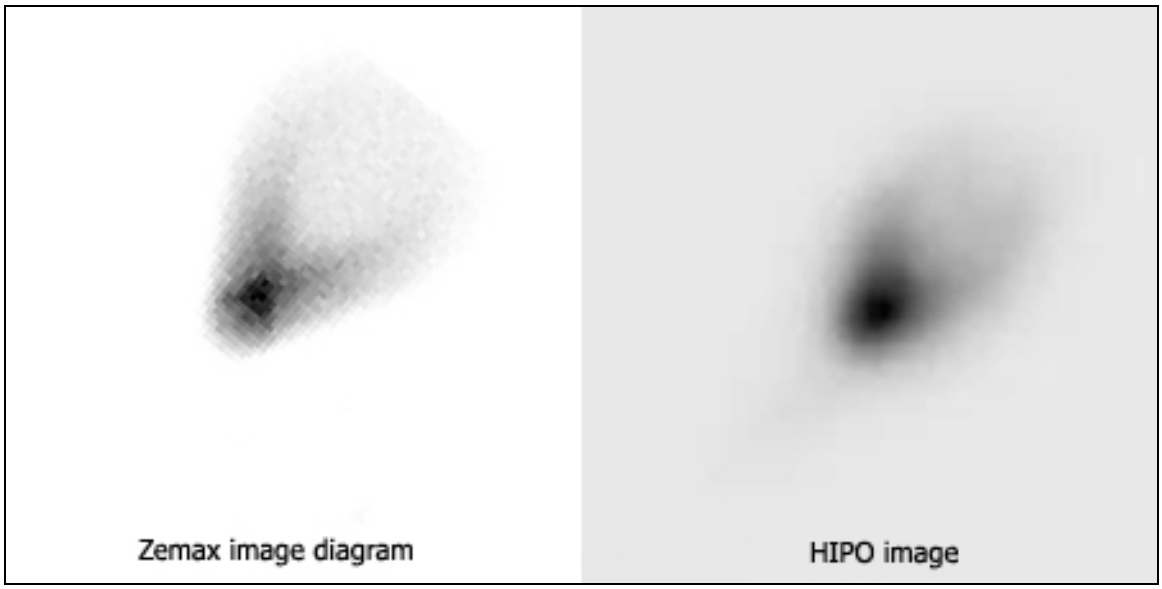

Negative endpoint of 10 arcmin chop, while chopping:

From one chopped image to the next, the peak of brightness moves around by at most 0.19% of the chop throw. The average IQ in vertical direction is 6.6 arcsec, and in the horizontal direction is 6.12 arcsec. Subtracting an average of the ten static images from

the average of the ten chopped image shows overshoot of about 70 pixels, or about 23 arcsec on the sky. 23 arcseconds on the sky corresponds to 85.7 mirror arcseconds, or 0.68 volts. The static and chopped images were slightly misaligned.

Average of chopped images, and result of chopped minus static images (negative endpoint)

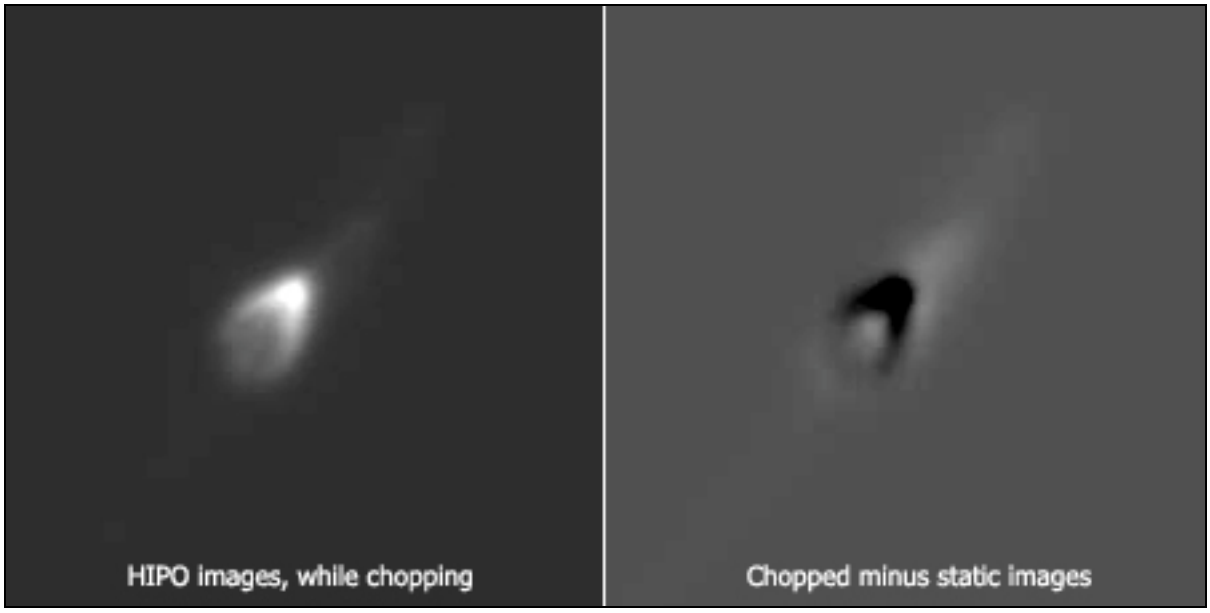

Static images at positive endpoint of 10 arcmin chop:

The peak brightness moves by at most 0.16% of commanded chop amplitude from one static image to the next. The average IQ in vertical direction is 6.75 arcsec, and is 5.98 arcsec in the horizontal direction. The real star image closely resembles the ZEMAX model, and is somewhat comatic.

Comparison of Zemax model and actual static image at positive endpoint of 10 arcmin chop

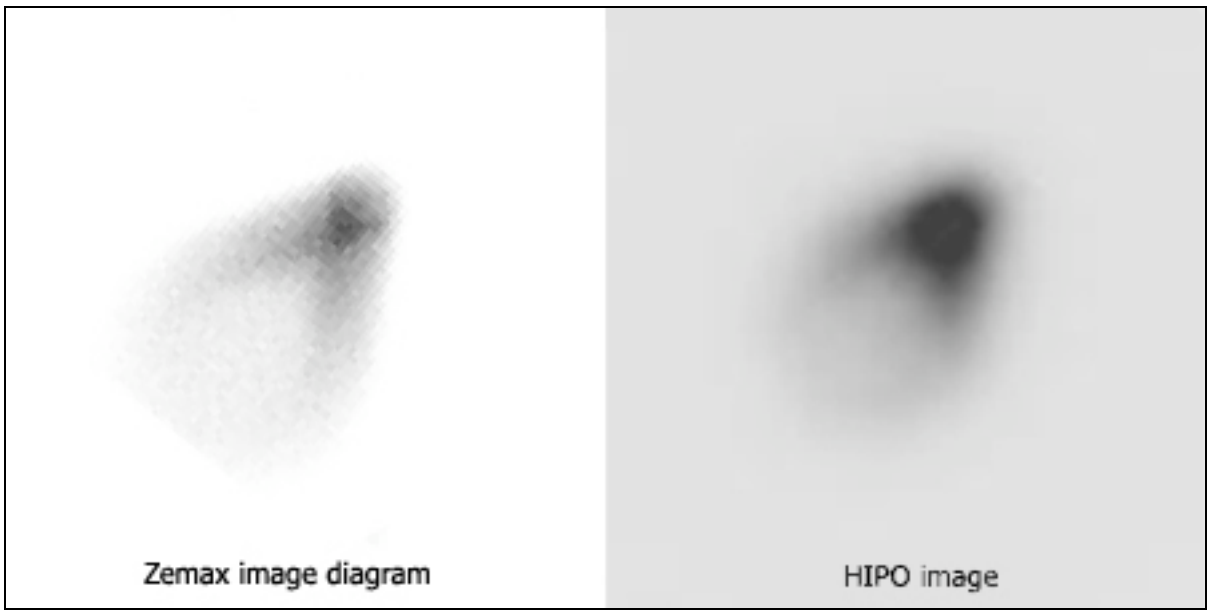

Positive endpoint of 10 arcmin chop, while chopping:

From one image to the next, the peak of brightness moves around by at most 0.47% of the chop throw. The average IQ measured in vertical direction is 7 arcsec, and is 6.36 arcsec in the horizontal direction, on average. Chop angle appears to be 51 deg on HIPO. Subtracting the average of ten static images from the average of the ten chopped image shows overshoot of about 70 pixels, or 23 arcsec on the sky, in the direction of the chop.

Average of chopped images, and result of chopped minus static images (positive endpoint)

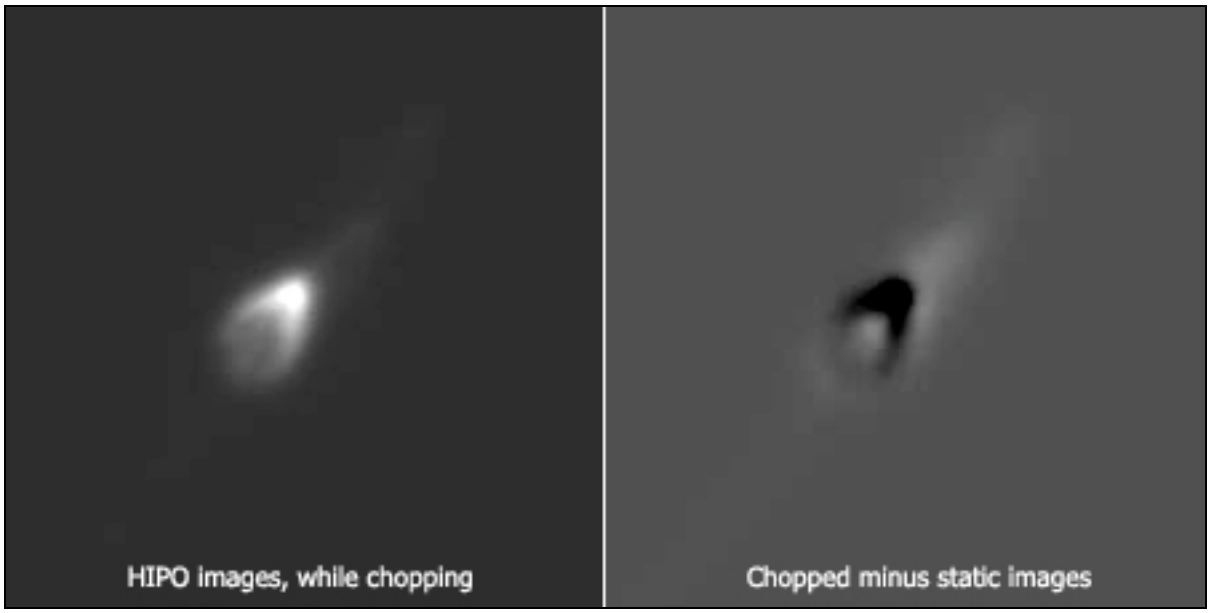

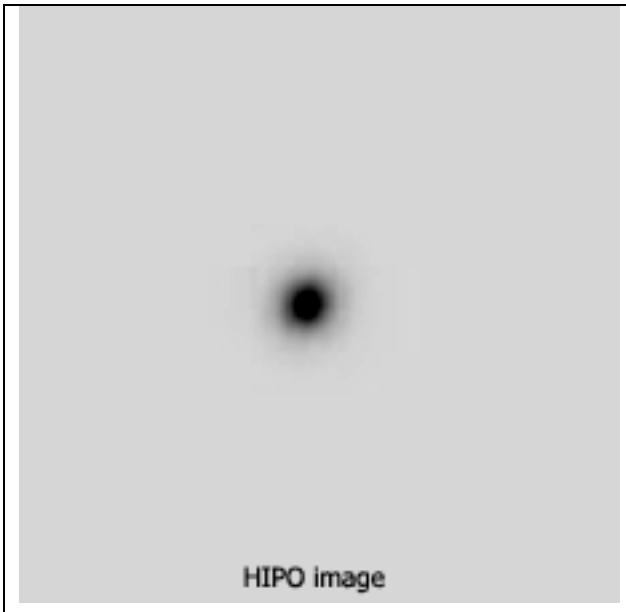

Vertical FWHM: 8.48 pixels, 2.77 arcsec

Horizontal FWHM: 8.26 pixels, 2.70 arcsec

Conclusions:

If this HIPO image quality check had been performed with FORCAST at 41000 feet, the mirror would have met the requirement in section 3.3.4.1/Early Science #69: "*On-Axis image quality <= 5.3"*". The on-axis image quality measured on the ground with HIPO is 2.77 arcsec.

Next Steps:

Modifications of the SMA servo system should be evaluated on the basis of early science performance requirements. Compete testing of the SMA system should occur prior to the early science flights with FCAST and GREAT. These tests can rely upon previously developed testing procedures.

TC-HIPO-04: Gyro Drift Trim and Residual Drift Measurement

Preface:

This test is intended to measure the uncompensated gyro drift, to measure residual gyro drift when drift is compensated and to evaluate the drift estimation algorithm implemented in the ATCU. The drift estimation algorithm is enabled when tracking is initiated. The test was done at the beginning of observing and from time to time as needed during the night to reduce gyro drift. The drift was estimated by the internal algorithm or by recorded HIPO centroids.

The first part of this report presents the gyro drift values that were measured over the five day test period. The analysis also includes data that were recorded during the TA standalone line operations.

The second part of this report focuses on the analysis and improvement of the internal drift estimation algorithm. It is spilt into an analysis section for the EL/XEL drift estimation and a section for the LOS drift estimation.

Part 1: Measured gyro drift

Introduction:

This section presents the measured drift values. Especially for the alignment measurements when drift has a significant effect on the results, the measurements were repeated frequently. Before the measurements were performed, the residual drift was preferably measured by HIPO and manually put into the ATCU to compensate for it. While conducting the tests, it seemed that the drift varied over the course of the measurement considerably. Thus, the drift measurements were repeated frequently to have reference data available for post-test analysis. It turned out that apparent drift changes are also due to slowly changing control deviations (TC-HIPO-06) and flexures (TC-HIPO-10).

Data Acquired:

Table 4-1 summarizes the drift measurements that were analyzed using HIPO images or recorded FPI centroids. It shows the UT date and time and the HIPO images sequence number and a short description of the drift measurement type. In the data description, “uncompensated” means that no drift values were implemented to compensate for the drift. “Tracking” means that the telescope was tracking on a star and constant position information was fed back into the control loop to compensate for any deviations. “Positioning” means that centroids were recorded but no position information was fed back (tracking is off).

Table 4-1. Summary of analyzed drift measurements.

Test run	Date UT	UT	HIPO OS	Description
1	20081211	06:07:14	53	uncompensated, image saturated, no FPI centroids available
2	20081211	06:48:07	60	TRC positioning with ATCU estimated drift values, no FPI centroids available
3	20081211	07:27:54	63	TRC positioning, drift values in ATCU (from HIPO centroids)
4	20081211	09:02:14	151	TRC positioning, drift values in ATCU (from HIPO centroids)
5	20081211	10:43:47	289	TRC positioning, drift values in ATCU (from HIPO centroids)
6	20081211	11:32:34	298	TRC positioning, drift values in ATCU (from HIPO centroids)
7	20081212	04:44:42	19	uncompensated
8	20081212	05:04:22	21	TRC positioning drift values in ATCU (from ATCU)
9	20081212	06:49:14	41	TRC positioning, drift values in ATCU (from HIPO centroids)
10	20081212	07:37:05	52	TRC positioning, drift values in ATCU (from HIPO centroids)
11	20081213	03:54:06	61	TRC positioning with day old drift values
12	20081213	05:50:01	104	TRC positioning, drift values in ATCU (from HIPO centroids)
13	20081214	08:03:21	75	TRC positioning, drift values in ATCU (from HIPO centroids)

Data Analysis:

The data analysis for the drift measurements is very straight forward. The HIPO and FPI centroid data are fitted to a linear curve separately for column and row pixels. The measured drift value is the slope of this curve.

Results:

The absolute drift values that are measured in EL and XEL are shown in Figure 4-1. The absolute drift values are composed of the implemented drift values in the ATCU and the measured residual drift values. The drift values are shown for 13 test runs over five days of the HIPO line operations. The absolute drift values have an average offset of 0.14 arcsec/s in the EL- and -016 arcsec in the XEL-direction. The day-to-day variation of the drift values is about an order of magnitude smaller. The average absolute drift values are similar to those measured during the TA standalone line operations in November 2008. The data are shown in Figure 4-2. Measurements were taken at different elevations (test run 34° and 57°) and with different alignment matrices. Here, the uncompensated measurements are compared to compensated measurements with the former drift estimation algorithm. However, this algorithm was improved for HIPO line operations and is analyzed in part 2.

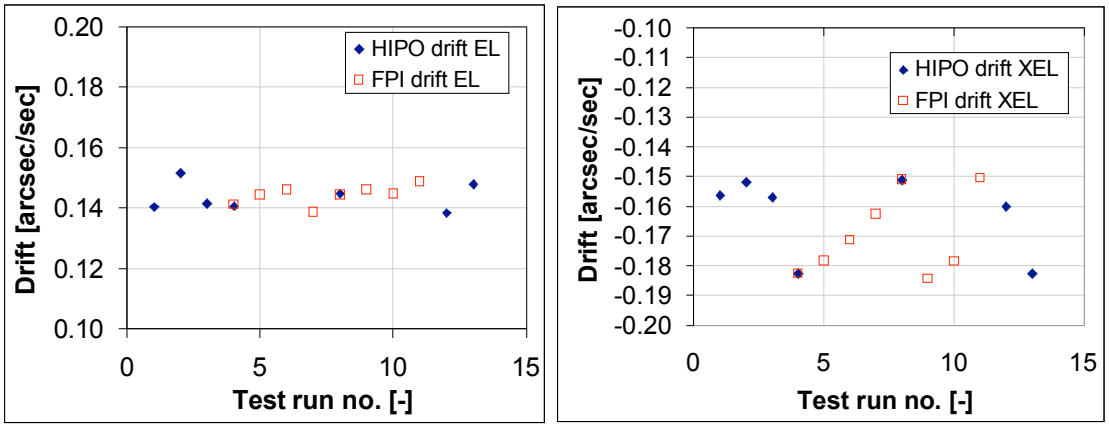

Figure 4-1. Day-to-day absolute drift values measured in HIPO and FPI for EL and XEL.

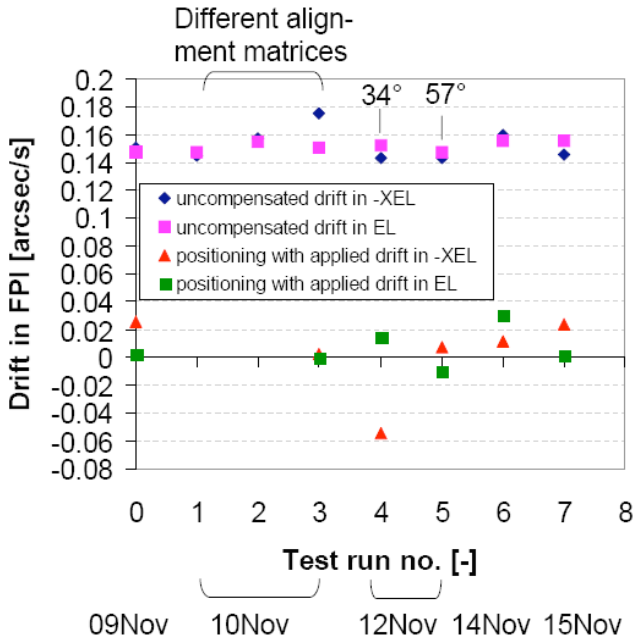

Figure 4-2. Day-to-day drift variation measured in FPI during TA standalone line operations in November 2008. Uncompensated measurements are compared to compensated measurements with former drift estimation algorithm.

Part 2: Drift estimation analysis

Introduction:

This section analyses the corrections messages that are sent from the Tracker to the TASCU. The TASCU forwards all ATC_POS_CORR messages to the ATCU which then process the messages and calculate a drift estimate. No additional HIPO data were acquired during this evaluation.
The main purpose was to evaluate the rewritten ATCU software of the drift estimation algorithm. The status of the estimation performance was largely unknown before these Line Operations. From the ICD the algorithm is advertised as a completely self-contained subsystem that exposes only minimal command interface and status information to the MCCS. In reality this algorithm has never been tested under various conditions and was usually tweaked to improve performance. Therefore, it is extremely important to implement a highly robust system that just behaves as expected.
We used a StethoScope Interface to interact with the drift estimator. Most notable parameter were the stable Counter to specify after how many corrections the drift is considered stable and applied to the quaternion integration, the Kalman Gain that basically controls how quick the algorithm adopts to new drifts, and the currently estimated drift (in radian per 400 Hz cycle).

From the set of drift measurements only a subset is analyzed here:

No.	Date and Time [YYYMMDD, UT]	Comment
1	20081212 04:32-04:34 (4.54-4.575)	EL-XEL drift estimation
2	20081212 08:04-08:22 (8.07-8.36)	EL-XEL and LOS drift estimation

EL & XEL drift estimation:

Tracker corrections
In the first tracking run, drift estimation was initiated with the default setting, i. e. no drift compensation, and the Kalman gain set to 1. The TA was brought into position via a TRC_FD_TRC_OFFSET command. When settling on the star was finished the TASCU House Keeping indicates a LOCKED state and the Tracker started to send EL & XEL Theta corrections ($\Theta_{EL/XEL}$). The first 3 were IMMEDIATE which were applied in full scale to the Fine Drive attitude. The following 85 $\Theta_{EL/XEL}$ were commanded as IMMEDIATE_ESTIMATE.
The greatly improved response time of the new Fine Drive controller made it necessary to apply a 0.5 damping gain in order to reduce the bumpy behavior of the TA which could lead to an overshoot or in a worst case even trigger a oscillation resonance within the Tracker loop. Introducing a gain is in accordance with the TA_MCCS_F ICD because it is not specified that the TA has to execute a full move (as opposed to move commands such as TRC_FD_TRC_OFFSET). On the other hand a very small gain might contribute to a slower convergence of the drift estimation.

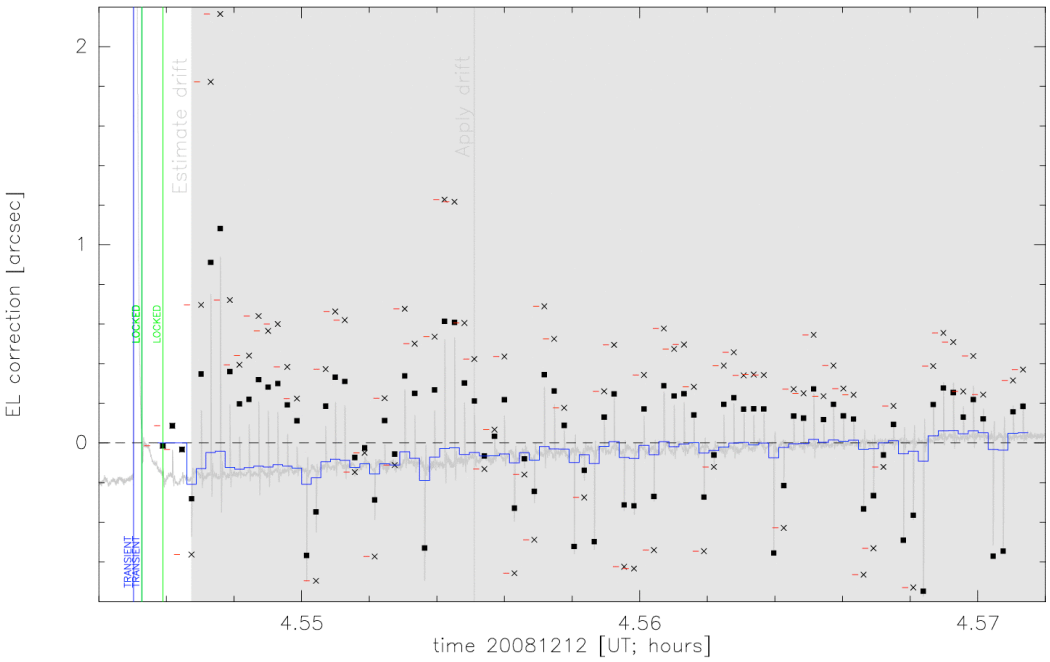

Figure 4-3. The shaded area indicates the period when the estimation started and when the estimation was applied (gray vertical line). The crosses with the red tail show when the Tracker offset was taken and how large the offset was. The black squares show how much was applied to the Fine Drive (here 50%). The gray curve with the periodic spikes indicates the controller deviation. The blue line indicates the controller deviation averaged over 500msec and that was used to calculate a better drift estimate.

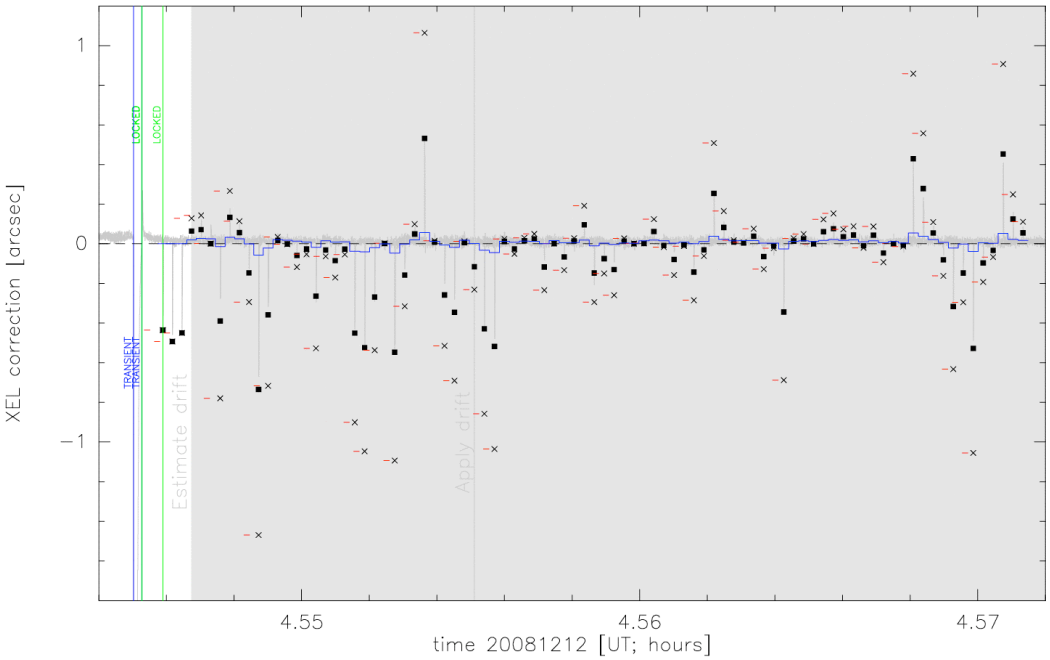

Figure 4-4. Same description as for Figure 4-3 but for the XEL axis.

Controller deviation

During the tracking test, the Fine Drive controller was not able to move the TA exactly to the commanded attitude. When the LOCKED status was reached (stable within 1" for at least 1 second) the TA remained at an offset of up to -0.2". This effect was observed to happen typically after a move as e.g. from the TRC_FD_TRC_OFFSET command. The offset is mainly visible in the EL axis where it is slowly converging to 0. It was found that the periodic centroid updates from the Tracker with the subsequent attitude adjustments (visible as small spikes on the gray curve in Figures 4-3 and 4-4) did not help to reduce this offset.

This behavior is probably caused by the algorithm itself. Although the offset has been measured, it wasn't taken into account in the original tracking correction and drift estimation code. As opposed to the FD controller, the Tracking controller is supposed to correct any deviations from the current star positions to the actual TA position. Therefore, the Tracker provides offsets that include the control deviation – in the nominal case the star is at the actual TA position the Tracker would report the FD control deviation but not 0 as desired. Hence, the offset must be taken out before the correction move and the Gyro drift estimation is executed. Otherwise this will causes a conflict between the two controllers (see Figure 4.5).

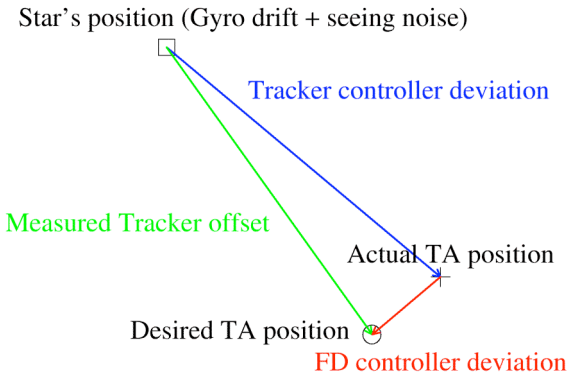

Figure 4-5. Responsibilities of the Fine Drive and Tracking Controllers: The first one tries to move the actual TA position toward the desired TA position while the latter one's strategy is to move the star toward the actual TA position. If only the Tracker offset is corrected then the desired TA remains at an offset to the star.

Drift estimation

The first objective of this test was to evaluate the rewritten drift estimation algorithm of the ATCU and seconds, an improved algorithm was searched and evaluated. In general, the drift estimation worked very well. The estimation started with immediateGain=estimateGain=0.5, i. e. only half of the reported Θ-offset was corrected and also only half the value was considered in the estimation. While the estimation was

active the Kalman gain was reduces by *gain/(1+gain)* with every $\Theta_{EL/XEL}$. This is equivalent to a running average over the slope of all previous $\Theta_{EL/XEL}$.
The algorithm started with first drifts of about 0.4 "/sec in EL and 0.1 "/sec in XEL and came down to the ±0.1 "/sec level of the final value after less than 20 corrections. At this level the drift is stable enough to be taken over into the correction loop but the drift stability requirements are not yet met.
After 30 IMMEDIATE_ESTIMATE messages, the ATCU took over the estimated drift which started at 0.18 "/sec in EL and -0.12 "/sec in XEL. It further changed the estimation state from TRANSIENT to STABLE. Figure 4-3 and 4-4 shows that the offset scatter is better centered on 0 after the drift was applied.
The recommendation here is to change the stable detection from the fixed stable counter to a standard deviation measure. As ATCU has presently only the two states TRANSIENT and STABLE it seems reasonable to add a status SETTLE to indicate the usage of the estimate but also to make clear that the drift is not yet stable enough to do longer measurements without tracking.
At the end, at about 90 seconds into the test, the estimates settled down to 0.158±0.046 "/sec in EL and -0.155±0.016 "/sec in XEL. At this level the error ellipsoid reaches 1" uncertainty in less than a minute. It should be noted at this point that the goodness of these estimates depend on the duration of the test and therefore the 90 second result is not representing the best achievable performance.
Implement a sigma-type estimation error that considers the first and the last estimation in order to extrapolate the error at a later time. When the error exceeds a threshold the drift should change from STABLE to TRANSIENT to inform the operator that a new estimation should be imminent.

Code analysis
As a first step to improve the ATCU code, the original code was reproduced and verified. Figure 4-6 and 4-7 show a perfect overlay of the black and green curves (ATCU vs. offline analysis code). Based on this result the analysis code was altered to include the controller deviation. The controller deviation was averaged over the duration of the imager exposure time and then added to $\Theta_{EL/XEL}$. Only the EL component was significantly changed and Figure 4-6 shows a slightly smaller estimate of 0.135±0.052 "/sec. In XEL the value remained almost unchanged: -0.152±0.016 "/sec.
If the controller deviation stays at an offset for a longer time it seems beneficial to subtract the averaged controller deviation.

Another aspect of the test was to evaluate the performance of the immediate gain. The present algorithm does not keep track of the initial position which makes it difficult to apply immediate moves with a gain while doing the estimation at the same time. To overcome this problem, a new algorithm is proposed that sums up all $\Theta_{EL/XEL}$ and measures the slope from the reference point to the actual position. As the reference point moves away from the actual position while the drift is applied to the inertial reference frame the used drift needs to be added to the reference point every time the drift offset is added to the IRF-TARF attitude. The slope can be calculated by the same Kalman filter

method over the last ~ 400 and the last ~ 200 corrections. This method works for both the EL/XEL and the LOS drift estimation (see next section), with and without an immediate gain factor, in the modes IMMEDIATE, ESTIMATE, and IMMEDIATE_ESTIMATE. Note that the ESTIMATE mode is just a special case of the IMMEDIATE_ESTIMATE with an immediate gain of 0.

Figures 4-6 and 4-7 indicate that the algorithm for the EL/XEL axes (shown under "proposed Drift") gives a smoother drift estimate than the previous method but also needs more time to adjust to the drift. The quality of the drift estimate mostly depends on the time between the first and the last measurement of the Tracker. Therefore, the performance would be similar if the Kalman gain would be a function of time rather than a function of the number of corrections.

Implement an immediate gain to smoothen the telescope reaction to an IMMEDIATE command from the Tracker in response to a deviation from the tracking object. Implement a reference point to keep track of all uncorrected IMMEDIATE moves and to deduce the real drift.

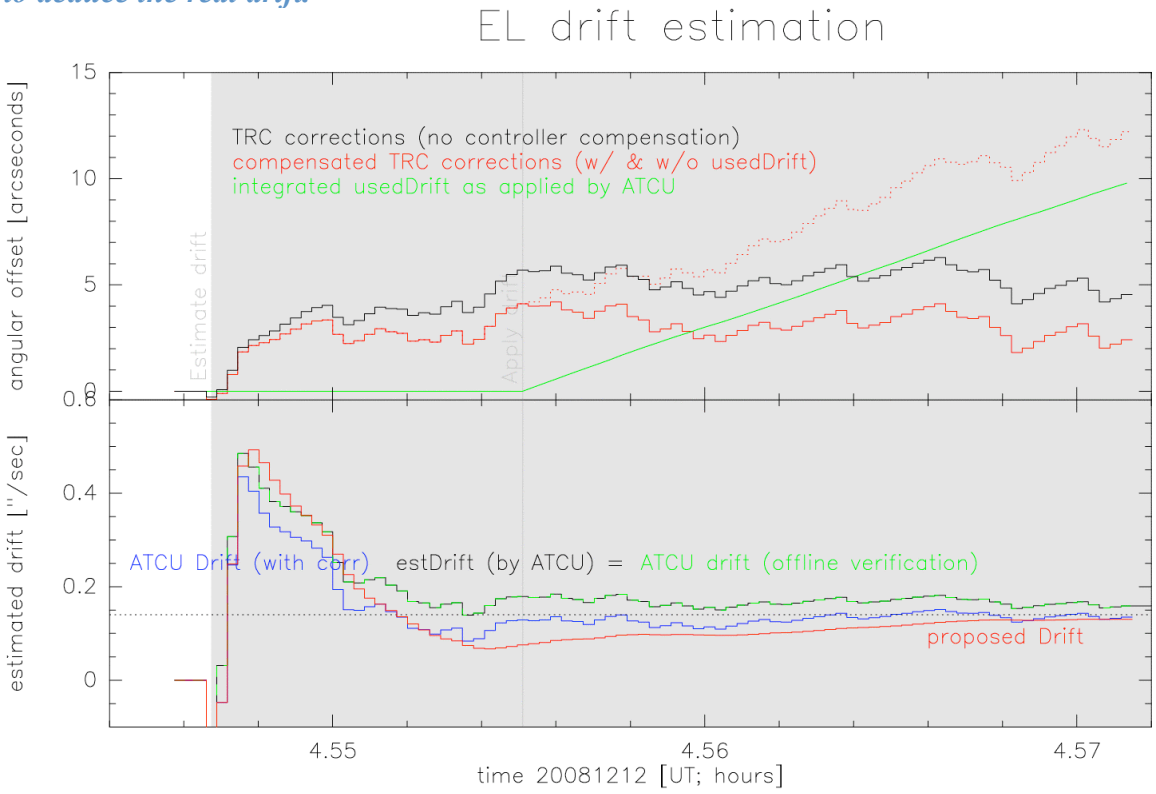

Figure 4-6. **Upper plot: Absolute angular offset with a reference set to 0 at the start of the Tracking. Integrating over all offsets gives the black curve which had no correction for the controller deviation. This correction was made for the red curves. The dotted part also corrects for the applied gyro drift (cf. green line).**
Lower plot: Shown are the various gyro drift rate estimates over time. The black-green dashed curve shows a perfect overlay between the drift as reported by the ATCU and the drift that was reconstructed from the Tracker offset shown in the upper plot. With the same algorithm but with controller compensation the blue curve is produces. A result from a different algorithm that basically measured the slope of the red+dotted curve in the upper plot is shown in red.

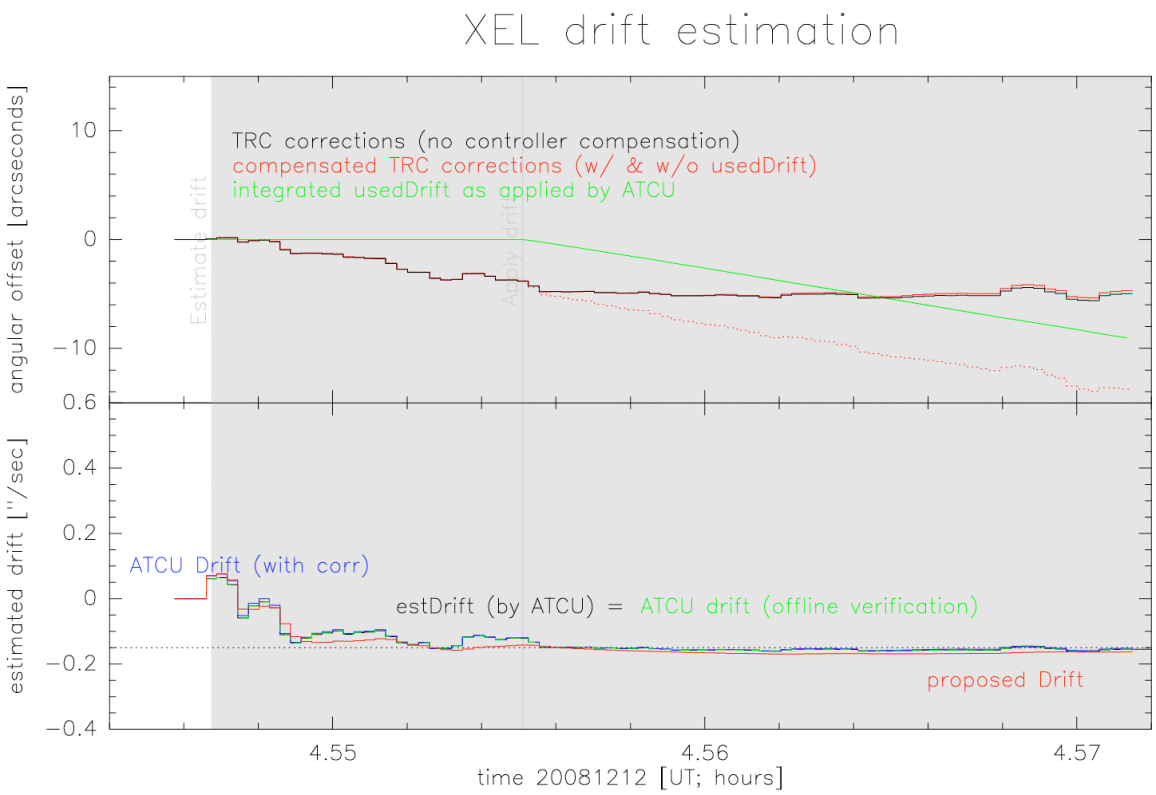

Figure 4-7. Same description as for Figure 4-6 but for the XEL axis.

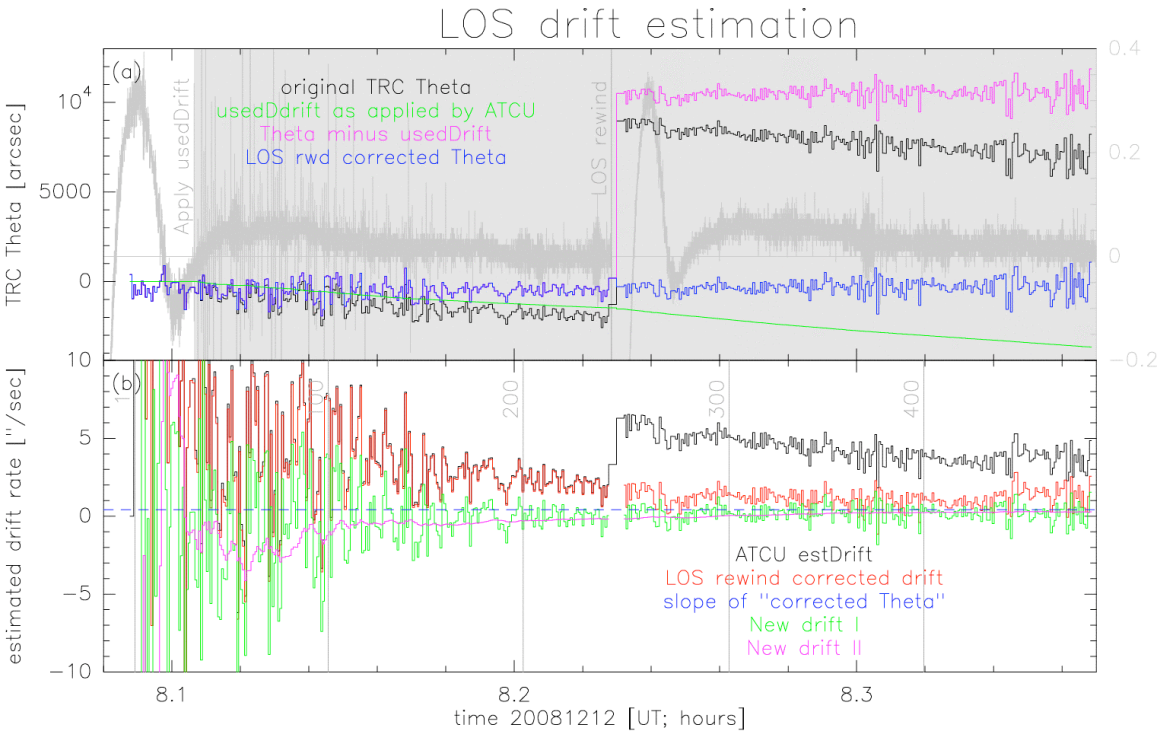

Figure 4-8. **(a) LOS drift corrections as sent by the Tracker in ROF_CALCULATE mode. In black the original data as sent by the Tracker is displayed. The pink plot shows the same data but corrected for the applied drift (green curve). The 3° LOS-rewind (incorrectly reported by the Tracker) was corrected in the blue curve. The gray curve illustrates the controller deviation (scale on right axis).**
(b) Measured LOS gyro drift rates. The drift as measured by the ATCU is shown in the black colored curve. The same algorithm but with the LOS rewind corrected is shown in red. The green curve shows a first attempt to improve the drift estimation. The second attempt (pink colored curve) uses the same algorithm that was proposed for EL/XEL. Vertical values show the number of received offsets.

LOS drift estimation:

Tracker corrections

A preliminary remark: The LOS drift estimation algorithm could not provide a useful drift estimate during this test. However, the test provided very useful data to improve the algorithm.
On Dec 12th between 8:05:19 and 8:22:08 the ROF_CALCULATE command was active. Two AOIs were setup on the FPI rather than the WFI to act as ROF centroids. The initially used LOS drift was 0 "/sec. One of the AOIs was used for EL and XEL tracking at the same time but the $\Theta_{EL/XEL}$ offsets are not analyzed here. Figure 4-8a shows the Theta angles (Θ_{LOS}) sent from the Tracker. After the initial estimation phase after the first 30 Θ_{LOS} measurements, the estimated drift was applied to the quaternion interaction beginning with 8:06:23. After this time the centroid corrections started to drift at the applied rate of about 4.2"/sec. As seen in the Figure the data were somewhat noisy and converged only slowly.

Drift Analysis

Because it is obvious that the estimated drift must be much smaller than the applied drift (usedDrift in Figure 4-8) the applied drift was subtracted out from the data in order to determine the uncompensated drift. This is shown in Figure 4-8a as purple line.

A 3° LOS rewind was initiated at 08:13:42 to evaluate the behavior of the system. After the rewind, the reported Θ_{LOS} offset jumped by 3°, while the estimated drift value jumped by a factor of ~4. The estimated drift continued to decrease but offsetted to again more than 5 "/sec. The preliminary source code analysis of this jump indicates that the Tracker actually stores the reference points in TARF rather than IRF which neglects the effect of a LOS move on TARF. For the purpose of this analysis the 3° were subtracted as shown as blue line Figure 4-8. With both the corrections for the used drift and the LOS rewind, the drift becomes stable between 0.41-0.49 "/sec (determined by a 1st order polynomial). The ATCU algorithm was able to stabilize the drift down to ~1.5 "/s before the LOS rewind took place after 247 Θ_{LOS} corrections (corresponding to a Kalman gain of 0.00405).

Correct a bug in the Tracker source code that caused LOS offsets to build up with every LOS rewind or other move.

In the course of this analysis it became obvious that also the ATCU algorithm has flaws. The algorithm basically considers the two last Θ_{LOS} and integrates over the difference and calculates the average by means of the Kalman-Gain. The estimateGain of 0.2 was not applied in LOS mode and cannot cause the slower convergence. A large error is propagated through this method and the drift has a slow convergence. If instead the average over the last n Θ_{LOS} is calculated the error is small compared to the result and the slope can be determined with a better accuracy. This approach is shown in Figure 4-8b in pink where running averages over all Θ_{LOS} (resp. the 2nd half of the Θ_{LOS}) were calculated. The slope between the two averages settled to 0.276 "/sec at the end of the test. This is almost equal to a 1st order regression fit to the Θ_{LOS} that gives 0.278±0.069 "/sec.

The LOS drift estimation should use the same algorithm as for the EL/XEL estimation.

The controller deviation in LOS was luckily not very pronounced during this test (cf. gray curve in Figure 4-8). It was therefore ignored.

LOS drift measurement

The drift estimate derived after the LOS test was affected by the LOS rewind and large overlaid drift compensation. It was important to obtain an independent measurement on the LOS drift. Because the drift rates in the two other axes are fairly well known an independent measurement is the measurement of the earth rotation. The average rotation rate is 15.0411 "/sec. Assuming a perfect orthogonality of the three Gyroscope units and a perfect compensation of the EL and XEL drift (0.148841 "/sec for EL and -0.150804 "/sec in XEL) the remaining rate error can be contributed to the LOS drift. To reduce the noise a rate integration was done over a few minutes. The results are shown in Figure 4-9. The residual drift was found to be 0.3218 "/sec in the first run which is in good agreement with the estimate above. After implementing the LOS drift a second run was done which shows a better agreement with the earth rotation speed. However, a another offset of of about 0.06 "/sec was found. This discrepancy probably falls within the accuracy

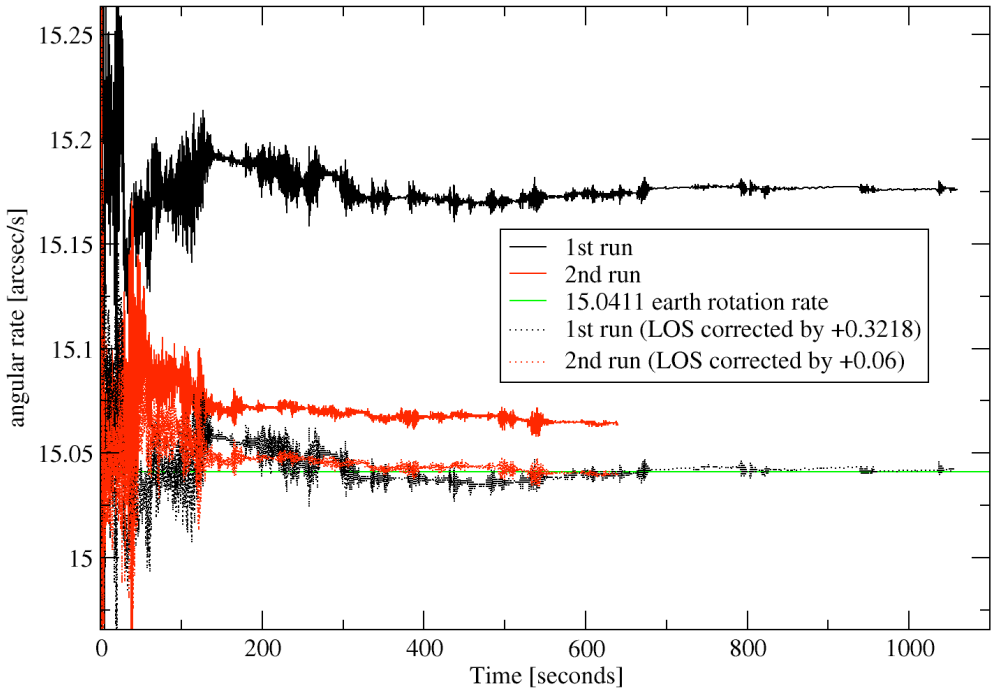

Figure 4-9. LOS drift measurement. Integrated angular rates should ideally sum up to the earth rotation rate. The discrepancy was measured and corrected (dotted lines). On the 2nd run the measured rate was used to correct the LOS drift.

Conclusions:

Part 1 of the report presents the absolute drift values as measured in HIPO and the FPI. A relatively high offset of about 0.15 arcsec/sec was observed in EL and also in XEL direction which was consistent over the course of the HIPO line operations and the TA standalone line operations. The variation of this offset is about an order of magnitude smaller.

Part 2 of the report presents the performance analysis of the drift estimation algorithm which is internal to the TA system. A set of recommendations were made how to change the algorithm and based on these recommendations an improved algorithm is presented and was tested offline on the measured data.

Next Steps:

1. Test the new drift estimation algorithm.
2. Investigate constant gyro offset.
3. Investigate influence of flexure during measurement.
4. Predict bias stability for typical observations.

TC-HIPO-05: Optical Alignment

Introduction:

This test determines the SMA FCM tilts and decenters required to achieve correct alignment of the telescope optics. Alignment is accomplished by nulling the effect of coma on images of the stars in the science instrument focal plane. Once aligned the integrated, as-built optical quality of the TA optics is determined. This determination is complicated by the presence of an astigmatic component in the TA optical system.

An incorrect secondary mirror decenter is well compensated by tilt. As a result we had to choose one of these parameters as fixed and vary the other one to achieve zero coma due to misalignment. Discussion regarding the theodolite/autocollimator alignment resulted in a decision to retain the tilt values from that alignment and vary the secondary decenter.

Data Acquired:

The primary Shack-Hartmann data were obtained on HD1687 (V=8.1, K0) on 10 December 2008 UT (See Table 5-1). Additional data obtained in support of TC-HIPO-07 on 11 December 2008 UT also relate to the alignment (see Table 7-2). The LED control image for the images in Table 5-1 was Observing Sequence (OS) 116.

Table 5-1 shows the data obtained, the secondary mirror positions, the coma and focus values, and derived SMA position changes. The final R and S values adopted are those for OS125 (shaded in Table 5-1). Note that the FCM rot_R and rot_S values were fixed at -400" and +270" respectively for the entire alignment process.

Table 5-1: Shack-Hartmann Alignment Analysis Results

HIPO Observing Sequence	UT	R	S	T	Z4 : Focus	Z7: Coma Y	Z8 : Coma X	delta R	delta S	delta T
115		-600	-400	450	7.8	3	-2.7	0	0	160
118		-600	-400	609	-2.48	1	-0.01	-280	-325	-66
119		-880	-725	543	1.1	-0.4	0.1	80	162	12
120		-800	-563	555	0.1	0.24	0.17	-12	-126	-10
121		-812	-689	545	*	*	*	0	0	0
122		-812	-689	545	0.69	-0.15	-0.15	-9	90	3
123		-821	-599	548	0.72	0.1	0.03	-20	-41	3.5
124		-841	-640	551.5	0.72	-0.08	-0.01	19	28	3.5
*****125*****		**-822**	**-612**	**555**	**0.22**	**0.05**	**0.03**	**-5**	**-26**	**-7**
126		-827	-638	548	0.38	-0.04	-0.03	0.5	24	-4

* The analysis results for OS121 were anomalous so OS122 is at the same SMA settings.

Data Analysis:

The Shack-Hartmann data are analyzed by first finding the centroids of the lenselet images of both the calibration LED and the star, and registering the two spot patterns to a common reference. The identified LED and star patterns are shown in the analysis GUI pictured in Figure 5-1, in the top two graphics windows left and right, respectively. Optionally, the star pattern image may be flat-fielded to remove large scale gradients in the background, but the Site-9 sky was dark and uniform enough to make this step unnecessary. Next, the deviation of the star spots relative to the LED spots are calculated, with options to remove focus or preserve tilt in the wavefront solution. The wavefront is represented by an 11-term set of Zernike polynomials (Noll, 1976), through 3rd-order spherical aberration. A closed-form solution of the wavefront gradient is utilized to solve a non-linear least squares fit of the gradient to the measured ray deviations. The resulting 11-term Zernike polynomial fit to the wavefront is displayed in the blue table (left center, Fig. 5-1), and used to generate model ray deviations, which are depicted graphically in direct comparison to the measured deviations along with the RMS of the fit in the GUI lower center window. Simulated focal plane spot patterns generated from the spot deviations and the corresponding wavefront fit are plotted in the lower right window, with the FWHM's of each spot pattern calculated from 1.6 * (RMS spot radius). Finally, the derived secondary (R, S) decenter *or* tilts to correct coma, and (T) piston to correct focus, are shown in the green tables, lower left.

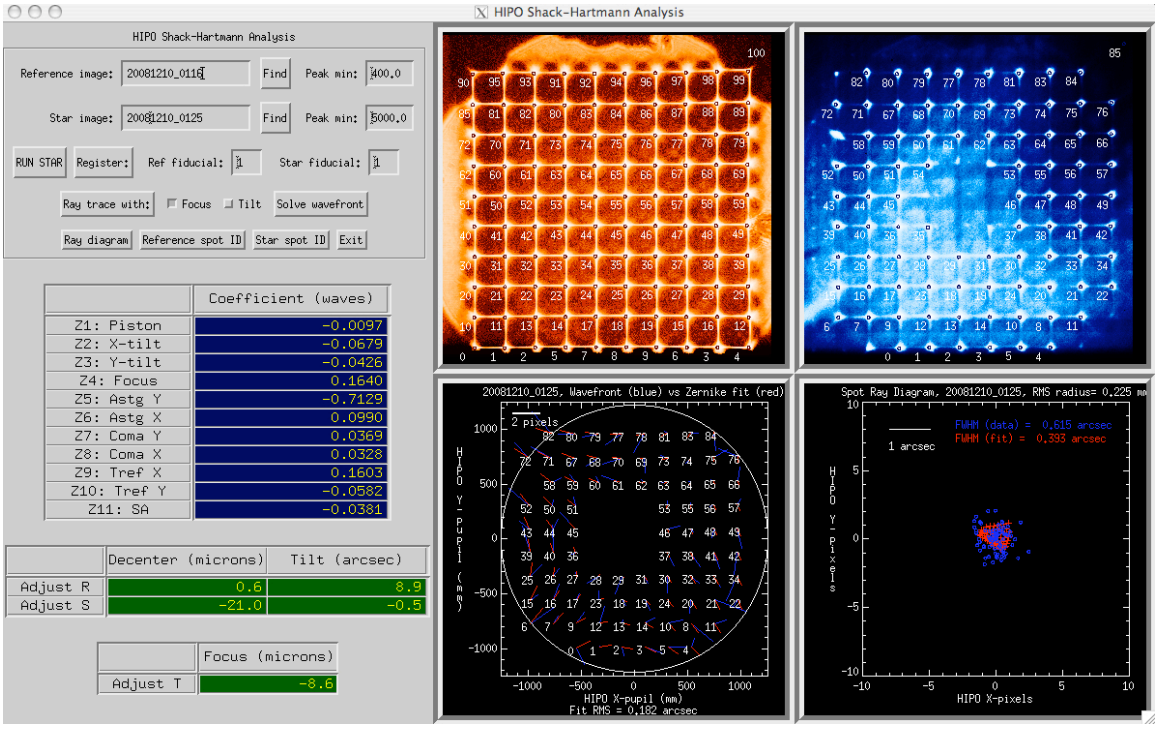

Figure 5-1: Shack-Hartmann analysis screen shot for OS125. This shows the results of the adopted alignment. See text for further discussion of this figure.

The Shack-Hartmann results presented in the next section show significant astigmatism in the OS125 adopted alignment results. Because of this an additional analysis was carried out using the ZEMAX ray tracing program to understand whether this is due to the field-dependent astigmatism that results when secondary mirror tilt is compensated with decenter or whether there is field-independent astigmatism due, for example, to a stressed optic in the system. Analysis of images using the IRAF image processing package was also done for comparison to the ZEMAX results. The details of this work are presented in the next section following the table of aberrations from the OS125 alignment.

Results:

Adopted Alignment:

The Zernike coefficients found in the OS125 analysis are presented in Table 5-2. With the exception of Z5 (X Astigmatism) the aberrations are on the order of 0.1 wave. The astigmatism is large by comparison and caused us to investigate further to determine its cause. *It should be pointed out that the minimum blur circle for this amount of astigmatism is about 0.8" with 80% enclosed energy in a 0.7" diameter circle and 50% inside a 0.55" circle. Leaving the optics as they are is perfectly acceptable for Early Science.*

Table 5-2: Zernikes for adopted alignment condition (OS125)

Zernike Name	Zernike Term	Value (Waves)
Z1	Piston	-0.009
Z2	X Tilt	-0.087
Z3	Y Tilt	-0.088
Z4	Focus	+0.174
Z5	X Astigmatism	-0.719
Z6	Y Astigmatism	+0.138
Z7	X Coma	+0.086
Z8	Y Coma	+0.055
Z9	X Trefoil	+0.136
Z10	Y Trefoil	-0.081
Z11	Spherical	-0.069

Astigmatism Investigation:

The observed astigmatism could be caused by either an incorrect secondary tilt (compensated by decenter) or by an astigmatic element in the TA optical system. The misalignment case would result in field-dependent astigmatism while the astigmatic element would cause field-independent astigmatism. This was investigated in some detail by examination of Shack-Hartmann analyses from a number of additional images

to establish the reality of the astigmatism, ZEMAX modeling to define the optical behavior for the two causes of the astigmatism, and examination of in-focus HIPO images at various field positions to discriminate between the two possible sources of the astigmatism.

Table 5-3 shows results from several Shack-Hartmann images, some taken at about the same time as OS125 during the optical alignment and some taken the following night in support of TC-HIPO-07. Several entries are highlighted. The X coma entry for OS123 should be ignored since we were still in the process of aligning the secondary. The blue highlighted fields are outliers that have no clear explanation. The main conclusion to draw from this table is that the substantial astigmatism seen in OS125 is real. The average Z5 coefficient is well defined at -0.61 ±0.11 waves and Z6 is less well defined at +0.3 ±0.18 waves. The Z6 average is affected by two unusually low points; if they are eliminated the average value is closer to 0.4 waves. In any case, the astigmatism is real. There may be something going on with the Trefoil (Z9 and Z10) coefficients, but this is less certain. The majority of the results suggest small Trefoil values, but there are a few outliers at higher values. The coma and spherical aberration terms are uniformly small.

Table 5-3: Zernikes for Several Shack-Hartmann Images

OS	14	49	292	123	124	126	125
Date	20081211	20081211	20081211	20081210	20081210	20081210	20081210
Z1 (Piston)	-0.0180	-0.0159	-0.0037	-0.0050	-0.0101	-0.0127	-0.0097
Z2 (Tip)	-0.0985	-0.1394	-0.0590	-0.0909	-0.0164	0.0372	-0.0679
Z3 (Tilt)	-0.0064	-0.0802	-0.1845	-0.1772	0.0063	0.0424	-0.0426
Z4 (Focus)	0.3232	0.3849	0.4548	0.6072	0.6259	0.3491	0.1640
Z5 (X Astig)	-0.6744	-0.7305	-0.4909	-0.6533	-0.6975	-0.8515	-0.7129
Z6 (Y Astig)	0.2868	0.4331	0.5936	0.2419	0.0967	0.4045	0.0990
Z7 (X Coma)	0.0052	0.0434	0.1376	0.1264	-0.0278	-0.0480	0.0369
Z8 (Y Coma)	0.0531	0.0940	0.0361	0.0490	0.0099	-0.0308	0.0328
Z9 (X Trefoil)	0.3903	0.3409	0.0741	0.1205	0.1409	0.2155	0.1603
Z10 (Y Trefoil)	0.0389	-0.0711	0.0341	-0.1940	-0.3604	-0.1253	-0.0582
Z11 (S.A.)	0.0073	0.0352	0.0207	-0.0232	-0.0057	0.0496	-0.0381

The ZEMAX model of the TA and HIPO red side optical system was used to investigate the imaging effects of misalignment vs. an astigmatic optic in the TA. This model was modified by addition of a Standard Zernike Phase surface at M1 to allow modeling of an astigmatic optical component in the telescope. Coordinate breaks to model the tilt and decenter of the SOFIA secondary mirror were already present. A coordinate break to simulate a body re-pointing of the telescope was added, and the merit function was modified to force the central field to remain fixed at the center of the TA flange. Failure to take these last two steps causes ZEMAX to optimize and discover a very good solution for the tilt/decenter compensation – *but at the wrong location in the focal plane*.

The spot diagrams shown in Figure 5-2 show the imaging behavior across the HIPO field of view when 0.7 waves of astigmatism are imposed on the optical system through misalignment (left) and an astigmatic optic (right). The image shape and size are the same for the central field (where the HIPO Shack-Hartmann data are taken) but there is strong field dependence in the misalignment case and essentially none in the other case.

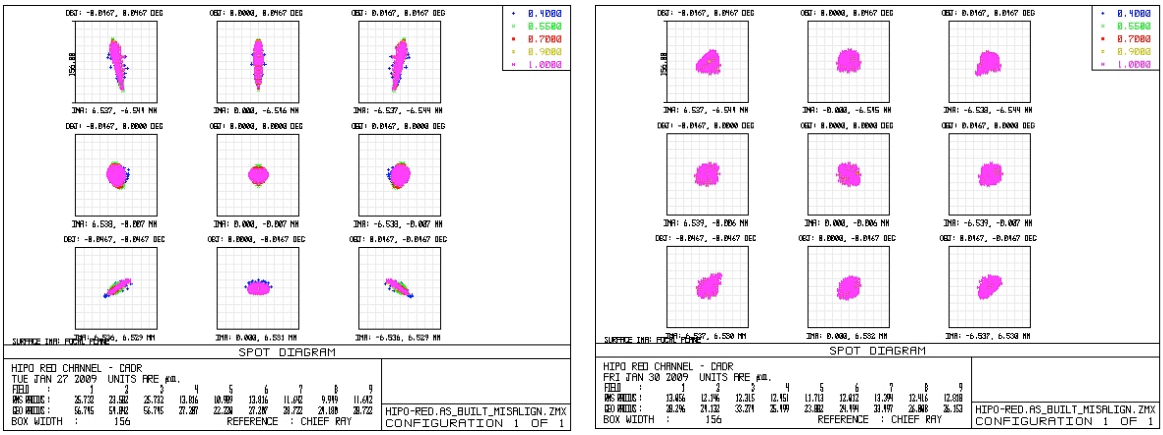

Figure 5-2: Spot diagrams for 0.7 waves of astigmatism introduced by secondary mirror misalignment (left) and an astigmatic optic modeled by a Zernike surface (right). The boxes surrounding the individual images are 4" square. The fields correspond to the corners, center of the edges, and center of the HIPO field.

The amount of misalignment required to produce this amount of astigmatism is a tilt of 0.446 degrees and a compensating decenter of 3.49 mm. These are truly enormous errors compared to the uncertainties in the theodolite/autocollimator alignment procedure that was carried out prior to the HIPO observations. This is our first clue that misalignment is not the primary problem.

We then examined in-focus HIPO images to see if field dependent astigmatism was detectable. The best images for this purpose were EL and XEL gyro alignment images, since star images were placed near the four corners of the HIPO field in these images. The images examined were OS54-72 on 20081212 UT. As it happened, the frames with star images in the lower left corner have a second star closer to the center of the frame, and these images were analyzed also. These were all 5 frame basic occultation frames but only the first frame in each series was examined using the *imexam* function in IRAF. The results of this analysis are given in Table 5-4.

In Table 5-4 the "Corner" entry indicates lower left, lower right, upper left, upper right, and the aforementioned position near the middle of the frame. The FWHM of the image is given in pixels (at a pixel scale of 0.325 "/pixel), the ellipticity is a number indicating elongation of the image, and PA is the angle of the major axis of the elongated image.

The ellipticity is generally small, but not zero, suggestive of an astigmatic image that is not quite in focus. In this connection it is important to note that the position angle of the images (Figure 5-3) is limited to a fairly narrow range around about 65 degrees, independent of field position. This is at odds with the expectation of the astigmatic behavior caused by misaligned optics. In that case the position angle should rotate by about 90 degrees from upper left to lower left, and likewise from upper right to lower right (see left panel in Figure 5-2). The observed behavior is consistent with field-independent astigmatism (see right panel in Figure 5-2).

Table 5-4: IRAF Results From In-Focus HIPO Images

OS	Corner	FWHM	ellip (obs)	PA (obs)
55	LL	13.17	0.011	25.5
57	LL	11.75	0.025	60.3
59	LL	11.19	0.054	58.5
64	LR	9.63	0.075	71.0
67	LR	7.46	0.125	81.3
69	LR	10.66	0.016	48.7
71	LR	12.92	0.048	71.5
63	UL	9.18	0.094	76.4
65	UL	9.59	0.108	49.5
66	UL	9.30	0.064	68.5
68	UL	11.61	0.134	62.9
70	UL	9.81	0.023	78.1
72	UL	11.70	0.014	153.9
54	UR	10.32	0.172	60.0
56	UR	10.76	0.045	61.0
58	UR	12.39	0.024	49.0
60	UR	8.96	0.025	94.2
55	Middle	12.64	0.016	62
57	Middle	11.43	0	
59	Middle	11.42	0.054	57.3

Average	LL	12.04	0.030	48.1
Sigma		1.02	0.022	19.6
Average	LR	10.17	0.066	68.1
Sigma		2.27	0.046	13.8
Average	UL	10.20	0.073	67.1
Sigma		1.15	0.048	11.6
Average	UR	10.61	0.067	66.1
Sigma		1.41	0.071	19.5
Average	Middle	11.83	0.023	59.7
Sigma		0.70	0.028	3.3

* OS72 removed from average & sigma

The next question is whether we can see the field-dependent astigmatism due to misalignment of the secondary in the presence of the seeing we experienced during our observations. This question was addressed by comparing actual observed images with images modeled using ZEMAX. The modeled images were convolutions of uniformly illuminated circular regions with diameters varying through the range of FWHM seen in Table 5-4 with the PSFs seen in the left hand panel of Figure 5-2 using the ZEMAX Geometric Image Analysis function. Figure 5-4 shows the star image in OS64 (which has an mid-range ellipticity of 0.075 and FWHM of 9.6 pixels) flanked by ZEMAX simulated images produced by convolving the PSF for the upper left field of the left panel in Figure 5-2 with circles 7.5 (upper left), 13 (upper right), and 9 (lower left) pixel diameters. The elongation of the images due to field-dependent astigmatism is clearly sufficient to see in the HIPO images. It is also clear that the observed images are not as elongated as we would expect them to be if misalignment was the cause of the astigmatism.

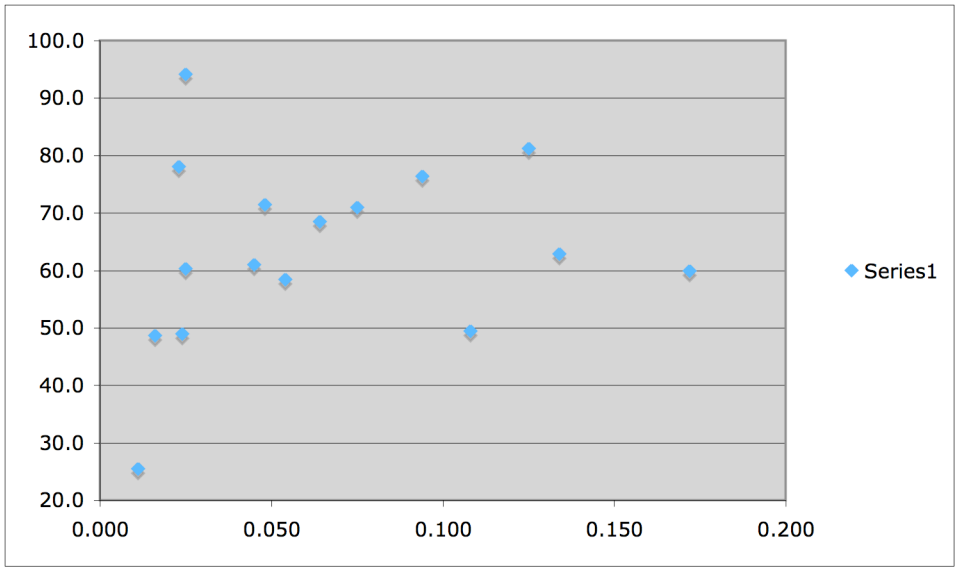

Figure 5-3: Position angles of the HIPO images (vertical) plotted against ellipticity (horizontal). The position angle is necessarily ill-defined when the images are nearly round, but for even very modest values of ellipticity the position angle is limited to a relatively narrow range around 65 degrees. This is independent of position in the field.

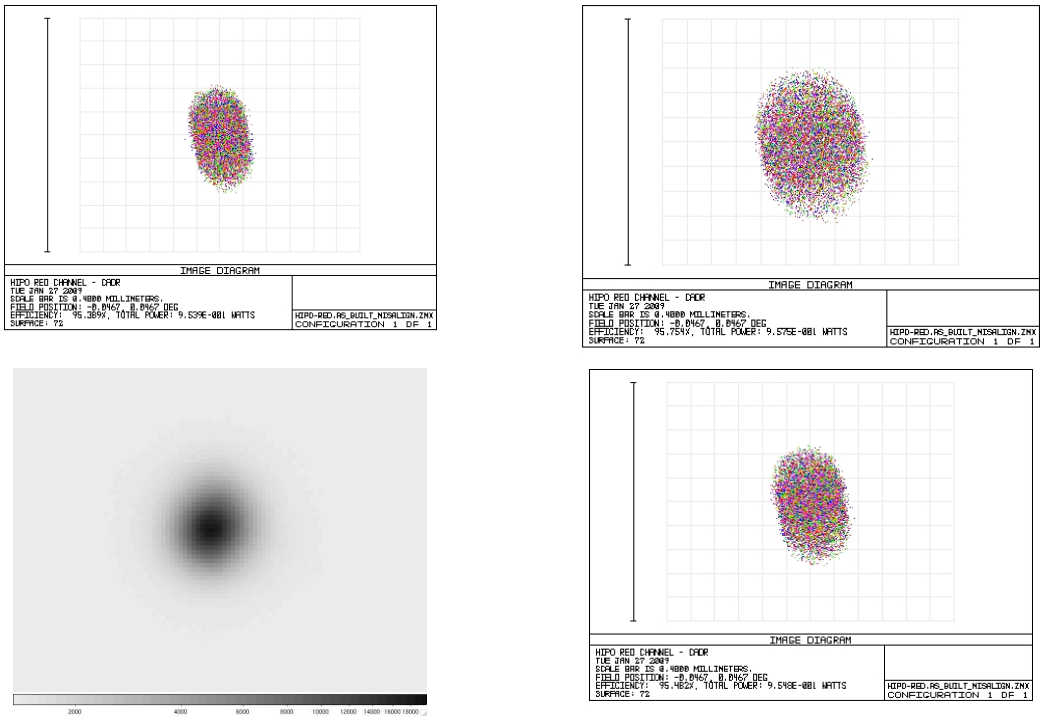

Figure 5-4: Expected image elongation for field-dependent astigmatism compared to an observed image. The star image from OS64 (lower left, ellipticity=0.074, FWHM=9.6 pixels) is not as elongated as the simulated images. The simulated images in the top row show the range of image elongation expected while the simulated image to the right of the OS64 image is directly comparable to it. See text for further discussion.

We conclude that:

1. The ~0.7 wave astigmatism seen in the Shack-Hartmann analysis is real.
2. The astigmatism is field-independent, not the field-dependent astigmatism that would result from compensation of a large tilt error with a large decenter because:
    a. The required tilt/decenter is far too large given the theodolite and autocollimator alignment done prior to the HIPO work
    b. The expected elongation of the in-focus images is large enough to see, but it is not seen
    c. The orientation of the images does not vary with field position
    d. The elongation and fixed orientation of the images is consistent with field-independent astigmatism and a slightly out-of-focus image.
3. The field-independent astigmatism is produced by an astigmatic optic, most likely one that is slightly stressed by its mounting hardware. M3 is the obvious first candidate to check.
4. The impact of the field-independent astigmatism is sufficiently small that no additional work is required for early science.

Intrinsic Optical Quality of the TA:

In principle the Shack-Hartmann results give a direct measurement of the quality of the optics of the telescope once it is properly aligned. In practice this is complicated by the field-independent astigmatism observed in the system. We made an attempt to remove the effects of defocus and astigmatism by removing those terms from the Zernike fit to the observed Shack-Hartmann data.

From the Shack-Hartmann point of view the intrinsic optical quality is a combination of errors that are not modeled by the 11-term Zernike least-squares fit and the Zernike terms for coma, trefoil, and spherical aberration. We intentionally removed focus and astigmatism for the purpose of determining the intrinsic quality, and the tip/tilt terms only affect the location of the image, not its quality.

Table 5-5 gives the FWHM of the fit residuals, the FWHM of the image formed from the coma, trefoil, and spherical aberration Zernikes (Z7-11), and the vector sum of these, which we take to be the FWHM of the image formed by the intrinsic optics.

Table 5-5: Intrinsic SOFIA TA Optical Quality

OS	FWHM of fit residuals (arcsec)	FWHM of Z7-Z11 terms (arcsec)	Vector sum (arcsec)
125	0.29	0.14	0.32
126	0.32	0.18	0.37
		Average	0.34

It should be borne in mind that the lenslet array used for these tests is quite coarse so image defects due to the known high spatial frequency errors on the secondary mirror, for example, are filtered. For formal V&V purposes and finer lenslet array should be used. With this caveat, and the astigmatism removed, the intrinsic quality of the TA optics as assembled into the telescope appears to be excellent.

Conclusions:

1. The TA is aligned sufficiently well for Early Science. No additional work is required. If the alignment is changed the gyro alignment will be affected and may need to be redone.
2. There is approximately 0.7 waves of astigmatism in the integrated TA optical system. This is not primarily due to tilt/decenter compensation of the secondary and is likely due to an optic stressed by its mount.
3. The intrinsic quality of the TA optics is excellent, on the order of 1/3" FWHM. A formal assessment of this would best be done after fixing the astigmatism and with a finer Shack-Hartmann lenslet module.

Next Steps:

1. No action is needed for Early Science
2. Check for sources of astigmatism in the TA optics
3. Realign to do a better job of optimizing the tilt/decenter once the astigmatism is corrected
4. Revisit the intrinsic optical quality of the TA using a finer Shack-Hartmann lenslet array.

TC-HIPO-06: Gyro Alignment

Introduction:

This test determines the alignment of the gyro reference frame (GYRF) and the telescope assembly reference frame (TARF). TARF is hereby defined by HIPO and has previously been mapped to the HIPO CCD coordinate system (TC-HIPO-01). The alignment measurements are performed by commanding motions about the TARF axes, while observing the motions of a bright star in the HIPO images. At initial setup of the TA, TARF is assumed to be conjugate with the gyroscope axes defining GYRF by their sensing axes. As the gyroscopes serve as feedback sensors in the telescope attitude control loop, the in TARF commanded rotations lead to a rotation about the gyroscope axes. Comparing centroid measurements and recorded gyroscope attitude data during these processes permits the rotational alignment relationship between TARF and GYRF to be quantified. Background information on the algorithms can be found in [1]. The GYRF axes are assumed to be orthogonal to each other, because the gyroscope box in which the gyroscope are mounted was measured to have non-orthogonality errors in the region of only 20-40 arcsec.

With the intention to automate the alignment procedure, analysis software was prepared to evaluate HIPO images and to calculate the according alignment matrices on-site. It was decided that the best approach for the automation was a maneuver scheme with a fixed number of rotations with a constant rotation angle. The LOS alignment was particularly difficult in regard to avoid the telescope motion limits during the maneuver sequence. At begin of the sequence, the telescope was positioned at the positive LOS motion limit and the first alignment maneuver started with a negative rotation. After allowing time for the FD to settle and taking 5 images with HIPO, the next maneuver, a positive LOS rotation was performed. About 6 maneuvers were possible before hitting the negative LOS motion limit as the telescope rotates towards the negative LOS motion limit due to Earth rotation.

The execution of this test was made much more efficient by changing filters and increasing the proportional gain of the fine drive control system that resulted in much more rapid settling of the fine drive. The procedure was further streamlined by taking 5-frame basic occultation images with HIPO rather than several single frames.

Data Acquired:

The test sequence started with LOS alignment maneuvers. After the optimal number of maneuvers and rotation angle were determined on UT20081211, five sets of alignment measurements were performed. The first set was performed with the alignment matrix from the TA Line Ops prior to this test campaign. Each of the following alignment measurements were performed with an updated alignment matrix. During the on-site analysis, it appeared that changes in the gyro drift were significantly affecting the alignment measurements leading to multiple maneuver repetitions. Table 6-1 summarizes the alignment maneuvers that were performed during the HIPO Line Ops. The calculated and implemented alignment matrices during the test are listed at the end of this section.

Table 6-1. Summary of the performed alignment measurements with according UT times, HIPO image sequence numbers (HIPO OS), alignment axis, rotation angle about this axis, number of performed rotations and the implemented alignment matrix during the run.

Date UT	UT End	HIPO OS	Axis	Angle [°]	No. of moves	Implemented matrix during run
20081212	05:30-05:33	24-31	LOS	4	6	align #1 (TA Line Ops)
20081212	06:39-06:43	34-40	LOS	4	6	align #3
20081212	07:28-07:31	45-51	LOS	4	6	align #4
20081212	07:38-07:41	54-60	EL	0.1	6	align #4
20081212	07:47-07:49	66-72	XEL	0.1	6	align #4
20081213	04:06-04:10	64-72	EL	0.1	8	align #5
20081213	04:12-04:15	75-83	XEL	0.1	8	align #5
20081213	07:54-07:59	180-192	LOS	3.5	12	align #5
20081214	08:12-08:17	76-86	LOS	3.5	10	align #6
20081214	08:21-08:25	88-98	EL	0.1	10	align #6
20081214	08:27-08:30	100-110	XEL	0.1	10	align #6

Data Analysis:

The LOS alignment data analysis is shown exemplarily for LOS alignment run OS24-31. The alignment measurements were disturbed by an apparent drift variation in the HIPO centroid data. The drift was estimated during on-site analysis with the HIPO centroids. It appeared that the drift at one LOS motion limit was different to the drift at the other LOS motion limit.

The TA attitude data shows that the drift was partly caused by the control deviation which converges over time slowly to zero after the large LOS rotations. The control deviation is the difference between the actual attitude and the commanded attitude of the telescope and is calculated by quaternion multiplication:

$$q_{CD} = -q_{\text{actual attitude}} * q_{\text{commanded attitude}} \quad (6\text{-}1)$$

Figure 6-1 shows the control deviation for the EL and XEL axes along with the HIPO X pixel values from the images that were taken during the alignment run. Any deviation from zero of these curves causes a pointing error. Five HIPO images were taken at each alignment position. The LOS rotations about 4° were performed in between these measurements.

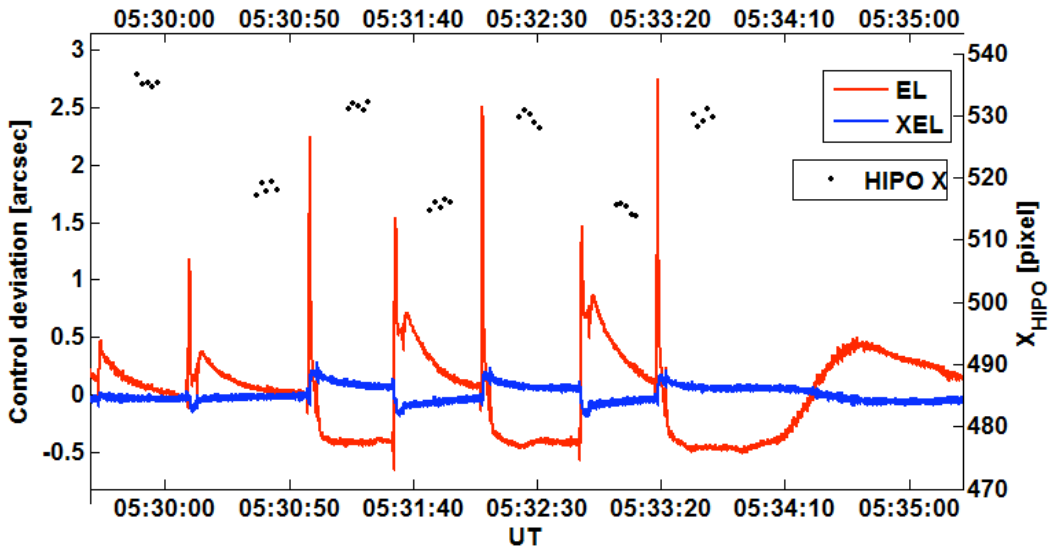

Figure 6-1. Control deviation in EL and XEL during the LOS alignment maneuvers on the left y-axis in arcsec. The HIPO centroid positions in X are shown for each image on the right y-axis. Five HIPO images were taken at each alignment position. In total, six LOS rotations (4°) were performed.

The control deviation can be taken into account in the alignment analysis by correcting the HIPO centroid data for the known pointing error. This requires first transforming the control deviation into HIPO pixel coordinates and then, adding it to the measured centroid positions. Using the relations in [2], the transformation of the control deviation from TARF (EL, XEL) into HIPO pixels (X, Y), is given by:

$CD_X = -(CD_{XEL} \cos(theta) + CD_{EL} \sin(theta)) / 0.327$	(6-2)
$CD_Y = -(CD_{EL} \cos(theta) - CD_{XEL} \sin(theta)) / 0.327$	(6-3)

with theta = 39.81°.

The pointing error is then added to the HIPO pixels:

$X_{corr} = X + CD_X$	(6-4)
$Y_{corr} = Y + CD_Y$	(6-5)

The control deviation was averaged over the exposure time of an image. Figure 6-2 shows the required correction for the centroids in HIPO coordinates to compensate for the control deviation. Figure 6-3 shows the acquired HIPO centroid data in X and Y coordinates during the entire LOS alignment run. The raw and the corrected data are shown for both axes. Although the pointing error seems small, the alignment results are affected greatly.

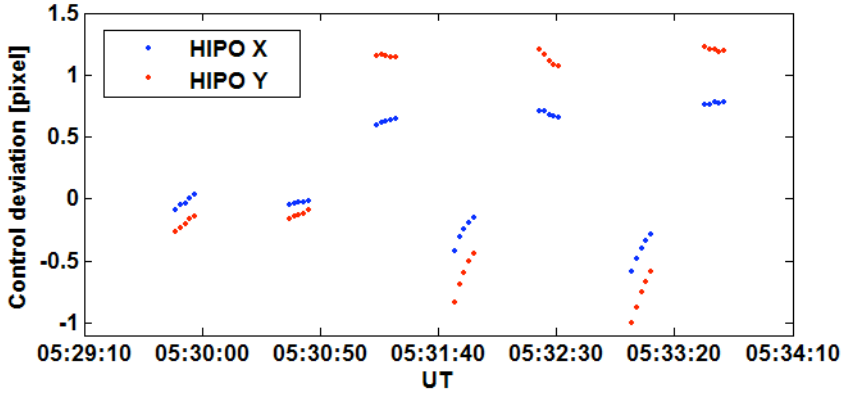

Figure 6-2. A plot of required correction for the HIPO centroids to compensate for the existing control deviation during the alignment measurement.

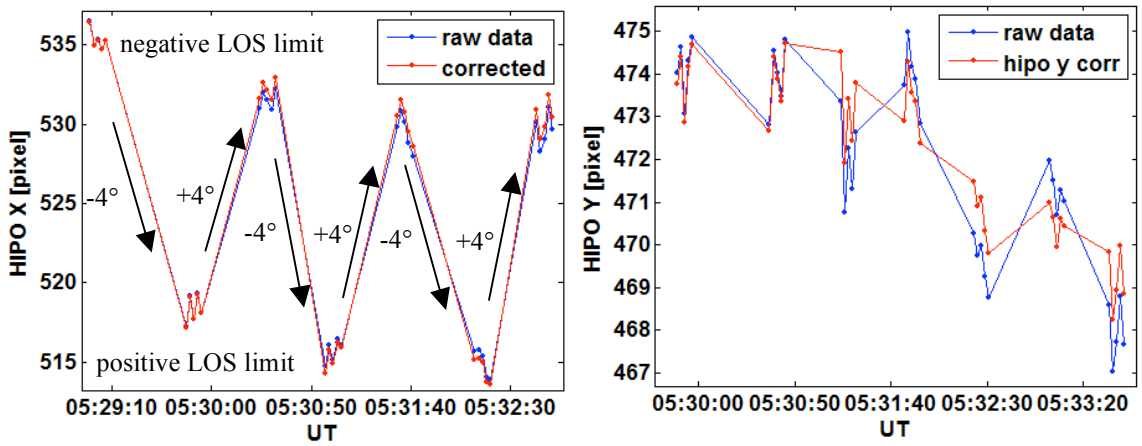

Figure 6-3. HIPO centroid data in X and Y coordinates before and after the six alignment measurements which are indicated by arrows. The raw data are shown in red, the data that is corrected for the control deviation is in blue.

As a final processing step, the residual drift in the data is corrected. The drift information is taken from HIPO centroids. In contrast to the on-site analysis, only one drift values per axis is determined. The drift value for each axis is estimated such that the RSS of the centroid position standard deviations at each LOS motion limit is minimized.

The drift affects the alignment analysis only within one alignment maneuver. The starting and end centroid positions are evaluated separately for each maneuver. The drift affects the measurement only between the first image of the start position and the last image of the end position per maneuver. The total amount of drift that happened between the first and the last maneuver does not affect the calculation.

In summary, the misalignments are calculated using data from four processing steps:

1. Raw centroid data
2. Apparent drift is corrected (final step for on-site analysis)
3. Existing control deviation added to raw data
4. Existing control deviation added to raw data and residual drift corrected.

Results:

In the first part, the results of the LOS alignment measurements are presented. The misalignment of the LOS axis is described by the so-called turning point which is the pixel position on the HIPO CCD about which the telescope is rotated when commanding a LOS rotation. After the alignment is complete, the turning point should corresponds to the center of the flange which is determined in HIPO-TC-01 to be the pixel location $X_0 = 542.8$, $Y_0 = 480.2$.

The resulting turning points, standard deviations and offsets to the nominal center of the flange are shown in table 6-2. Results are given for each of the above mentioned processing steps. The drift corrected data (2 values per axis) were used on-site to calculate the new LOS alignment matrices which were implemented into the system before the next alignment measurement. The control deviation and drift corrected data (1 value per axis) were calculated during post-processing. In the current understanding, these data provide the most accurate information of the turning point.

Table 6-2. Calculated turning points, their standard deviations and the difference to the center of the flange at $X_0 = 542.8$, $Y_0 = 480.2$.

HIPO Frames	Data processing status	X [pix]	Y [pix]	σ_X [pix]	σ_Y [pix]	ΔX [pix]	ΔY [pix]
OS24-31	Raw data	553.2	684.9	21.1	20.6	10.4	204.7
	Drift corrected (2 drift values per axis)	526.1	708.1	9.5	11.6	-16.7	227.9
	Raw data with control deviation added	533.4	697.0	13.5	15.7	-9.4	216.8
	Control deviation added and drift corrected (1 drift value per axis)	536.2	701.5	13.2	11.7	-6.6	221.3
OS34-40	Raw data	570.7	465.2	40.9	22.8	27.9	-15.0
	Drift corrected (2 drift values per axis)	548.3	468.9	20.2	14.4	5.5	-11.3
	Raw data with control deviation added	544.5	480.4	37.3	20.1	1.7	0.2
	Control deviation added and drift corrected (1 drift value per axis)	543.0	487.5	22.1	14.9	0.2	7.3
OS45-51	Raw data	579.3	463.3	30.6	21.6	36.5	-16.9
	Drift corrected (2 drift values per axis)	545.0	477.3	11.1	11.5	2.2	-2.9
	Raw data with control deviation added	557.1	476.6	24.7	18.3	14.3	-3.6
	Control deviation added and drift corrected (1 drift value per axis)	555.8	481.8	8.6	14.7	12.4	0.7
OS180-192	Raw data	565.3	458.6	16.8	21.5	13.0	1.6
	Drift corrected (2 drift values per axis)	565.1	457.0	16.6	21.0		
	Raw data with control deviation added	556.9	460.6	16.6	21.3	22.5	-21.6
	Control deviation added and drift corrected (1 drift value per axis)	556.2	458.9	16.6	21.2	22.3	-23.2
OS76-86	Raw data	649.5	537.6	10.2	17.3	13.4	-21.0
	Drift corrected (2 drift values per axis)	638.8	529.1	9.5	10.2		
	Raw data with control deviation added	638.4	543.4	10.8	15.9	106.7	57.4
	Control deviation added and drift corrected (1 drift value per axis)	641.8	542.1	10.0	10.7	96.0	48.9

The three corrected data sets yield similar results and their standard deviations are smaller than those of the raw data set. The difference between the measured turning point and its desired position at the flange center is already small after the first alignment iteration. It even becomes smaller for the drift corrected data (2 values) within the first three alignment measurements (as this data is used to calculate the alignment matrix). The forth iteration step does not result in an alignment improvement, but the test procedure changed and its results are still within the error of the procedure. However, the last measurement provides contradictory results: although the alignment correction that was added to the already implemented matrix is very small, the final turning points were measured to be about 38 arcsec (RSS) off the flange center. No explanation was found that could cause this discrepancy.

Assuming a centroid measurement error of one pixel, the alignment error of the procedure for the first three measurements (4° rotations) is about 6.6 arcsec (~20 HIPO pixels). Repeating the maneuver six times should reduce this number to 2.7 arcsec (~8 HIPO pixels). The later two alignment measurements were performed with 12 (respectively 10) maneuvers and 3.5° rotations. The error of the procedure is about 7.6 arcsec and is reduced through repetition to about 2.4 arcsec.

The data analysis in TC-HIPO-10 shows that flexures cause pointing errors over the 4° LOS rotation range of about 0.6 arcsec (1.5 pixels). Within this analysis, the pointing errors due to flexure are interpreted as misalignments. In worst case, 1.5 pixels are interpreted as misalignments as large as 10 arcsec, respectively 30 pixels.

An estimate of the initial misalignment of the LOS gyro is obtained by combining the implemented misalignment corrections with the residual misalignment measurements from table 6-2 (here in pixel). All three components for the five alignment measurements are presented in table 6-3. The upper part of the table provides the misalignment information in turning point locations on the HIPO CCD. The lower part of the table provides the same misalignment information in EL and XEL in arcsec. Comparing the estimated misalignments in the right column provides a consistency check of the entire measurement series. Except for the last measurement, the results suggest in average an initial misalignment of about 69.4 arcsec in EL and -183.1 arcsec in XEL which need to be compensated to make the gyro LOS axis conjugate with the TARF LOS axis.

Table 6-3. Comparing the estimated gyro LOS misalignment (compensated, residual and estimated) for the five measurements. Upper part: turning point locations on the HIPO CCD. Lower part: misalignment with respect to the flange center in EL and XEL.

	Compensated misalignment (turning points) by implemented matrix		Measured difference between turning point and flange center		Estimated misalignment (compensated+measured)	
Implemented matrix	X [pix]	Y [pix]	ΔX [pix]	ΔY [pix]	X [pix]	Y [pix]
align #1	841.4	-258.5	-6.6	221.3	834.8	-37.2
align #3	824.5	-30.4	0.2	7.3	824.7	-23.1
align #4	829.8	-41.5	13.0	1.6	842.8	-39.9
align #5	831.8	-44.2	13.4	-21.0	845.2	-65.2
align #6	854.2	-67.2	99.0	61.9	953.2	-5.4
	Compensated misalignment by implemented matrix		**Measured difference between to flange center**		**Estimated misalignment (compensated+measured)**	
Implemented matrix	**ΔEL [arcsec]**	**ΔXEL [arcsec]**	**ΔEL [arcsec]**	**ΔXEL [arcsec]**	**ΔEL [arcsec]**	**ΔXEL [arcsec]**
align #1	123.0	-229.6	-54.2	48.0	68.8	-181.7
align #3	69.3	-177.7	-1.9	1.5	67.4	-176.2
align #4	71.0	-181.3	-3.1	-2.9	67.9	-184.3
align #5	71.2	-182.4	2.5	-7.8	73.7	-190.2
align #6	72.3	-192.8	-36.3	-11.9	36.0	-204.8

In the next part, the results of the EL/XEL alignment measurements are presented. Three alignment runs for each axis were evaluated. The data on UT20081212 seem to show inconsistent results and are omitted in the following presentation. Table 6-4 shows the detailed results for the misalignment angles measured with HIPO and with the FPI. Table 6-5 shows the averaged results of the EL and XEL axis. The results are again presented in four variations depending on the data processing step. The data on UT20081213 was taken before any EL/XEL alignment was implemented. The standard deviations are large but can be reduce through drift removal. If single drift values for each axis are used, the misalignment angle does not change greatly. The FPI misalignment angles are very consistent for EL and XEL. Unfortunately, for the EL maneuvers, we lost the AOI in the FPI after four moves, so less data is available.

The data on UT20081214 was taken after an EL/XEL alignment of 5.3 arcmin was implemented. This number resulted from the average of the drift corrected (2 drift values per axis) angles of the EL and XEL measurements on UT20081213. The results are very consistent for EL and XEL in HIPO and the FPI.

Table 6-4. Misalignment angle results for EL/XEL measurements in HIPO and the FPI.

Date UT	Frames	Axis	Data processing status	HIPO Angle [arcmin]	HIPO σ	FPI Angle [arcmin]	FPI σ
20081213	OS64-72	EL	Raw data	8.1	10.6	-24.0*	15.2
			Drift corrected (2 drift values per axis)	4.4	2.5		
			Raw data, control deviation added	7.9	10.5	-24.0*	15.3
			Control deviation added and drift corrected (1 drift value per axis)	9.0	2.7	-23.2*	1.9
20081213	OS75-83	XEL	Raw data	6.2	3.2	-22.8	2.4
			Drift corrected (2 drift values per axis)	6.0	3.2		
			Raw data, control deviation added	6.3	3.4	-23.2	2.6
			Control deviation added and drift corrected (1 drift value per axis)	6.1	3.8	-23.2	2.5
20081214	OS88-98	EL	Raw data	3.2	3.7	-28.4	3.8
			Drift corrected (2 drift values per axis)	-0.4	2.9		
			Raw data, control deviation added	3.0	3.6	-28.5	3.8
			Control deviation added and drift corrected (1 drift value per axis)	3.0	3.3	-28.5	3.4
20081214	OS100	XEL	Raw data	4.0	2.2	-27.1	2.6
			Drift corrected (2 drift values per axis)	6.5	1.7		
			Raw data, control deviation added	2.7	2.2	-28.2	2.6
			Control deviation added and drift corrected (1 drift value per axis)	2.5	3.1	-28.2	2.5

* only four moves

Table 6-5 summarizes the results of the alignment measurements by comparing the averaged results of the EL and XEL axes before and after the alignment correction. It the following conclusions, it is assumed that the data that are corrected for the control deviation and drift (1 drift value) are the most realistic results. Before the EL/XEL correction was done, the misalignment angle between the gyro axes and the TARF axes (as defined by HIPO) was measured to be 7.6 arcmin. After the correction was implemented, the misalignment was 2.7 arcmin. The misalignment angle between the gyro axes and the FPI reference frame was measured to be -21.3 arcmin. After the correction was implemented, the misalignment was -28.4 arcmin. The difference between these values of 4.8 arcmin is very close to the implemented correction of 5.3 arcmin and is within the error of the procedure.

Table 6-5. Average of misalignment angles from EL and XEL measurements before (UT20081213) and after (UT20081214) the EL/XEL axes were aligned. Implemented alignment: 5.3 arcmin.

Data processing status	20081213 [arcmin]	20081214 [arcmin]	Delta [arcmin]
HIPO			
Raw data	7.2	3.6	3.5
Drift corrected using HIPO data (2 drift values per axis)	5.2	3.1	2.1
Raw data with control deviation added	7.1	2.9	4.2
Control deviation added and drift corrected (1 drift value per axis)	7.6	2.7	4.8
FPI			
Raw data	-23.4	-27.7	4.3
Raw data with control deviation added	-23.6	-28.4	4.8
Control deviation added and drift corrected (1 drift value per axis)	-23.2	-28.4	5.1

Data from drift measurements in TC-HIPO-04 were used to determine the TA flange center in the three imagers. Centroid data was gathered in all three imagers and HIPO during two minutes of the tracking run UT20081212 OS20. The TA flange center location in the imager reference frames was derived from the averaged centroid data (Table 6-6).

Table 6-6. TA flange center in HIPO (measured in TC-HIPO-01) and in the three TA imagers.

	X / Row [pix]	Y/ Column [pix]
HIPO (TC-HIPO-01)	542.8	480.2
FPI	540.6	522.3
FFI	487.2	490.8
WFI	491.7	500.4

The EL/XEL alignment measurements were not performed for the head ring imagers during the HIPO Line Ops. These were performed during the standalone TA Line Ops on UT20081116. Note that the FCM of the secondary mirror mechanism was not at his final position and gyro alignment was only performed with respect to the center of the FPI CCD. The results are shown in Table 6-7. Despite the preliminary status of the optical alignment, the average EL/XEL misalignment angle of the FPI is equal to the misalignment angle measured during the HIPO Line Ops (Table 6-4). The measured EL and XEL misalignment angles for the FFI and WFI are very consistent.

Table 6-7. Misalignment angle of imagers measured during the TA standalone Line Ops in November 2008.

	FPI [arcmin]	FFI [arcmin]	WFI [arcmin]
EL	-24.7	-11.6	-6.4
XEL	-21.8	-11.8	-6.8
Average	-23.2	-11.7	-6.6

Conclusions:

1. The alignment of the LOS gyro axis is determined by the turning point location. Software was prepared in order to automate the procedure and complete the alignment on-site. Several iterations of the alignment procedure were performed and the misalignment stepwise improved. During the test, on-site analysis was difficult due to an apparent drift variation over the test time. It turned out that a varying control deviation within the FD control loop had influence on the measurements. The control deviation could be taken into account in the alignment analysis and data were reprocessed. The results are presented and yield an initial misalignment of the gyro LOS axis of about 69.4 arcsec in EL and -183.1 arcsec in XEL which can be compensated by the appropriate alignment matrix. The results of the last iteration step of the LOS alignment were unexpected and the misalignment became significantly different. No explanation has been found for this measurement.
2. The alignment measurements for the EL and XEL gyro axes were consistent. The initial misalignment angle of the gyro axes with respect to TARF (as defined by HIPO) was measured to be 7.6 arcmin.
3. The pixel location of the TA flange in all three imagers was provided based on measurements in tracking mode.
4. The alignment measurements for the EL and XEL gyro axes with respect to the imagers are presented. The initial misalignment angle for the FPI is -23.2 arcmin, for the FFI -11.7 arcmin and for the WFI -6.6 arcmin.

Next Steps:

1. Calculate the four new alignment matrices based on the presented results. Provide the acceleration vector that was measured during the maneuvers for FBC.
2. Implement and verify these matrices during the next Line Ops. As HIPO will be most likely not available, the FPI can be used for verification.

References:

[1] Franziska Harms et al.: On sky testing and preliminary sensor alignment for the SOFIA telescope, Astronomical Telescopes and Instrumentation, Proceedings SPIE Vol. 6267, May 2006

[2] Ted Dunham: HIPO-TA Coordinate Transformation, Rev. 1.1, 20.11.2008

Appendix: Implemented alignment matrices

The alignment matrix is composed using the listed elements by:

$$A_{TARF,GYRF} = \begin{pmatrix} UU & UV & UW \\ VU & VV & VW \\ WU & WV & WW \end{pmatrix}$$

	Element	Value	
align #1	*UU*	9.9999938E-01	from TA Line Ops
	UV	-6.3473508E-06	
	UW	1.1133707E-03	
	VU	5.6832686E-06	
	VV	9.9999982E-01	
	VW	5.9654787E-04	
	WU	-1.1134634E-03	
	WV	-5.9658406E-04	
	WW	9.9999920E-01	
align #2	*UU*	9.999996E-01	align.20081211.116-130
	UV	-6.068702E-06	(implemented UT20081211 09:30)
	UW	8.720224E-04	
	VU	5.766842E-06	
	VV	9.999999E-01	
	VW	3.462718E-04	
	WU	-8.721135E-04	
	WV	-3.463095E-04	
	WW	9.999996E-01	
align #3	*UU*	9.999997E-01	align.20081212.24-24
	UV	-6.057159E-06	(implemented UT20081212 06:35)
	UW	8.612887E-04	
	VU	5.767945E-06	
	VV	9.999999E-01	
	VW	3.359038E-04	
	WU	-8.613797E-04	
	WV	-3.359416E-04	
	WW	9.999996E-01	
align #4	*UU*	9.999997E-01	align.20081212.34-34
	UV	-6.064212E-06	(implemented UT20081212 06:58)
	UW	8.790777E-04	
	VU	5.761824E-06	
	VV	9.999999E-01	
	VW	3.440922E-04	
	WU	-8.791687E-04	
	WV	-3.441299E-04	
	WW	9.999996E-01	

align #5	*UU*	9.999997E-01	align.20081212.45-45
	UV	-6.065293E-06	(implemented UT20081213 02:48)
	UW	8.841983E-04	
	VU	5.760056E-06	
	VV	9.999999E-01	
	VW	3.453218E-04	
	WU	-8.842893E-04	
	WV	-3.453595E-04	
	WW	9.999996E-01	
align #6	*UU*	9.999985E-01	align.20081213.180-192
	UV	1.538545E-03	(implemented UT20081214 07:50)
	UW	9.348753E-04	
	VU	-1.538873E-03	
	VV	9.999987E-01	
	VW	3.505745E-04	
	WU	-9.344236E-04	
	WV	-3.520556E-04	
	WW	9.999995E-01	

TC-HIPO-07: Temperature and Elevation Effect on Focus and Alignment

Introduction:

This test obtains preliminary information regarding the rate and direction of focus shift and misalignment versus change in TA temperature and, optionally, elevation angle with the SiC secondary mirror installed. Because the temperature in flight is much lower than we encountered on the ground, and the rate of change of temperature in flight can be much higher than diurnal temperature variations, final measurements of this kind require flight test.

The 2004 Waco tests (SSMOC-TA-REP-1000-050602) showed that the thermal focus change is by far the largest effect, so measurement of elevation angle effects was considered optional. Due to schedule pressure the elevation angle portion of this test was skipped. Additional relevant data obtained during the DSI TA standalone line operations prior to the HIPO work are included in the discussion below.

As noted in the test procedure TC-HIPO-07, focus change with temperature was measured during the 2004 line operations at Waco, when the Aluminum secondary mirror was installed. For the Nov. – Dec. 2008 line operations, the SiC secondary mirror was installed. Based on the ratio of the coefficient of thermal expansions for aluminum and SiC, and the corresponding effect on the radius of curvatures of these mirrors, it was predicted that the focus – temperature dependence would change from the 2004 measured rate of 20 microns / °C to about 11 microns / °C (SSMOC-TA-REP-1000-050602). The linear units of microns refer to the secondary mirror position along the telescope optical axis, measured by a position transducer in the Focus and Centering Mechanism (FCM) subsystem of the Secondary Mirror Assembly (SMA). This is referred to as the FCM "t" coordinate. Since it is the position of the mirror relative to the SMA, this does not reflect changes in the absolute distance of the secondary mirror from the Primary Mirror (PM), that may be caused by temperature changes of components of the TA structure.

Data Acquired:

Initial focus values were obtained during the DSI TA "Standalone" tests in November, 2008. Focus settings were chosen based only on brief viewing of displayed FPI images. Usually only a few focus settings were tried, with values that were multiples of 50 or 100, to allow quick interpolation if needed. The focus settings and SMA temperatures from these occasions are listed in Table 7-1.

Table 7-1: FPI Focus and Temperatures

Date	SMA T	FCM t
Nov. 8	17 °C	347
Nov. 9	14 °C	400
Nov. 10 a.m.	7.6 °C	500
Nov. 15	14.8 °C	350

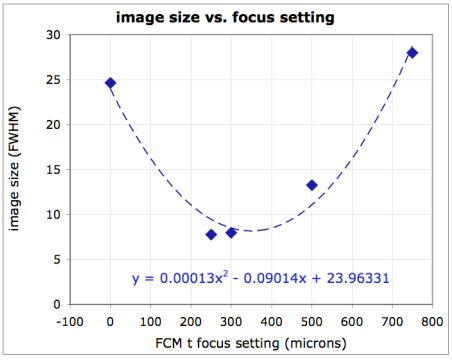

Figure 7-1: FPI focus curve, Nov. 8, 17C.

The first entry in Table 7-1 from Nov. 8 is a revised value obtained by fitting 5 FPI images taken at several focus settings as shown in Figure 7-1. A quadratic least squares fit to the measured FWHM values and focus positions of the star images was done and the optimum focus was taken to be the vertex of the fitted parabola. In the three images taken closer to best focus, the star (Polaris) was saturated, so the FWHM of a ghost image was used. This ghost image was seen whenever a very bright star was in the FPI FOV, and is probably produced by multiple reflection inside the dichroic tertiary. Although this implies the optical path length would be slightly different for the ghost image, the ghost image sizes are reasonably consistent with the two unsaturated image size values.

The primary data source was the HIPO Shack-Hartmann data obtained according to TC-HIPO-07. This provides far greater precision in evaluating defocus and other image quality factors. On each occasion, the focus (FCM t) was first set to an approximate value to produce an FPI star image that appeared to be near good focus. Then HIPO was used to obtain a Shack-Hartmann result, which includes a value for defocus in optical wavelengths. This was scaled to defocus in microns, using the previously determined scale value of 0.0375 waves/micron (SSMOC-TA-REP-1000-050602). Then the FCM was commanded to the new value of FCM t indicated by the measured defocus, and the Shack-Hartmann test was repeated to confirm that the secondary had been moved to the current best focus position. On some occasions, several Shack-Hartmann images were obtained, to check repeatability. For those the average result is used below.

Focus positions were obtained for a useful range of temperatures during the first two nights of HIPO line operations. On the first night (Dec. 10 UT), several Shack-Hartmann images and results were obtained after 4 a.m., when the indicated SMA temperature was in the range of 4.6 °C to 4.1 °C. During the next night, optimum focus settings were obtained as the SMA slowly cooled from 12 °C to 7 °C.

Data Analysis and Results:

The results are summarized in Table 7-2 and Figure 7-2 below, including deviations from a least squares linear fit. The approximate values obtained earlier using only FPI images are included in Figure 7-2 for comparison, but were not used for the linear fit. The revised FPI focus value obtained from a fitted parabola is the filled in square at 17 °C.

Table 7-2: HIPO Focus Values and SMA Temperatures

Date, ~PST	Image Number	LED Image Number	SMA Temp.	FCM t (μm)	Fitted line (μm)	O - C (μm)
Dec. 10, 6 p.m.	OS 14	OS 6	11.8 °C	437	436	1.1
Dec. 10, 9 p.m.	OS 49	OS 44	9.6 °C	471	470	0.8
Dec. 11, 3 a.m.	OS 292	OS 290	6.9 °C	510	512	-2.4
Dec. 10, 4 a.m.	OS 125	OS 116	4.3 °C	555	553	2.1
					RMS error:	1.9

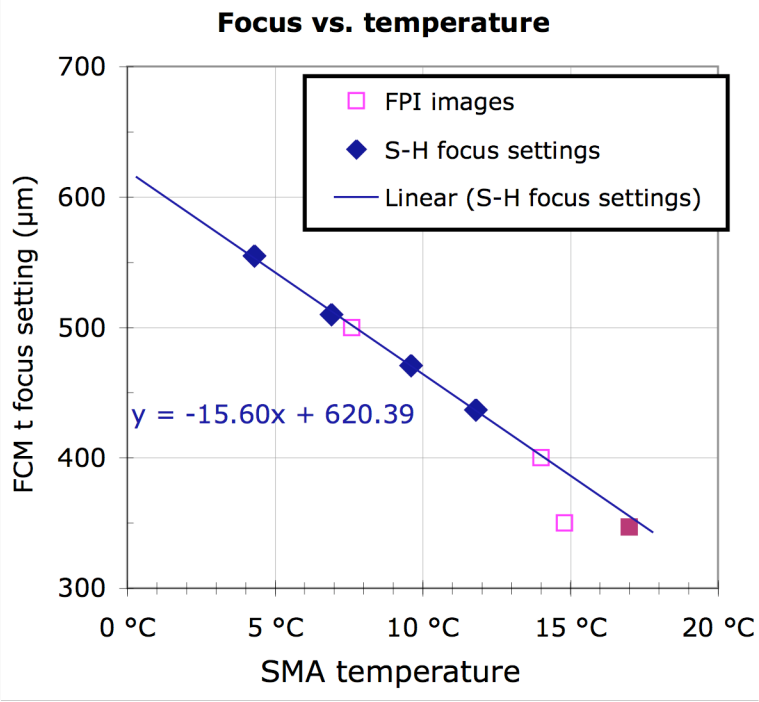

Figure 7-2: Observed focus position vs temperature relationship. The filled square at 17C is the revised FPI focus position described earlier in the text.

The HIPO data show a well-defined linear relationship of focus vs. SMA temperature, with an rms residual of less than 2 µm. The slope is -15.6 µm/C with an uncertainty of about 0.5 µm/C. The FPI results are consistent with this relationship. Note that there is no offset adjustment applied between the FPI and HIPO data since the FPI "trombone" focus was set to the previously determined position for HIPO focus.

It isn't clear why the observed slope (-15.6 µm/C) with the SiC secondary differs as much as it does from the prediction based on the 2004 Waco expectation (-11 µm/C). In any case it is well established, at least for the slow diurnal temperature changes we experienced.

There is potential for a temperature dependence to the TA alignment. This was looked for and was not found. The data presented in Table 5-3 in the TC-HIPO-05 section of this report show no significant change or trend in the coma terms as a function of temperature.

Conclusions:

The relationship between SMA focus (t) in µm and SMA temperature in degrees C (T) is:

$$t = 620 - 15.6T \qquad \text{(HIPO)}$$

for the HIPO back focal position of 319 mm from the SI mounting flange. The corresponding relationship for FORCAST (back focus = 232 mm, based on Table 9 in the FORCAST Integration and Commissioning Plan) is:

$$t = 990 - 15.6T \qquad \text{(FORCAST)}$$

The uncertainty in the slope indicates a focus uncertainty of ~20 μm when these relationships are extrapolated to -40C. This will be very close and will permit quick refinement of the actual focus position.

We now derive the general focus relationship as a function of temperature and back focus position for a given SI. Given a back-focus value Z_{SI} in mm, the total effective back-focus from PM vertex is $Z_L = Z_{SI} + 3795$ mm. The distance of the secondary mirror from the PM vertex needed to provide focus at Z_L is given by the following equation (Erickson, Matthews, NASA TM X-3137, 1975):

$$z_S = \frac{1}{2}\left\{F_p + z_L - r_s + \left[r_s^2 + \left(F_p - z_L\right)^2\right]^{1/2}\right\} \qquad (1)$$

where z_s = distance of secondary mirror vertex from primary mirror vertex
F_p = focal-length of primary mirror = 3200 mm
r_s = radius of curvature of secondary mirror = 954.13 mmm
z_L = distance of focal-plane from the primary mirror vertex (assuming no tertiary)

The corresponding focus setting would be given by:

$$\text{FCM t}_{[\mu\text{m}]} = 1000 * (z_S - 2753.3mm) - 15.6 * T_{[^\circ C]} \qquad (2)$$

Eqn. 1 is only slightly non-linear over the full design focus range. In the smaller range of back-focus values needed by the first generation instruments, Eqn. 1 can be quite well represented by a linear approximation. This combined with Eqn. 2 provides the following linear estimation of focus setting given back-focus from the SI flange Z_{SI} and SMA temperature:

$$\text{FCM t}_{[\mu\text{m}]} = 1970 - 4.23 * z_{SI} - 15.6 * T_{[^\circ C]} \qquad (3)$$

Next Steps:

1. Measure the focus position with FORCAST in flight and extend the linear relationship given by Eqn. 3 to flight temperatures.
2. Observe the focus position in flight as the telescope cools down to search for possible contributions from components with significantly different thermal time constants.

TC-HIPO-08: Pointing Stability

Preface:

This test consists of four parts, all related to the tuning and performance of the fine drive pointing control system. The first two parts require the presence of HIPO as a mass on the telescope for system tuning purposes, but it is inactive and takes no data. Therefore these tests can be done in the hangar. HIPO does acquire imaging data for the second two parts, which must be done using a star during a line operation. Part 3 of this test is complicated by the need to install a shaker in the cavity to introduce disturbances into the fine drive control system.

TA Configuration

This summary of the TA configuration reflects the state of the TA during the HIPO Line Operations from a structural dynamics point of view.

- HIPO Science Instrument installed and dewars partly filled
- All mirror covers removed (PMA, SMA, TMA)
- SiC secondary mirror installed
- SI counterweight rack installed and equipped with mass simulators
- Fine Drive balanced (weight distribution see below)
- Coarse balance weights torque with 100 ft-lb
- TA manually uncaged per SSMOC-TA-PRO-3315-050913
- One cable guide (right hand side "ear") on CLA was not installed due to ongoing maintenance
- 100 sec random noise signal available on TASCU for injection into fine drive
- The random noise was scaled so that the peak force was approximately 40% of the max. torque in each axis
- Note: the Gyro alignment matrix was changing throughout the HIPO08 tests, since its improvement was part of the HIPO line operations.

The following tables present the final result of the FD Balancing for HIPO w/o Cryogens (M_{HIPO} = 333.8kg, CG_{HIPO} [2600 15.24 -33] mm)

Coarse Weight Distribution:

Ar	5	**Al**	5	**Er**	2	**El**	3
Br	5	**Bl**	4	**Fr**	2	**Fl**	2
Cr	5	**Cl**	5	**Gr**	8	**Gl**	2
Dr	5	**Dl**	4	**Hr**	1	**Hl**	2

Fine Balancer Positions:

U	1792 mm
V	204.1 mm
W	1003.1 mm

TC-HIPO-08 Part 1: System Identification

Introduction:

This section contains the results of the first part of the HIPO08 procedure. Goal of this test was to characterize the Fine Drive control plant with the HIPO science instrument installed, and to identify changes in the dynamic behavior compared to the configuration with the Science Instrument Mass Simulator that was used during the TA standalone Line operations in November 2008. Furthermore, the sensitivity of the control plant to changes in the Coarse Drive elevation angle is discussed. This section closes with a short description of the Fine Drive controller that was implemented during the HIPO line operations, and the bandwidth measured in each axis.

Fine Drive Control Plant

The coherence of the measurements was very good. Fig. 1, 3 and 5 show the coherence functions for excitations in EL, XEL, and LOS. Values are mostly above 0.9, only at frequencies where the control plant shows a low response (zeros) the coherence goes down, since the signal-to-noise ratio deteriorates (see fig. 2,4,6: frequency response functions of the control plants). Note that excitation in EL and response in LOS show high coherence in the low frequency (rigid body) regime. This applies as well to excitation in LOS and response in EL. In contrast, XEL excitation causes very little coherence in EL and LOS. This is due to the fact that EL and LOS are significantly coupled, whereas XEL is decoupled fairly well. In fact, the principle axes coordinate system (PAIRF) is rotated by -15 deg about the TARF v-axis. This has consequences for the SISO controller design: we have to consider the coupling effects within the bandwidth of the controller, which is designed on the assumption that no coupling exists (SISO design). This is done by weighting controller outputs with decoupling terms, which are derived from the rigid body inertia matrix. In the flexible body regime coupling between all axes is generally high.

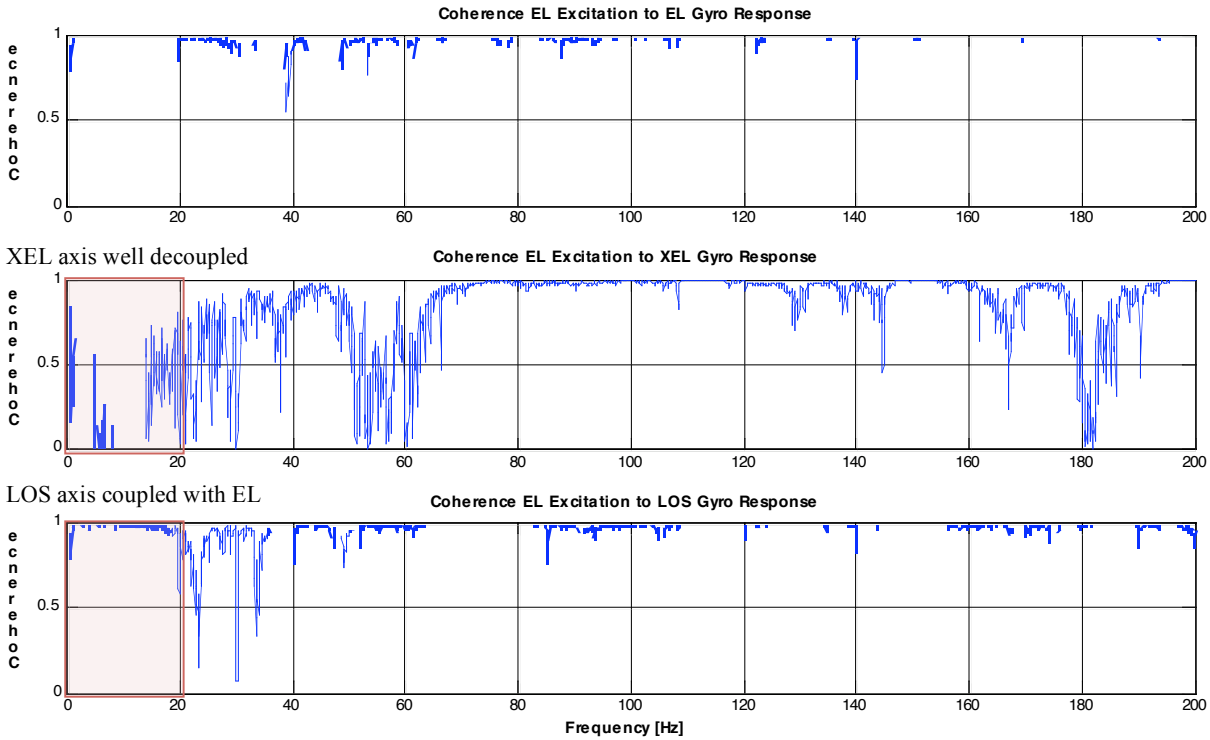
Coherence EL Excitation to EL Gyro Response
Coherence
1
0.5
0
0
20
40
60
80
100
120
140
160
180
200
XEL axis well decoupled
Coherence EL Excitation to XEL Gyro Response
LOS axis coupled with EL
Coherence EL Excitation to LOS Gyro Response
Frequency [Hz]

Figure 1

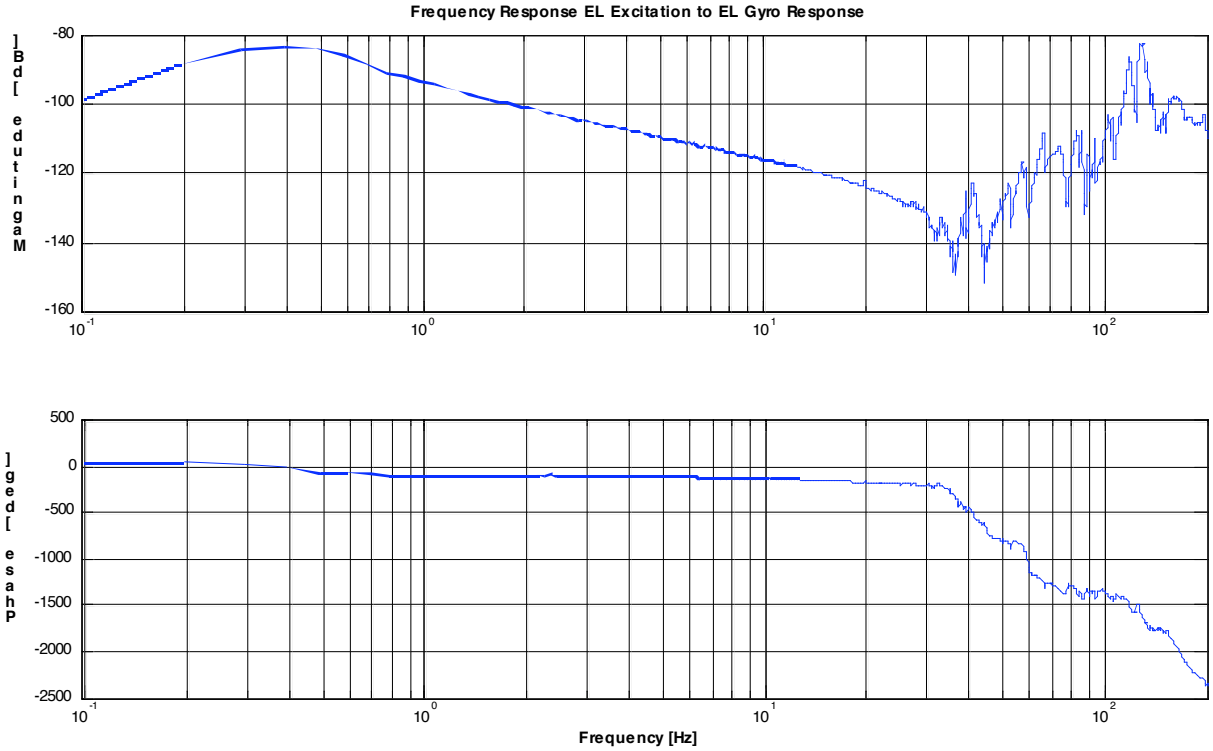

Figure 2

EL axis well decoupled from

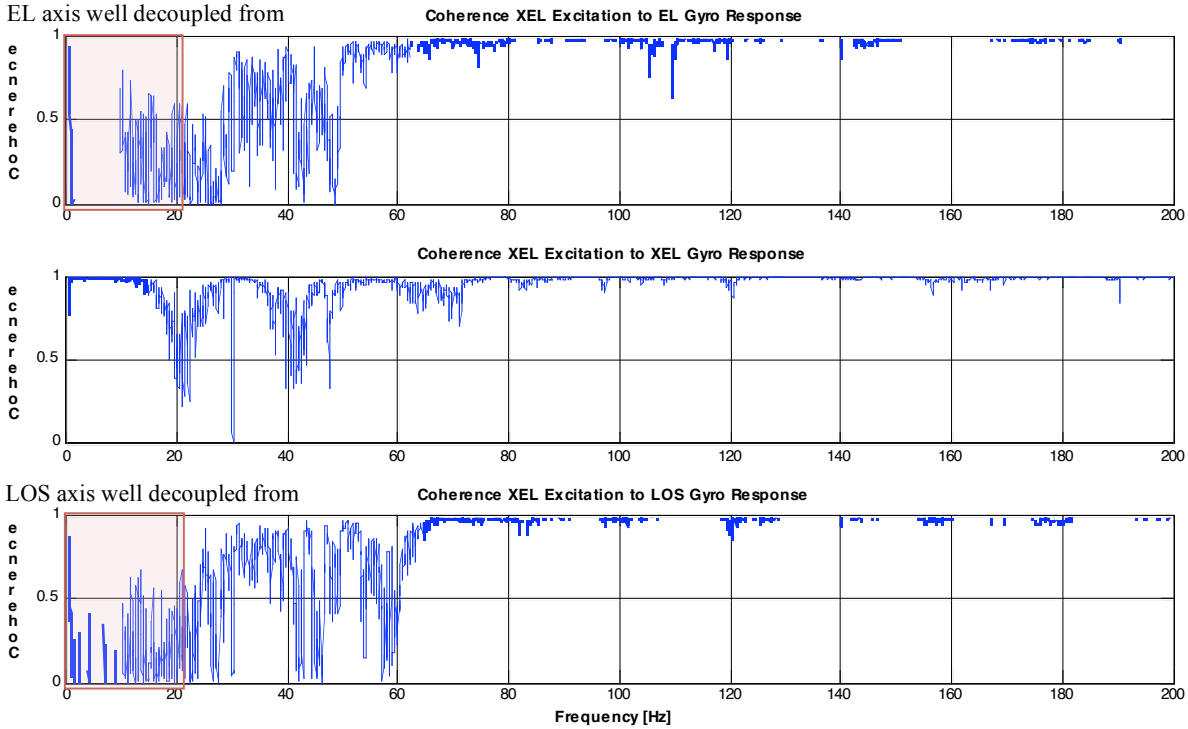

LOS axis well decoupled from

Figure 3

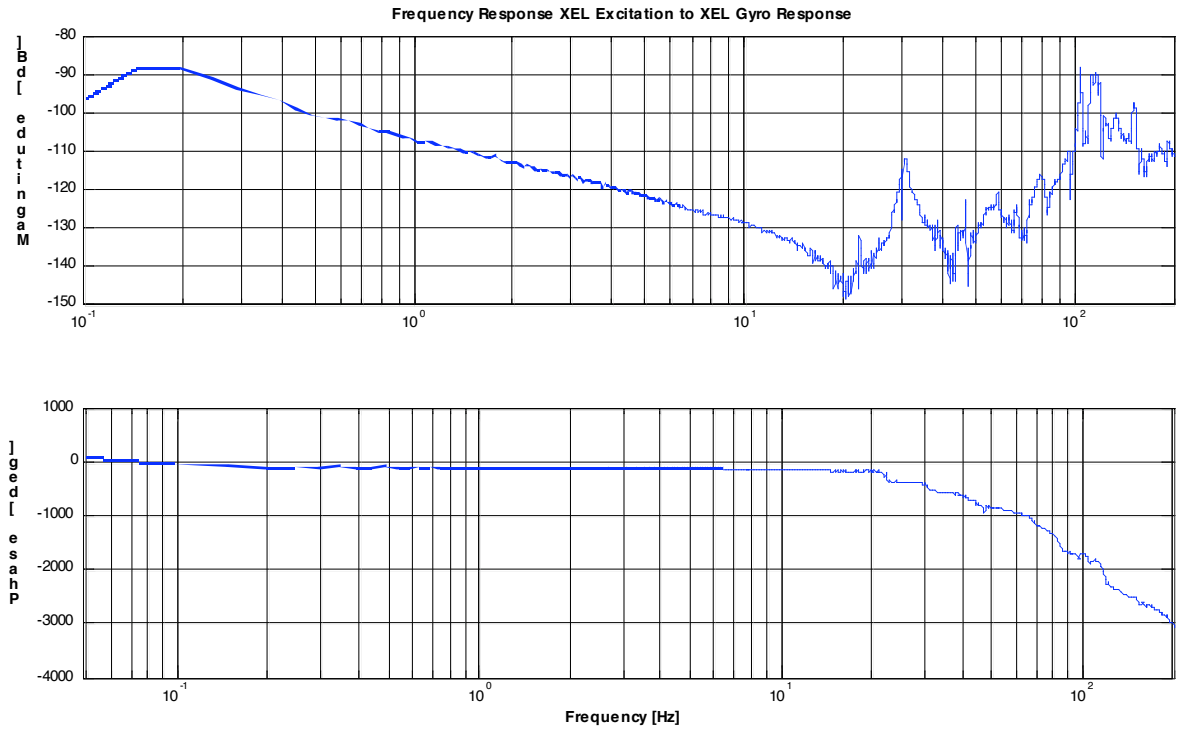

Figure 4

The frequency response functions (transfer functions) show a 20dB/dec roll off, which is typical for a plant with a single integrator. The control system was designed to be collocated in order to achieve a minimum phase system, which is suited for rigid body attitude control. However, the FD actuator does not consist of a single drive close to the Gyro box, but of eight torquers that are distributed around the bearing. Therefore, flexible modes of the TA show up in the transfer functions. And since large structures like the TA have flexible modes at fairly low frequencies, they need to be considered in the controller design. The amplitude of the transfer function increases in the flexible body regime as the continuous decoupling of the structure concentrates energy locally around the torquer motors, where the gyro box measures them.

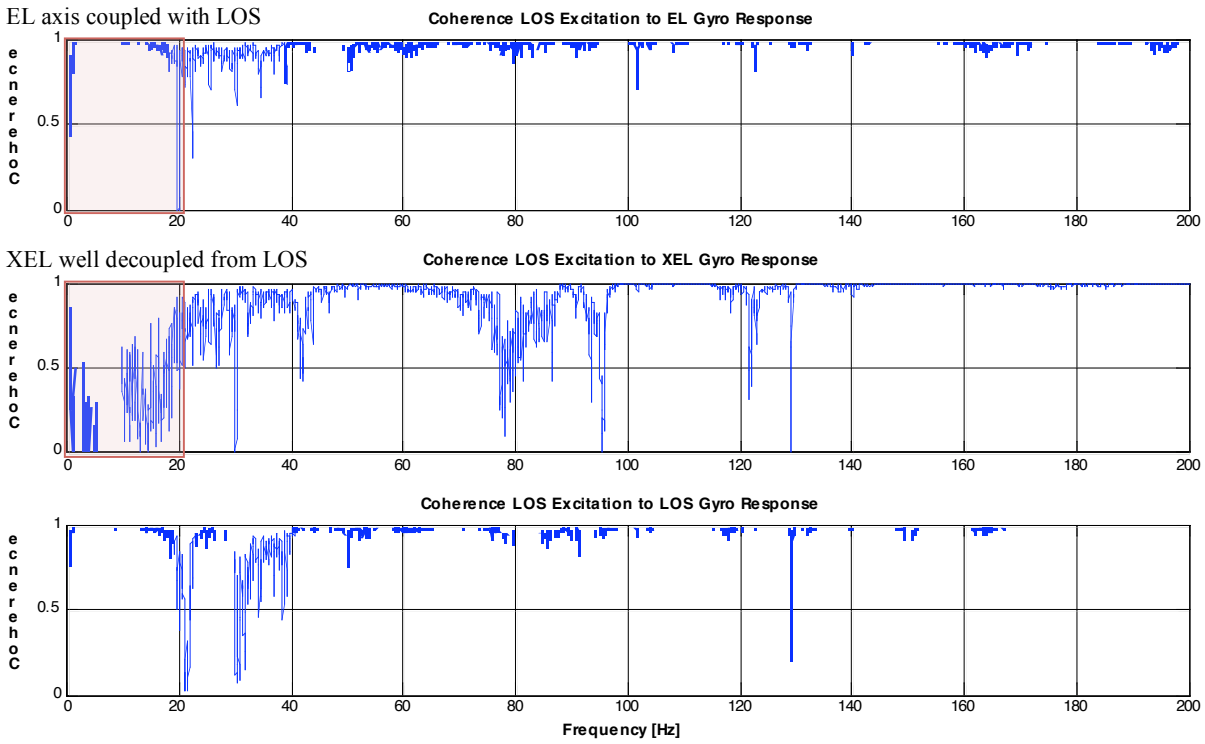

Figure 5

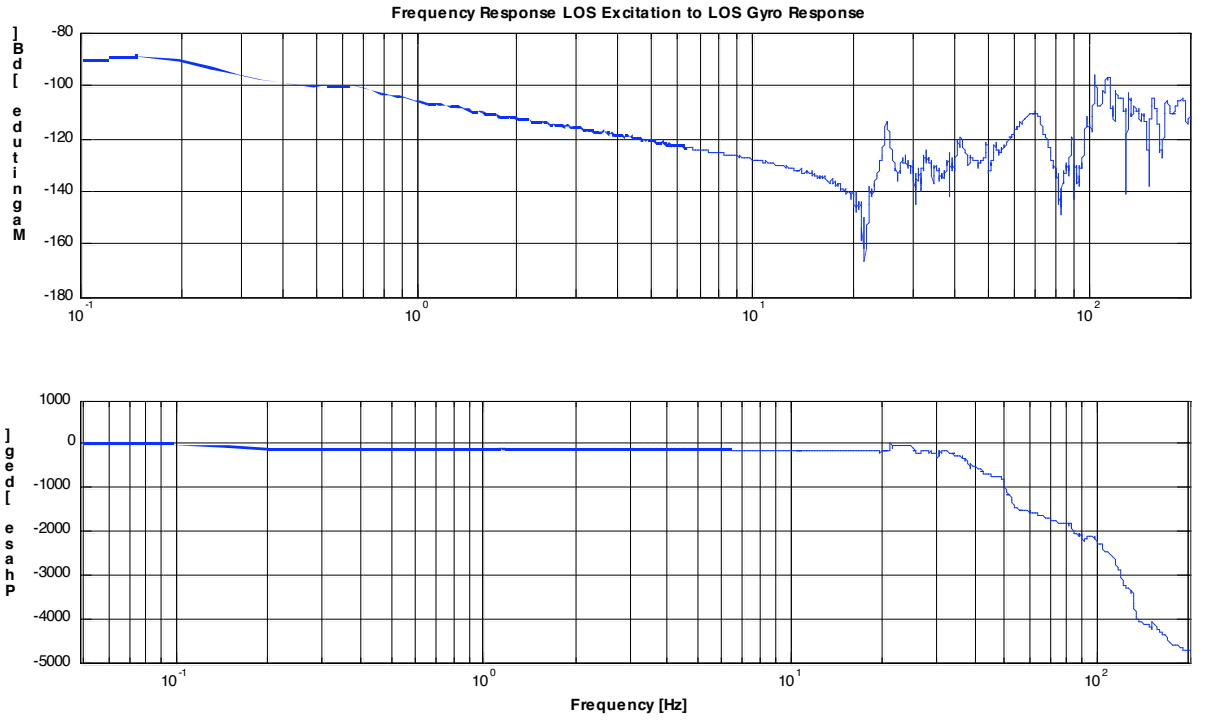

Figure 6

A stable controller will need a low pass filter in order to avoid excitation of flexible modes and to avoid high frequency noise to disturb the closed attitude control loop. In our case, to maximize our controller bandwidth, we want the low pass filter to be placed at a high frequency within the flexible regime. Therefore a number of compensators, such as notch filters and pole-zero cancellation filters need to be utilized. This is called dynamic compensation.

Sensitivity Analysis of the Fine Drive Control Plant

During the TA Modal Survey test the sensitivity of the control plant to various parameters was investigated. One result was to define the torque that is being applied to the coarse balance weight stacks. The desired value is 134 Nm (100 ft-lb), which minimizes the sensitivity of the control plant towards the coarse balance weight configuration to a level where we are not concerned at this point. One scope of the HIPO08-01 system identification measurements was to identify sensitivity to changes in the CD elevation angle, as well as to measure the sensitivity to different Science Instruments by comparing transfer functions from the TA standalone Line Ops (SI Mass Simulator installed) with data from the HIPO Line Ops.

Comparison of Elevation Angles

Figures 7 through 12 present comparisons of transfer functions taken at 17 deg (blue), 40 deg (red) and 65 deg (green) CD elevation. Figure 7 compares the transfer functions of the EL axis control plant. Figure 8 is a zoom into the most sensitive frequency range between 30 Hz and 60 Hz. Note that the data at 65 deg is very noisy.
Figure 9 compares the transfer functions of the XEL axis control plant. Figure 10 is a zoom into the most sensitive frequency range between 20 Hz and 40 Hz.
Figure 11 compares the transfer functions of the LOS axis control plant. Figure 12 is a zoom into the most sensitive frequency range between 25 Hz and 45 Hz.
All three control plants are sensitive to changes of the CD elevation angle. The most sensitive areas are the ones where the Cable Load Alleviator plays a role in the mode shape. In the worst case the changes in the transfer functions could make the dynamic compensation filters in the control loop which could ultimately lead to a destabilization of the closed loop system. However, during the HIPO Line Ops nothing was discovered that pointed in this direction, which means the changes in the modal behavior can be tolerated by the currently implemented controller (the controller is robust to those plant changes). In the future, when we try to maximize the bandwidth with more aggressive control laws we need to keep an eye on those sensitivities, since those controllers will also be more sensitive to changes in the plant dynamics.

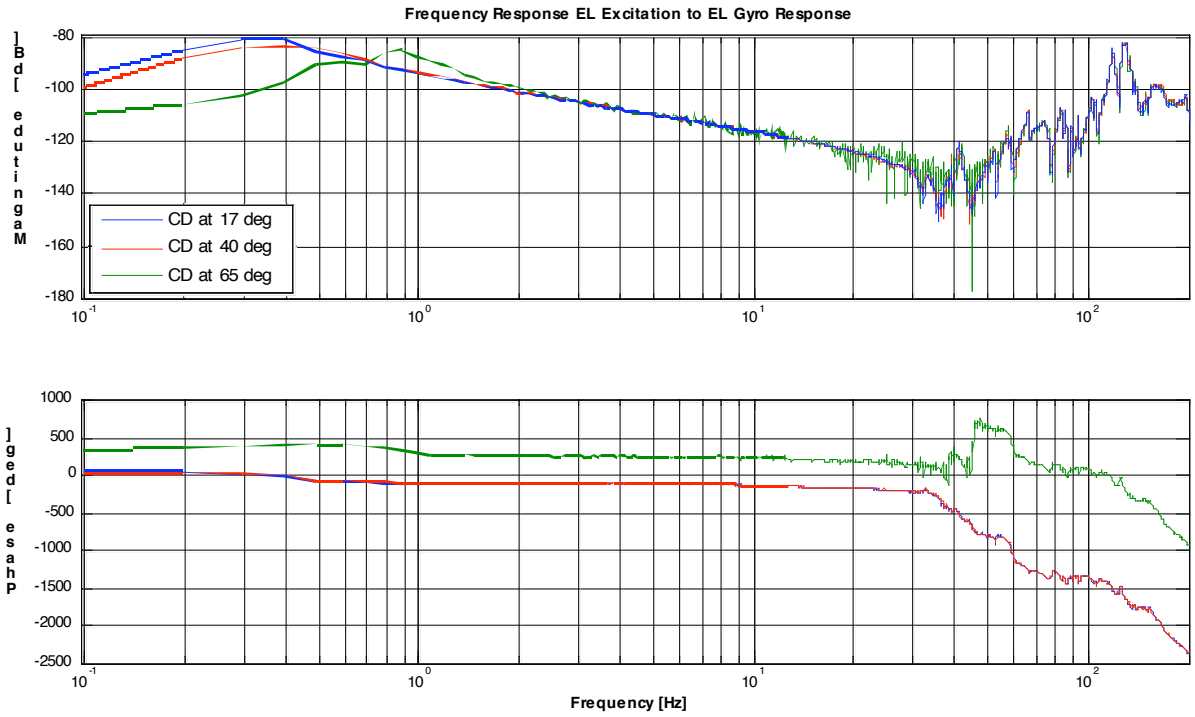

Figure 7

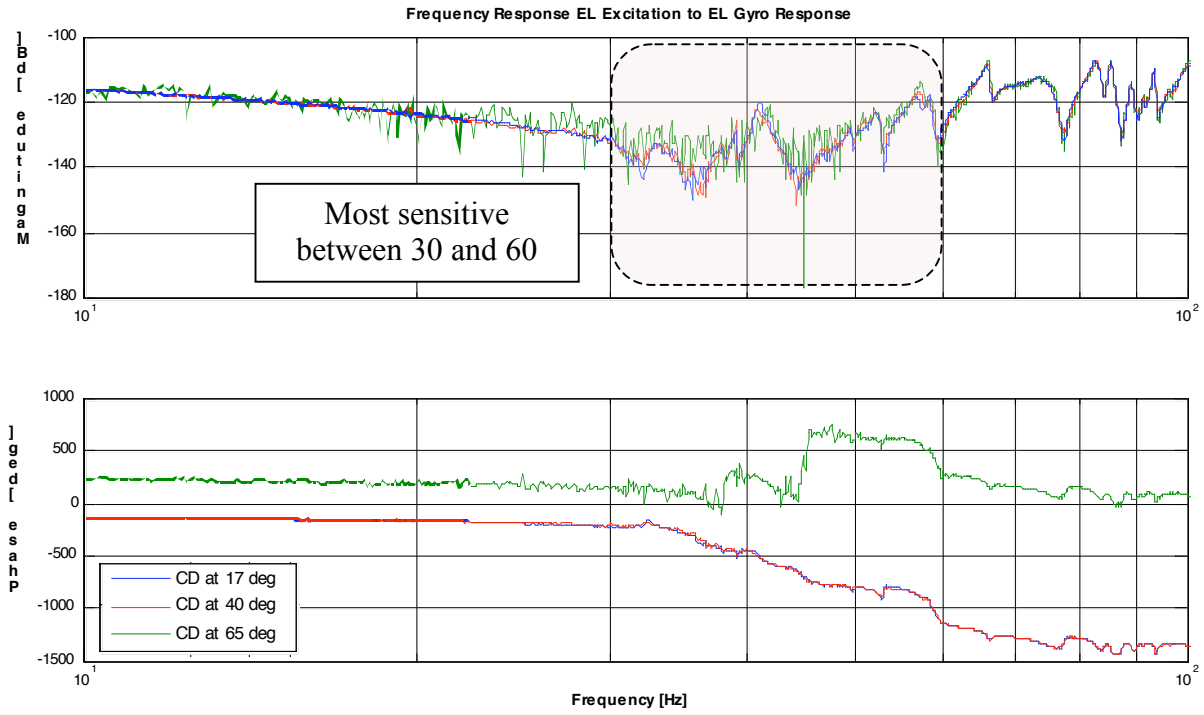

Figure 8

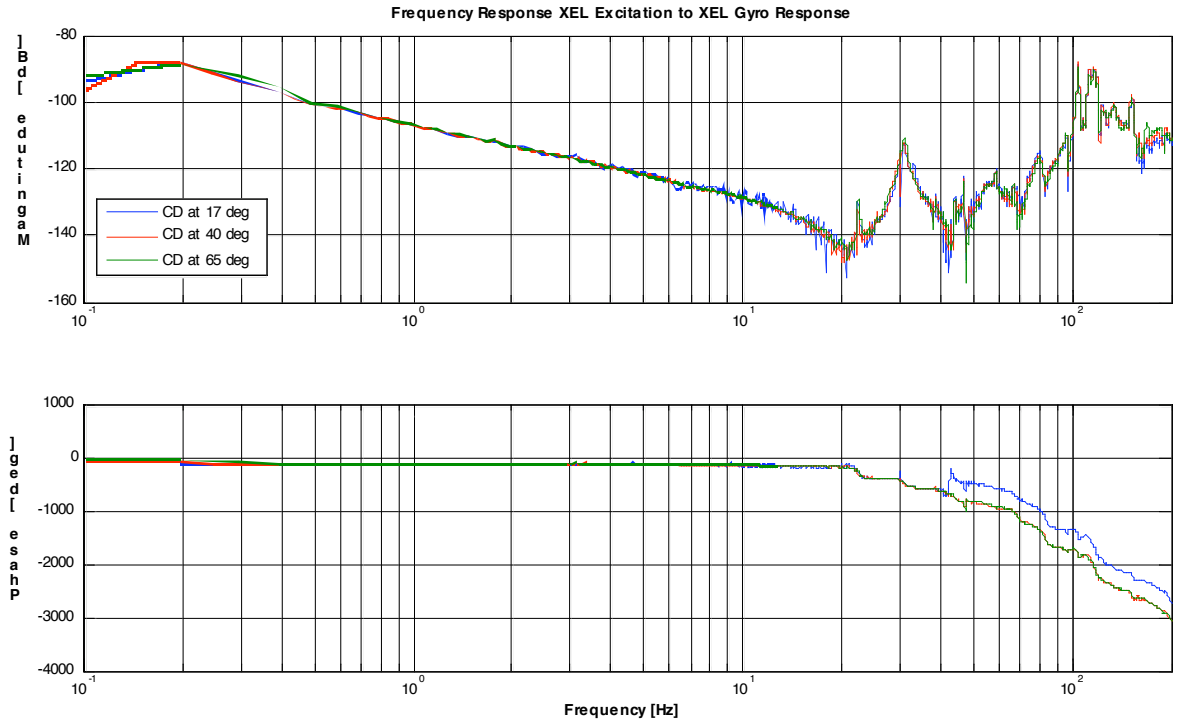

Figure 9

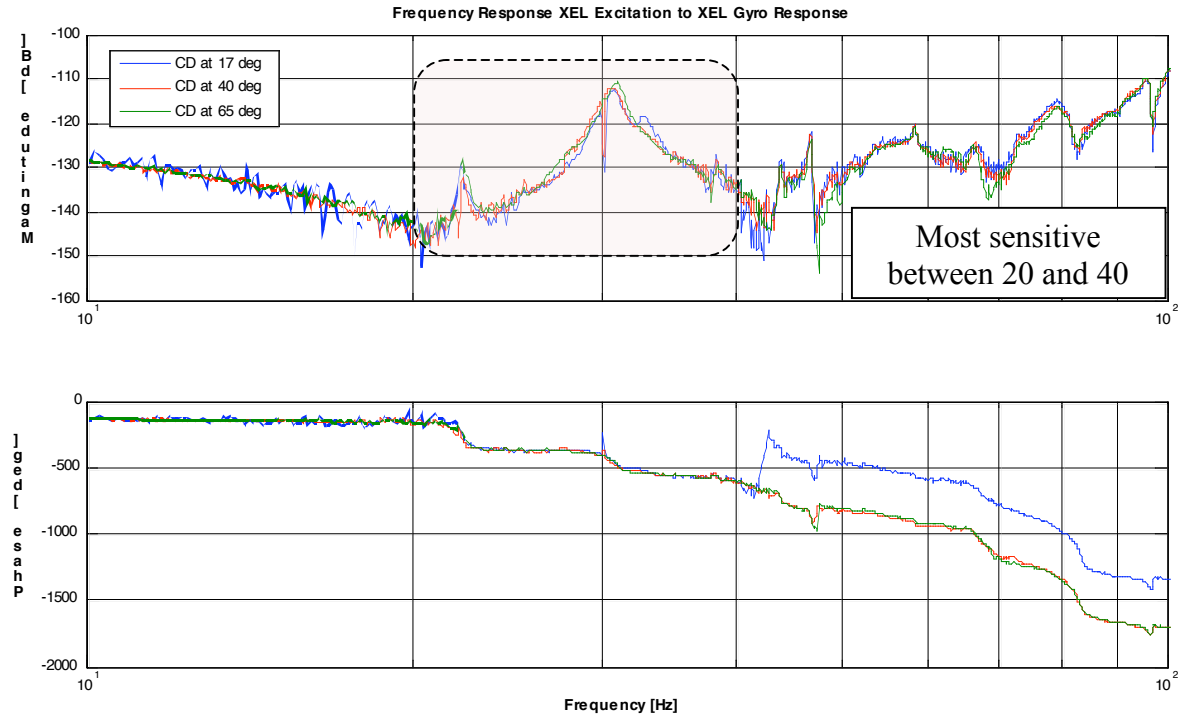

Figure 10

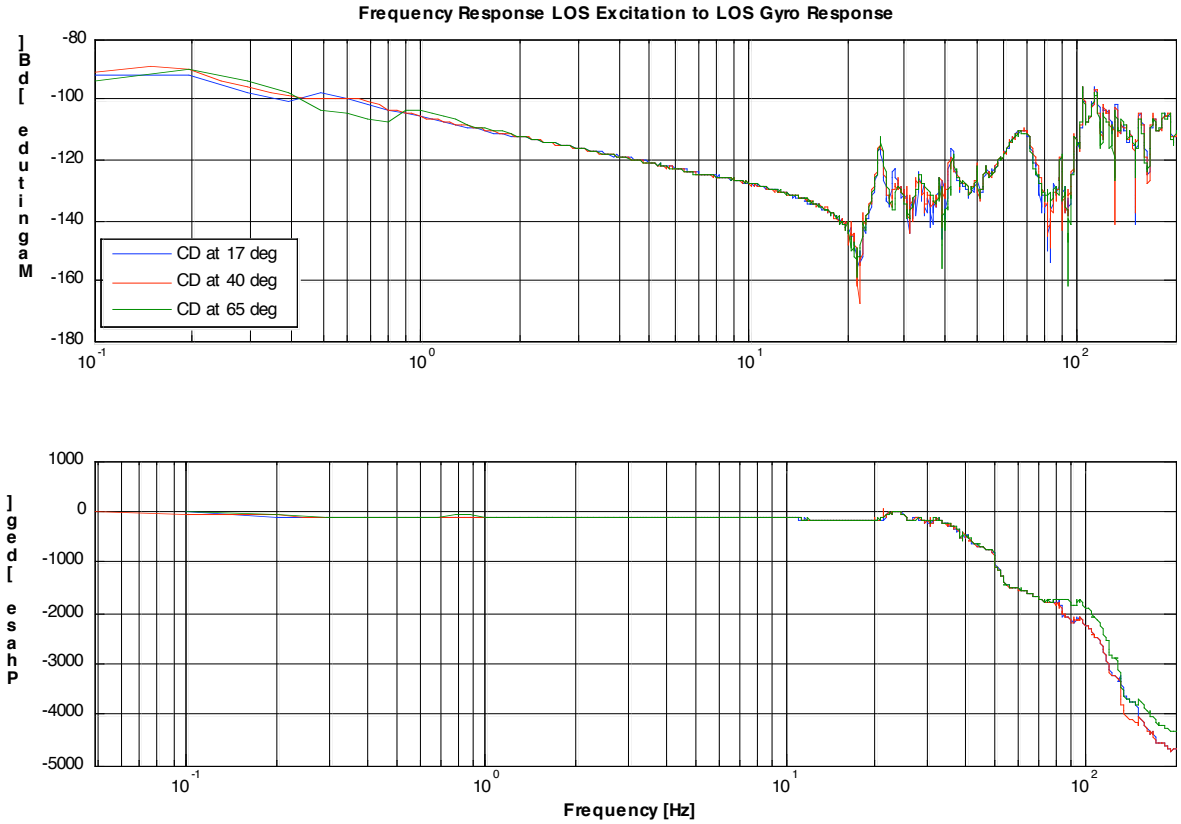
Frequency Response LOS Excitation to LOS Gyro Response
]Bd[edutingaM
-80
-100
-120
-140
-160
-180
CD at 17 deg
CD at 40 deg
CD at 65 deg
10^-1
10^0
10^1
10^2
]ged[esahP
1000
0
-1000
-2000
-3000
-4000
-5000
Frequency [Hz]

Figure 11

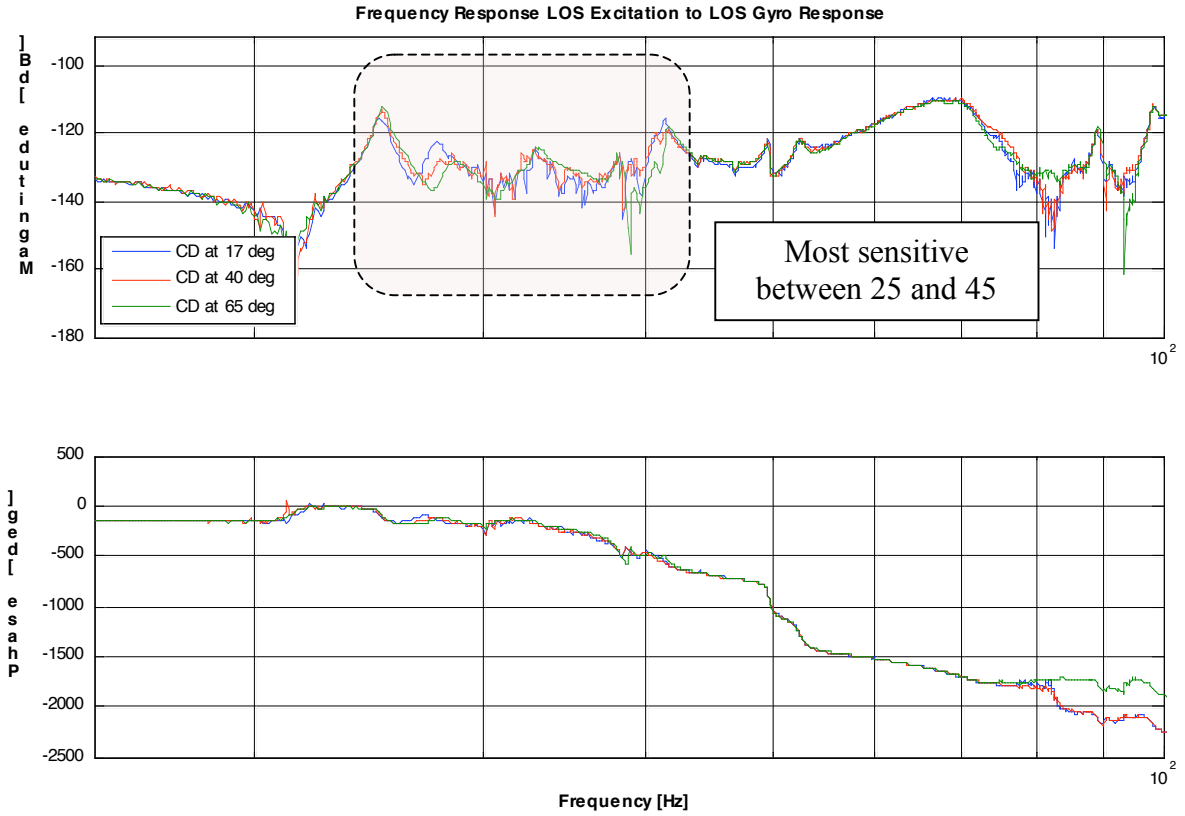

Figure 12

Comparison of HIPO Configuration to SI Mass Dummy Configuration

Figures 13 through 18 present comparisons of transfer functions measured at 40 deg CD elevation angle with HIPO installed (blue) and the SI Mass Simulator installed (green). Figure 13 compares the transfer functions of the EL axis control plant. Figure 14 is a zoom into the most sensitive frequency ranges between 25 Hz and 40 Hz, and between 55 Hz and 80 Hz.

Figure 15 compares the transfer functions of the XEL axis control plant. Figure 16 is a zoom into the most sensitive frequency range between 25 Hz and 40 Hz, and between 55 Hz and 95 Hz.

Figure 17 compares the transfer functions of the LOS axis control plant. Figure 18 is a zoom into the most sensitive frequency range from 25 Hz to 55 Hz and above 75Hz.

Compared to the CD elevation, sensitivity to SI mass changes is more significant and influences a larger bandwidth. The HIPO Line Ops showed that the currently implemented controller is robust against changes in SI mass, as the controller was designed based on data gathered with the SI Mass Dummy and no changes had to be made after HIPO was mounted. Other Science Instruments will be studied when they are

mounted. It is understandable that the control plant is sensitive to significant changes in the structure like a changing SI, and with future more aggressive controllers we will likely have to deal with those effects.
Sensitivities like the ones measured above make the TA interesting from a controls point of view: the (disturbance) environment will be likely fairly constant at the work point (temperature, aeroacoustic loads, inertial loads), but the control plant itself will change its characteristics frequently between flights! Optimal multivariable feedback controllers need to be robust to those changes.

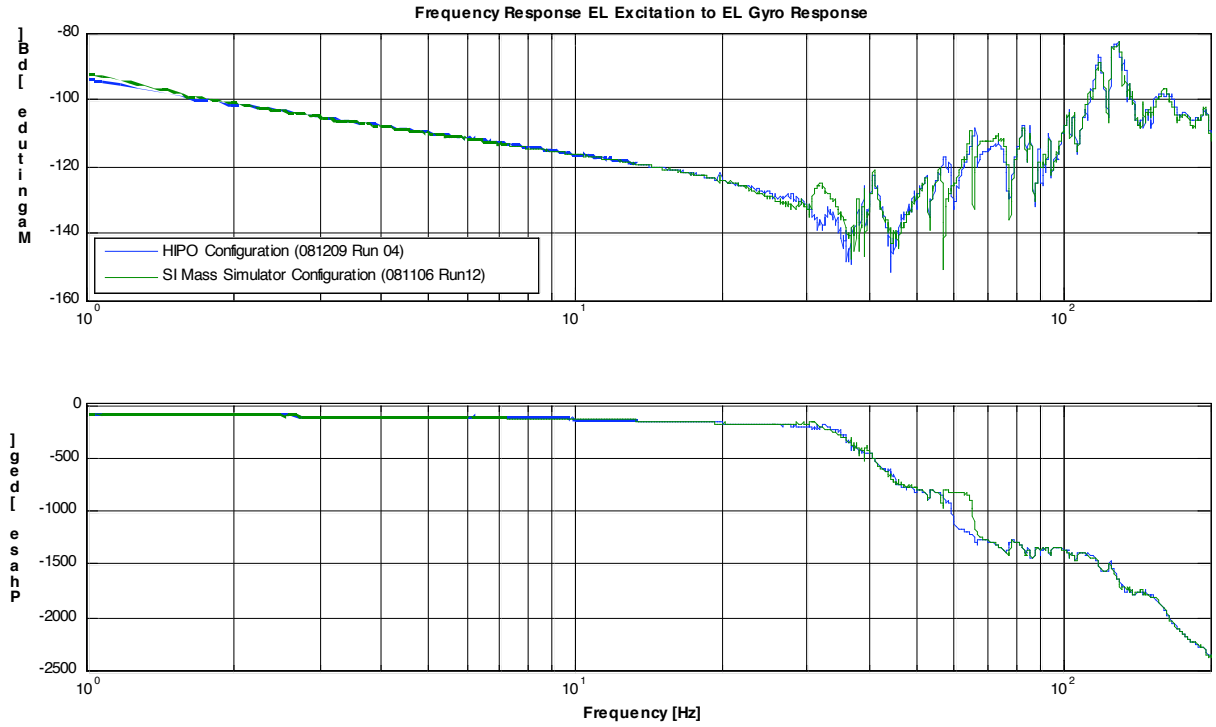

Figure 13

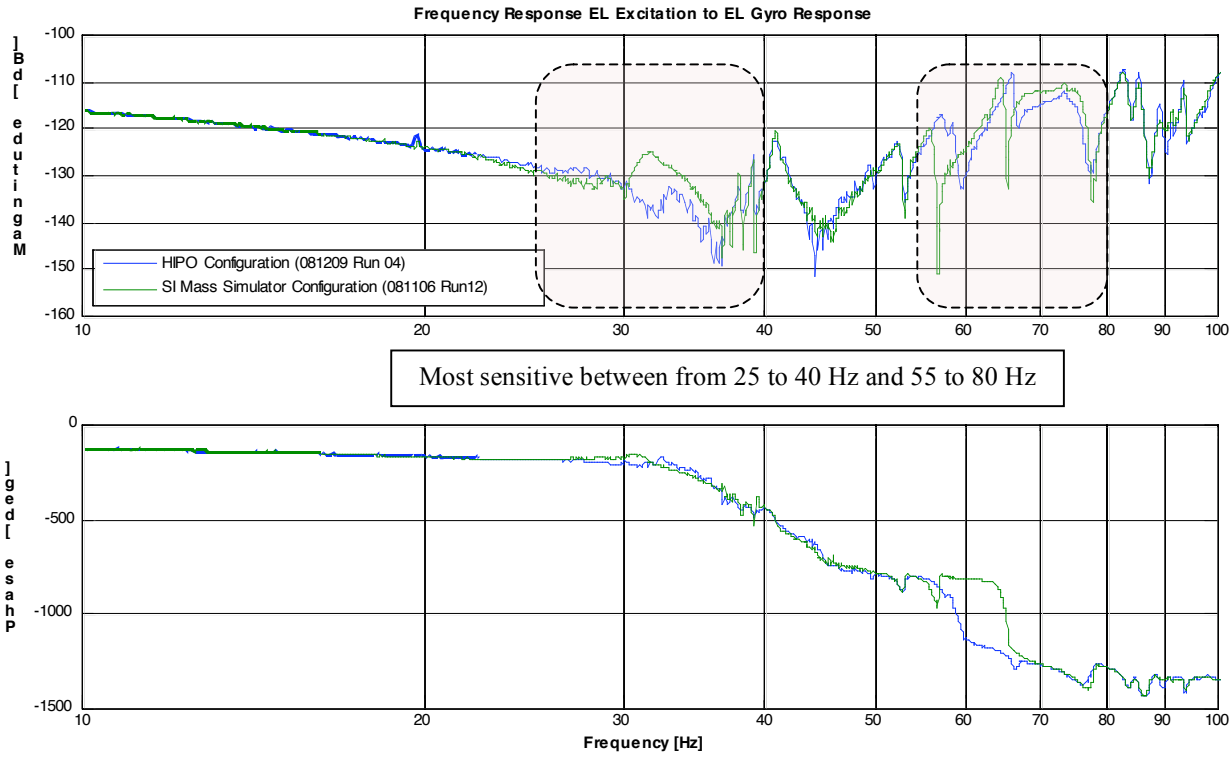

Figure 14

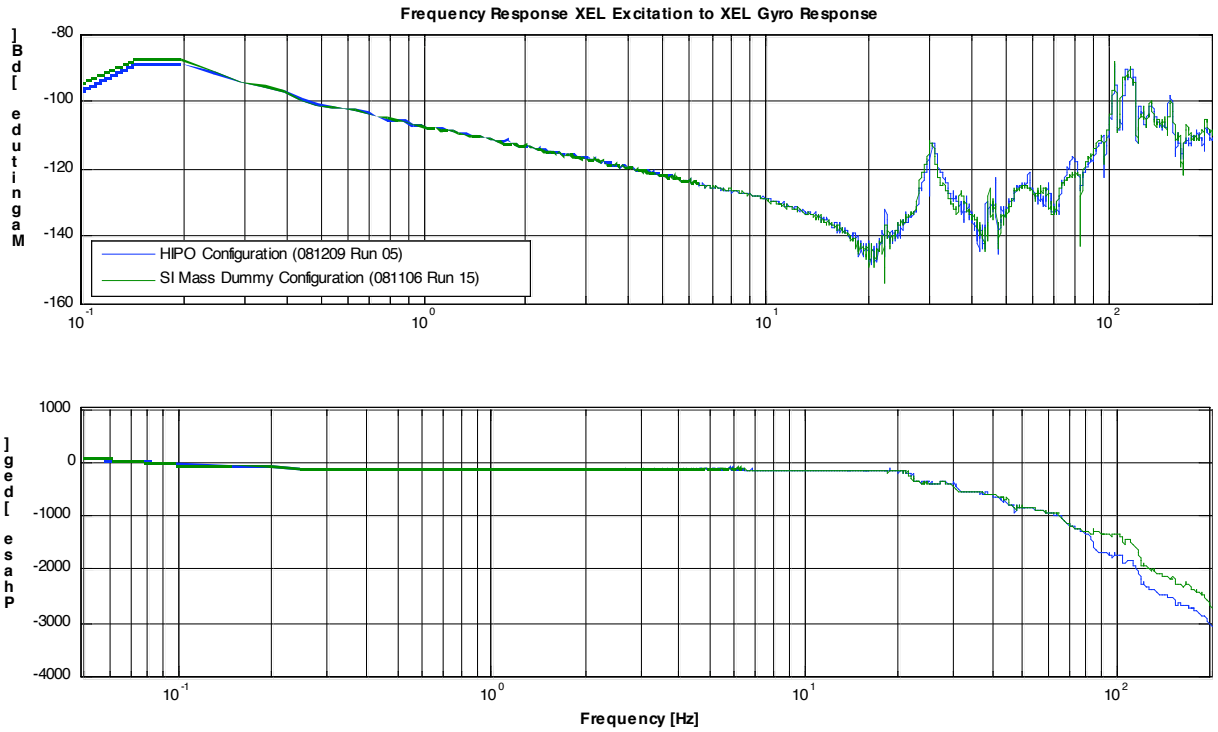

Figure 15

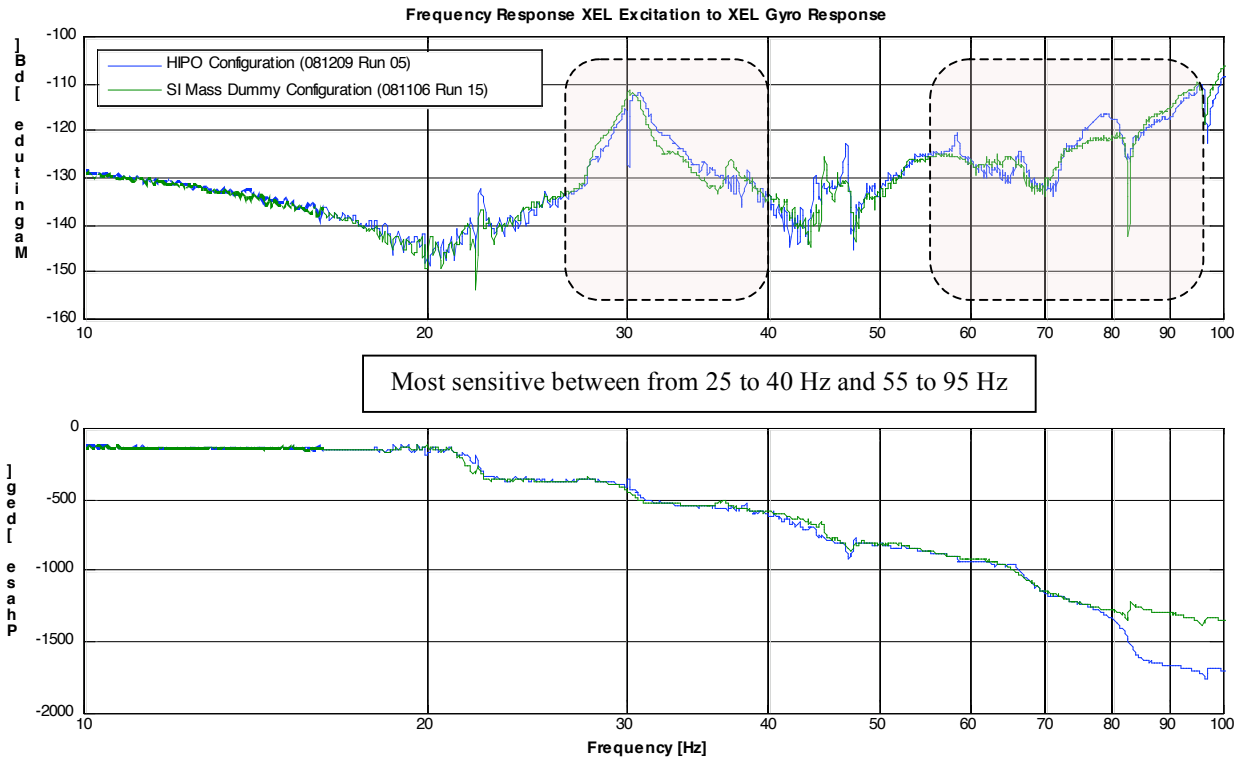

Figure 16

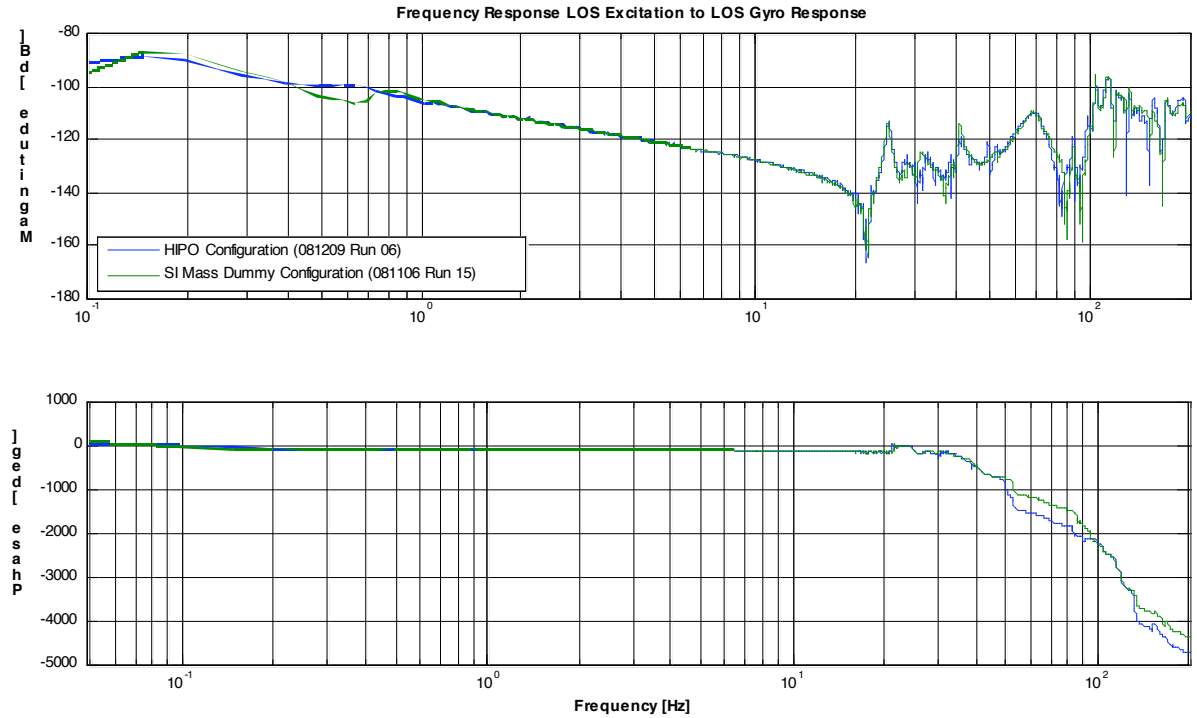

Figure 17

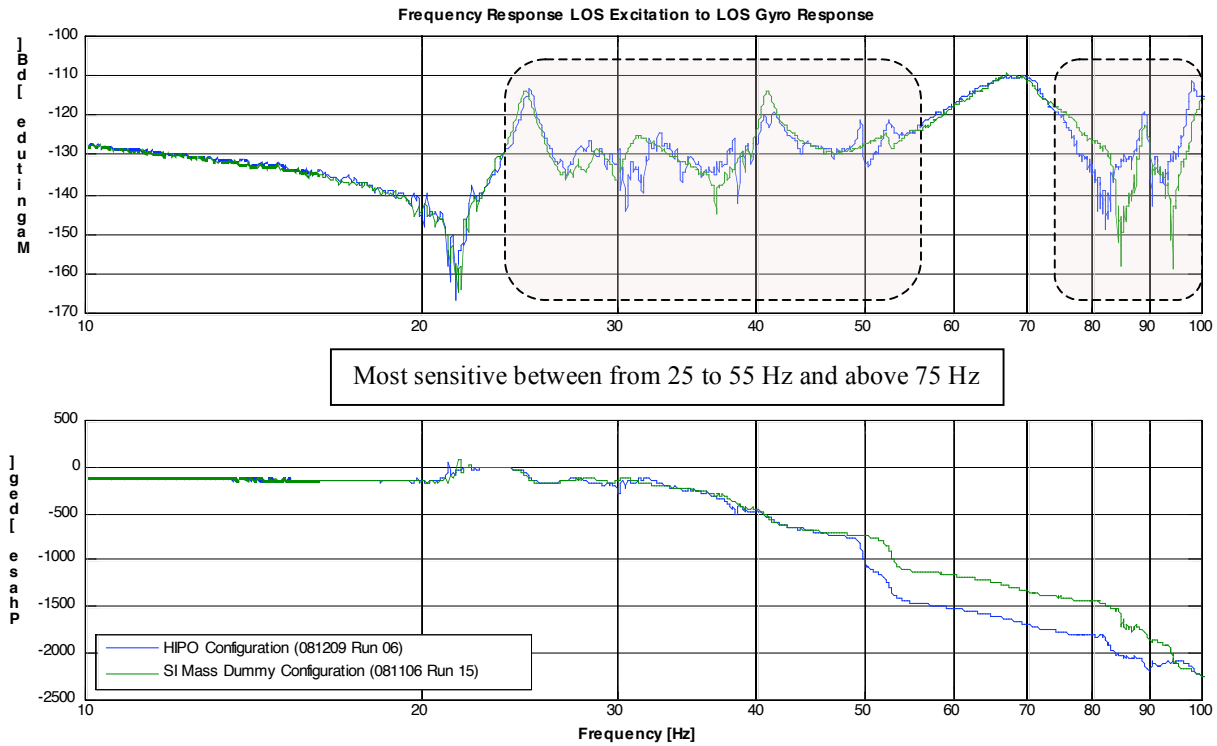

Figure 18

Control Plant Delay

Every real control plant, in particular in digitally controlled systems, will include time delays due to signal processing etc. Time delays cause phase shift in the plant transfer function that is linearly dependent on the frequency, i.e. a phase lag that will increase with frequency. This phase lag "eats up" phase margin, a major stability criterion for control systems. The only way to achieve sufficient gain margin is to reduce the controller gain and thus to give up some bandwidth. Figure 19 presents the time delay measured in the fine drive control system. The dotted line was derived from the end-to-end simulation and contains no delay (the phase is constant at -90 deg in the rigid body regime). The black line represents data from system identification, where a roll off in phase can be seen in the rigid body regime. As an example the EL axis transfer function is shown, but the same delay is seen in all axes.

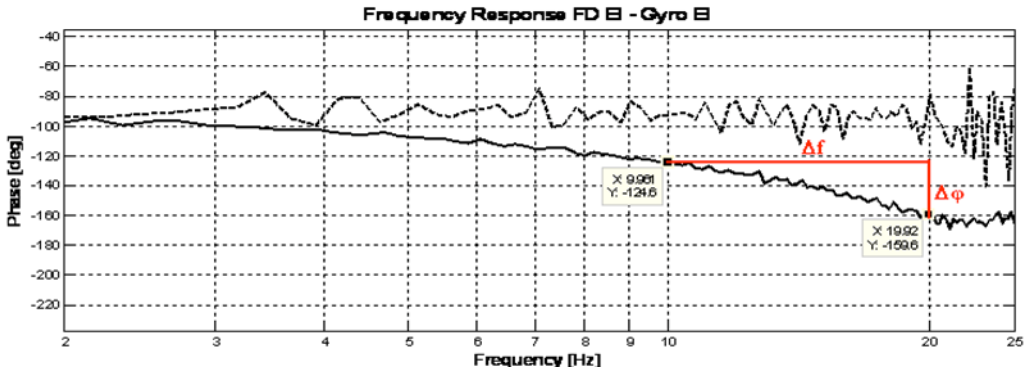

Figure 19

$$T_D = \frac{\Delta\varphi}{2\pi \cdot \Delta f} = \frac{0.61 rad}{2\pi \cdot 10 Hz} = 0.0097 \sec$$

The calculation of the loop delay is straightforward per the above formula and yields 10ms. This is a fairly high value and up to now only 6.25ms can be accounted for by ATCU and TASCU signal processing (2.5 cycles). The additional 3.75ms cannot be explained at this point. Investigations on this will be done, but for early science the achievable bandwidth is sufficient.
Apart from finding and (if possible) eliminating the additional time delay of 3.75ms we are also discussing the possibility to increase the TASCU fast loop rate from 400Hz to 800Hz or higher. This will cut down the signal processing time and hence the delay significantly.

Closed Loop Transfer Functions

Open loop transfer functions are used to analyze the plant characteristics and to quantify closed loop stability. In contrast, closed loop transfer functions can be used to quantify the controller performance in terms of bandwidth. The higher the bandwidth, the faster the controller reacts.
Frequency response functions are shown below (figures 20 to 22) with both velocity and position loop closed and random excitation at the position loop command input. Measured data (blue) is overlaid with simulated data from the controller design (dotted green). The controller design was based on SI mass dummy data. Bandwidth measurements are based on the 90 deg phase lag definition.

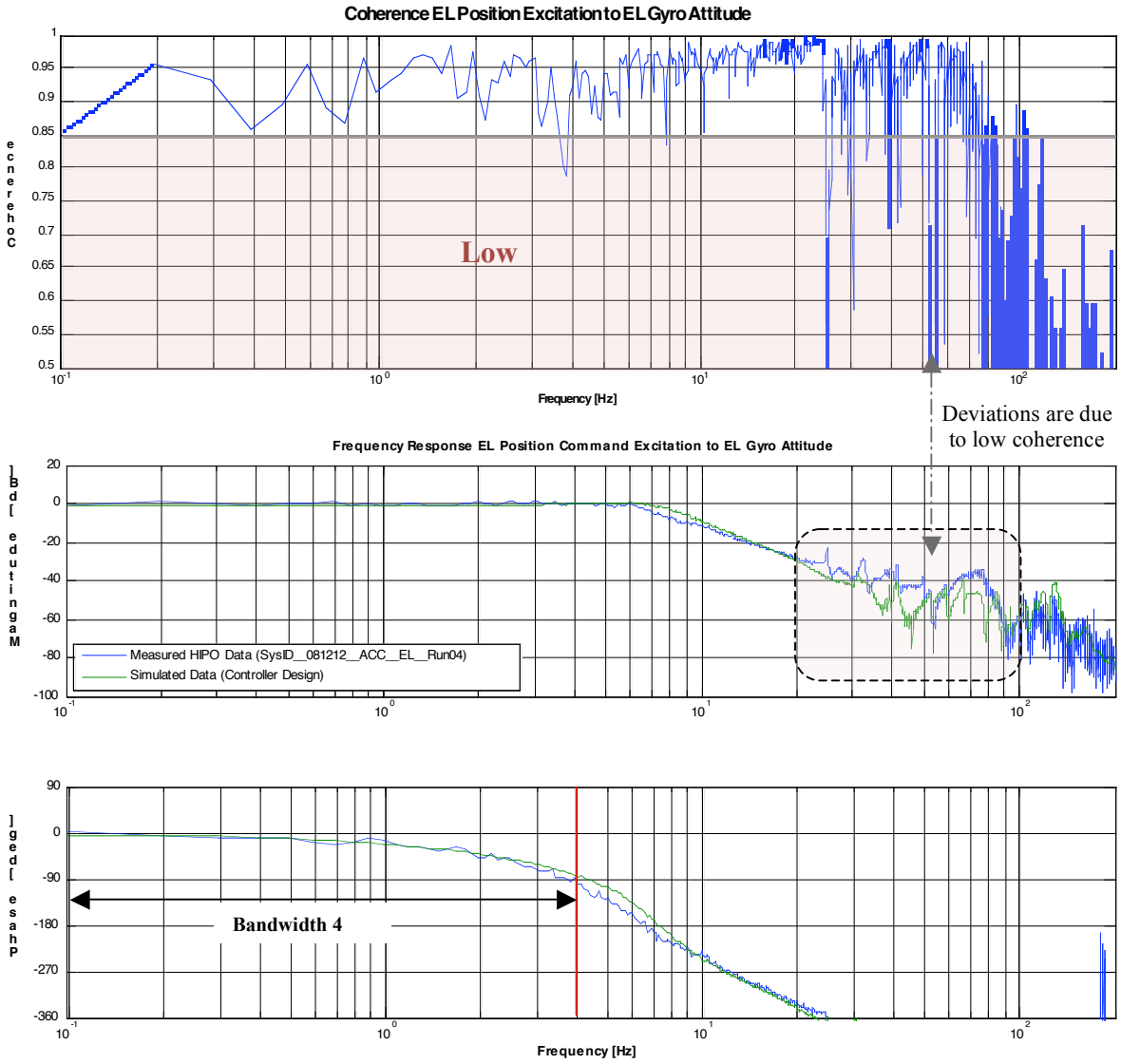

Figure 20

It is difficult to achieve good coherence between input and output signal when performing a closed loop measurement, since the amplitude of the commanded position signal needs to be very small to avoid saturation of the Fine Drive torque motors. Therefore coherence depends heavily on the controller gains, which are per design acting in a limited frequency band. Results are good in the low frequency range (where control authority is high), and correlate well with the simulation[1] performed during controller design. At higher frequencies coherence gets worse and hence the correlation between simulation and measurement deteriorates. But the measurements are reliable when they are used to measure the controller bandwidth, and the overlay between measurement and simulation shows that we achieved the bandwidth we design the controller for.

[1] Note: controller design is based on system identification (=measured) data. The "simulation" of the closed loop is based on the measured frequency responses and no physical or modal model was used in order to minimize errors

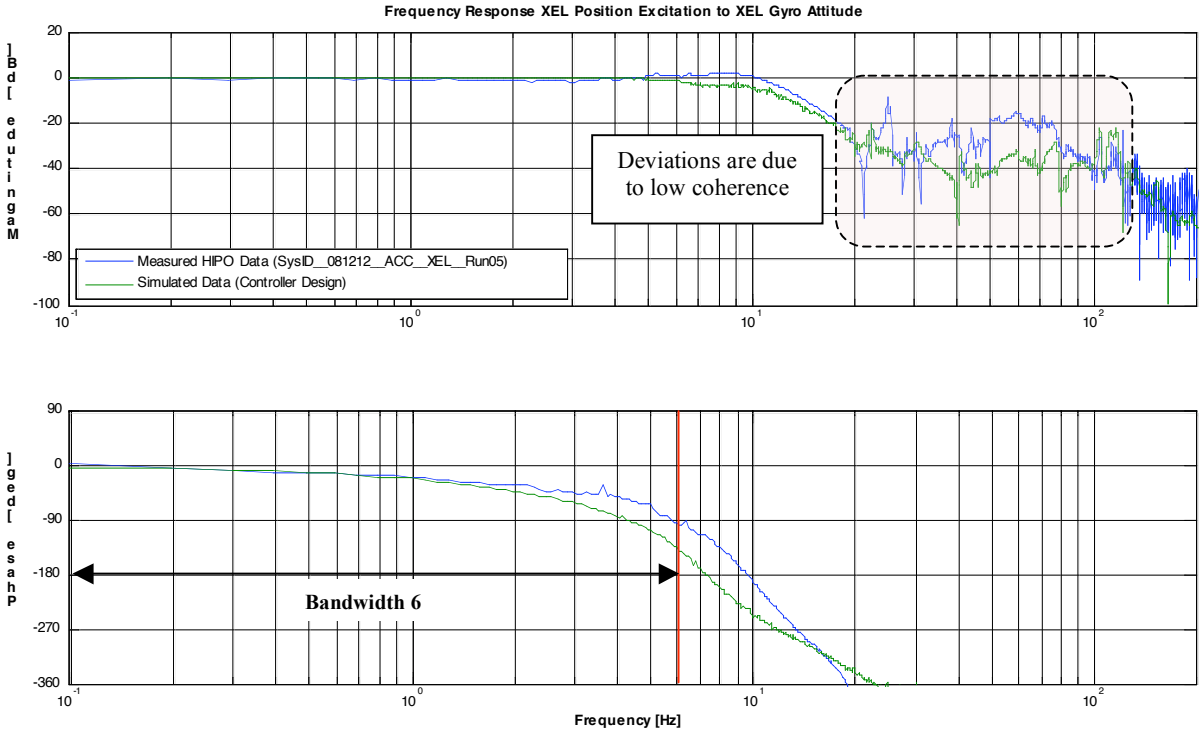

Figure 21

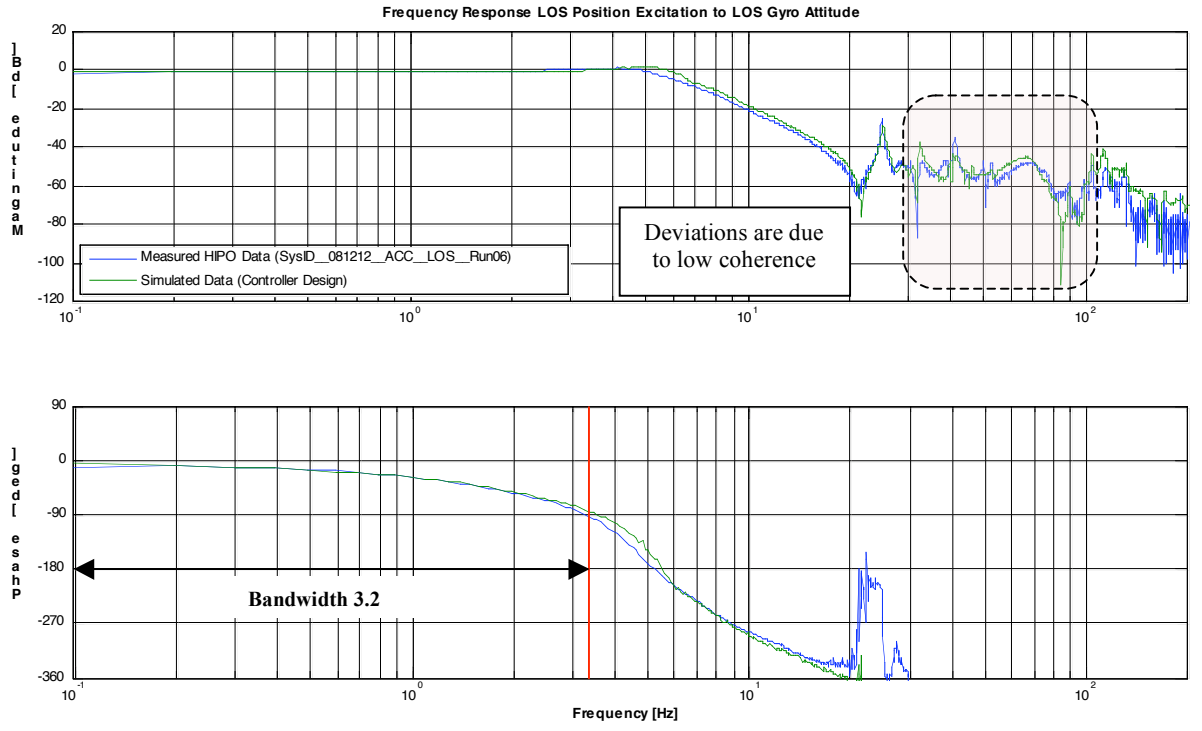

Figure 22

The time delay in the control plant induces a phase lag that grows with frequency and this „eats up“ phase margin. This limits the controller bandwidths to 4-6 Hz at this point. In order to achieve higher bandwidths (~7-8 Hz) we will have to reduce the 10ms delay. The following table summarizes the controller bandwidths as measured during the HIPO Line Ops, based on the 90 deg phase lag rule.

Axis	***Bandwidth (90 deg phase lag)***
Elevation	*4 Hz*
Cross Elevation	*6 Hz*
Line of Sight	*3.2 Hz*

Elevation and Cross Elevation look really good. The Line of Sight controller could be made a bit faster, although the overshoot (see step response section) is already very high. Note that a fast LOS controller is not as important as EL and XEL to achieve good pointing stability.

Next Steps:

- Redo this with FORCAST and compare to the SI mass dummy and HIPO.
- Work on strategies to reduce plant delay
- Consider plant sensitivities during controller improvements and test sufficiently

TC-HIPO-08 Part 2: Step Response

Introduction:

The step responses discussed in this section show the closed loop characteristics in the time domain. Position steps were commanded without using the trajectory generator, which avoids limit cycling but also increases the settling time. Instead the position steps were limited to a size that did not saturate drives. The results were scaled to represent a unity step. The respective scaling factors were then used to add 1 arcsec thresholds above and below the unity step. Once the measured position is within ± 1 arcsec the TASCU considers a TA motion to be settled. Consequently, those values were used to derive the settling times of the closed loop system in this report. The results are shown in figures 23 through 26 with overshoot and settling times presented in tables below the respective plots.

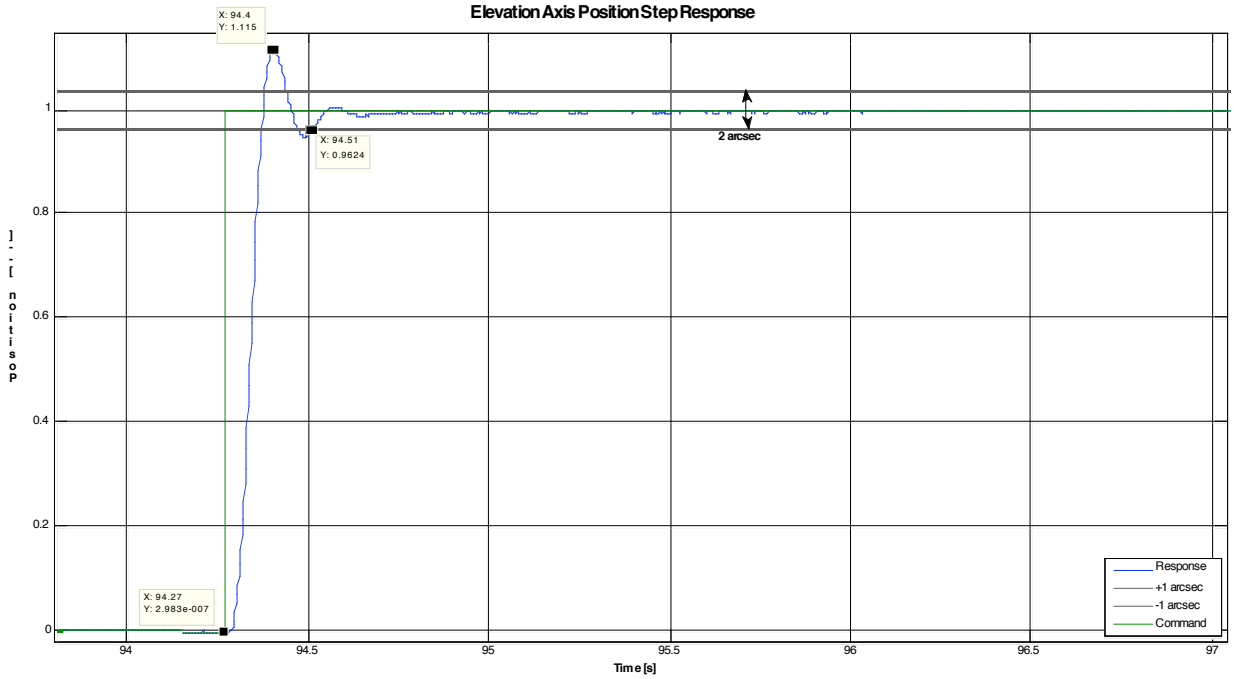

Figure 23

Elevation Axis Step Response Parameters	
Overshoot	*11.5 %*
Settling Time (within 1 arcsec)	*0.24 sec*

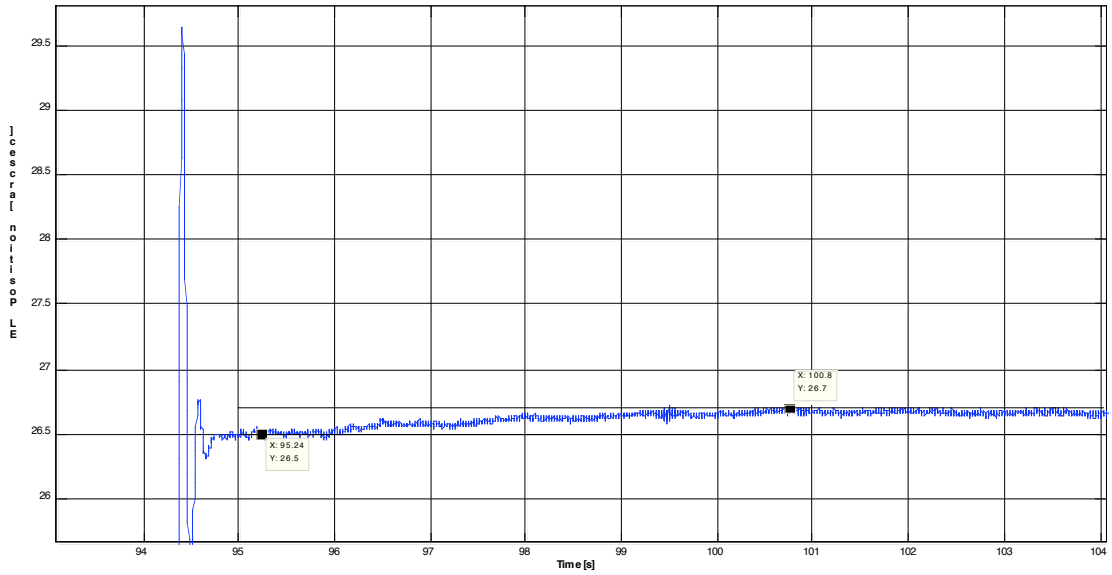

Figure 24

Figure 24 presents a zoom into the EL axis step response and shows that the desired attitude is not reached exactly. This effect is still being studied, but it seems that there is a low frequency oscillation with an amplitude of about 0.2 arcsec, which is likely due to the integral gain in the PID controller. The integral gain is necessary to achieve stationary accuracy of the position loop (pointing accuracy), which comes at the cost of this low frequency oscillation.

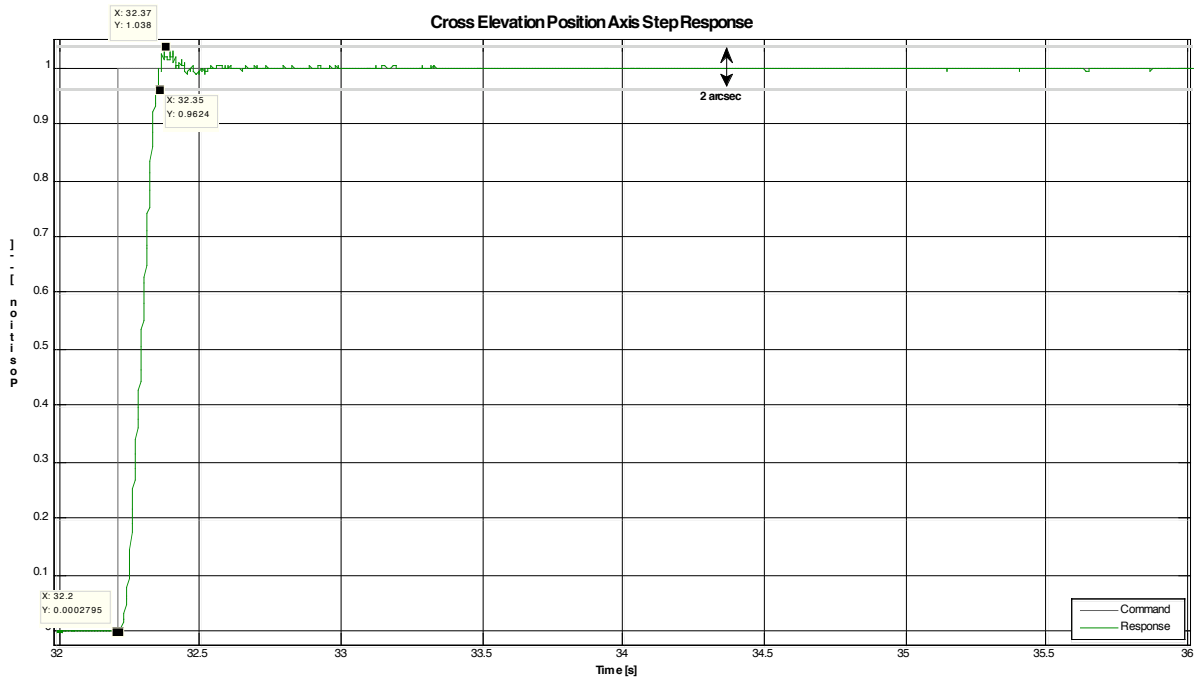

Figure 25

Cross Elevation Axis Step Response Parameters	
Overshoot	*3.8 %*
Settling Time (within 1 arcsec)	*0.15 sec*

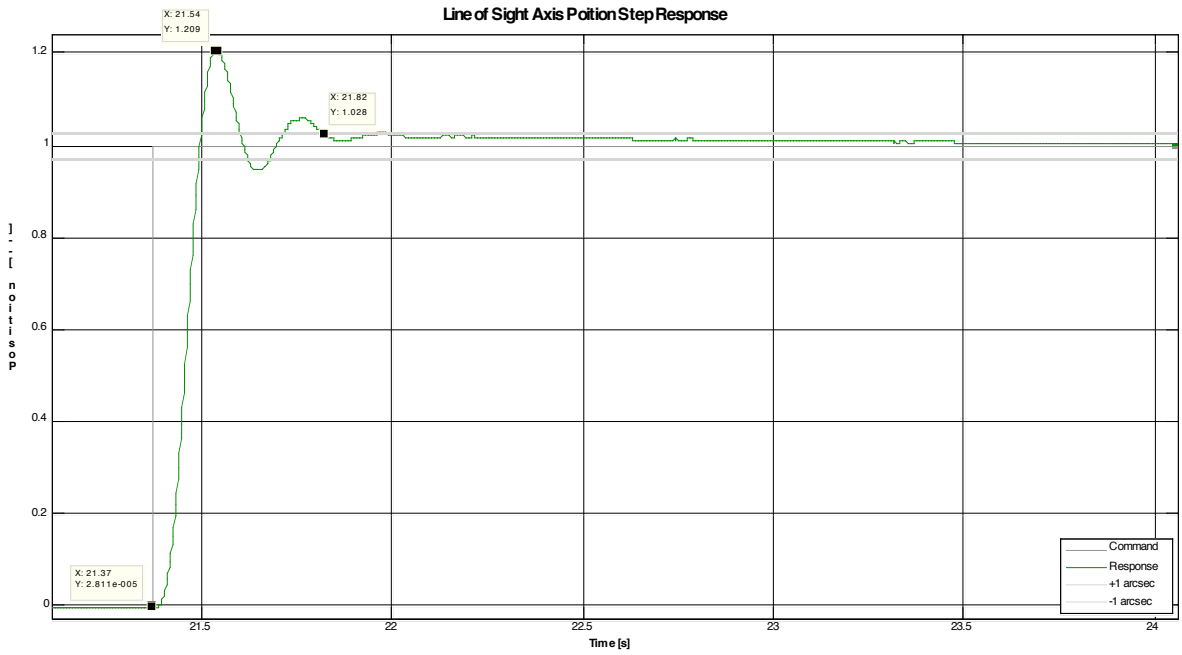

Figure 26

Line of Sight Axis Step Response Parameters	
Overshoot	*20.9 %*
Settling Time (within 1 arcsec)	*0.45 sec*

Next Steps:

- Redo this with FORCAST and compare to the SI mass dummy and HIPO.
- Work on optimization of LOS controller

TC-HIPO-08 Part 3: Disturbance Rejection

Introduction:

The intent of the original plan was to observe the image at high speed using the pipelined occultation mode. The star needs to be off the center of the SI flange in order to do this and the complication of LOS resets, off-axis operation, and the limited range of the connecting rod to the shaker made this impractical. Instead we used 4x4 binned basic occultation frames taken at 80 ms/frame.

Goal was to test the Fine Drive controller under the influence of external disturbances, and getting a first impression of the image stability in the focal plane that can be expected during early science. Initially, those tests were performed with an external shaker located in the cavity, exciting the TA structure at a PMA whiffle tree. Later (14 Dec 2008), the test was repeated using random torque injection into the Fine Drive system (closed loop) instead of using a shaker. When the shaker was attached to the telescope on 11 December (UT) the telescope pointing remained reasonably stable up to force levels up to 0.75 lbs rms (white noise within a 0-200 Hz band) but exhibited anomalous behavior at or above 0.97 lbs rms. The incorrect operation was characterized by the star image jumping from one stable location to another location some distance away. Over a period of minutes and multiple jumps the star image could move entirely out of the HIPO and FPI field of view. The same effect was seen when we used the Fine Drive Torque Motors as excitation source.

Figure 27 below shows the correlation between events. Every now and then, the ATCU warning (figure 27c) changes its value from 0x00 to 0x90000, which means a GyroUnitFault occurs. When this happens, the measured Gyro rate values of the respective cycles are ignored and the old values from the last cycle are kept. At the same time a torque peak occurs (figure 27b), which leads to a TA motion that remains now undetected by the Gyroscopes (figure 27a). As a result, the image of a star in the focal plane makes a step motion; it “jumps” to a new average position (see FPI v direction centroid position in figure 1d).

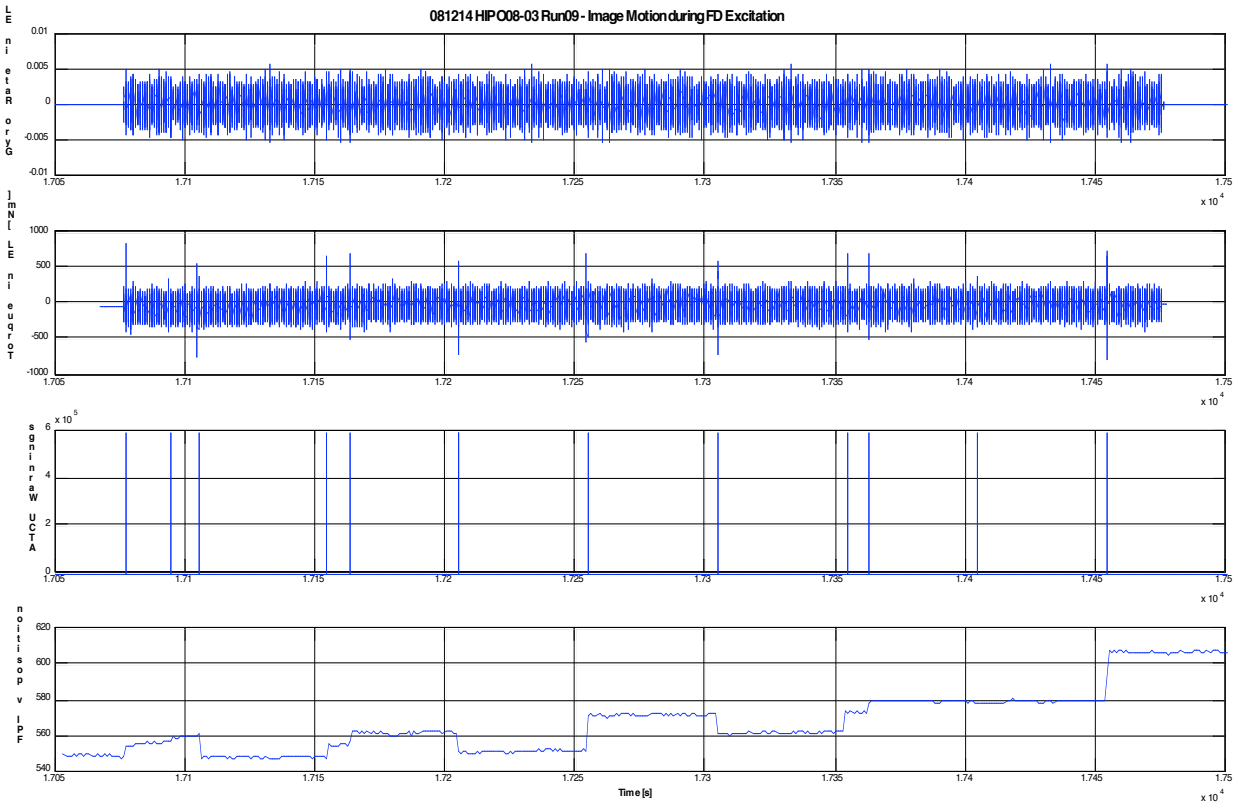

Figure 27

Where do the torque peaks come from?

Behaviour of the Elevation Axis

The peaks can either come from the disturbance torques that get injected into the system or from within the closed loop itself. Figure 28 below shows that the injected torque signal does not include peaks like the ones observed during the test.

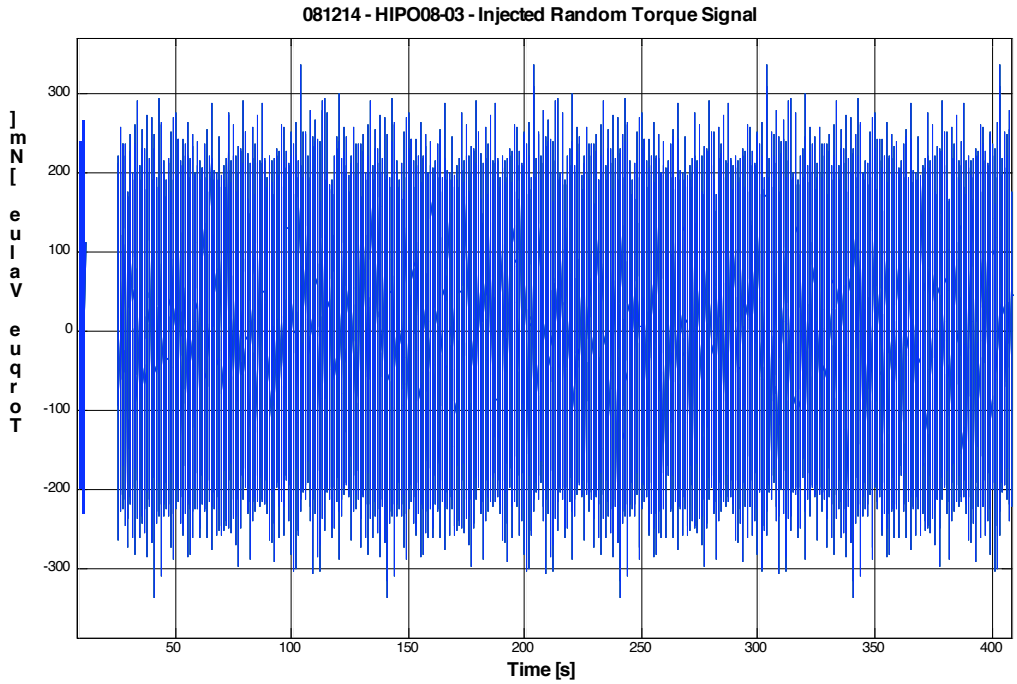

Figure 28

This means the torque peaks have to be generated within the closed loop system. In the following we will look at a few plots that give insight to the values of variables that are processed within the closed TA attitude control loop. Figure 29 shows the actual (= measured) attitude that the TASCU uses as feedback signal for the position control loop.

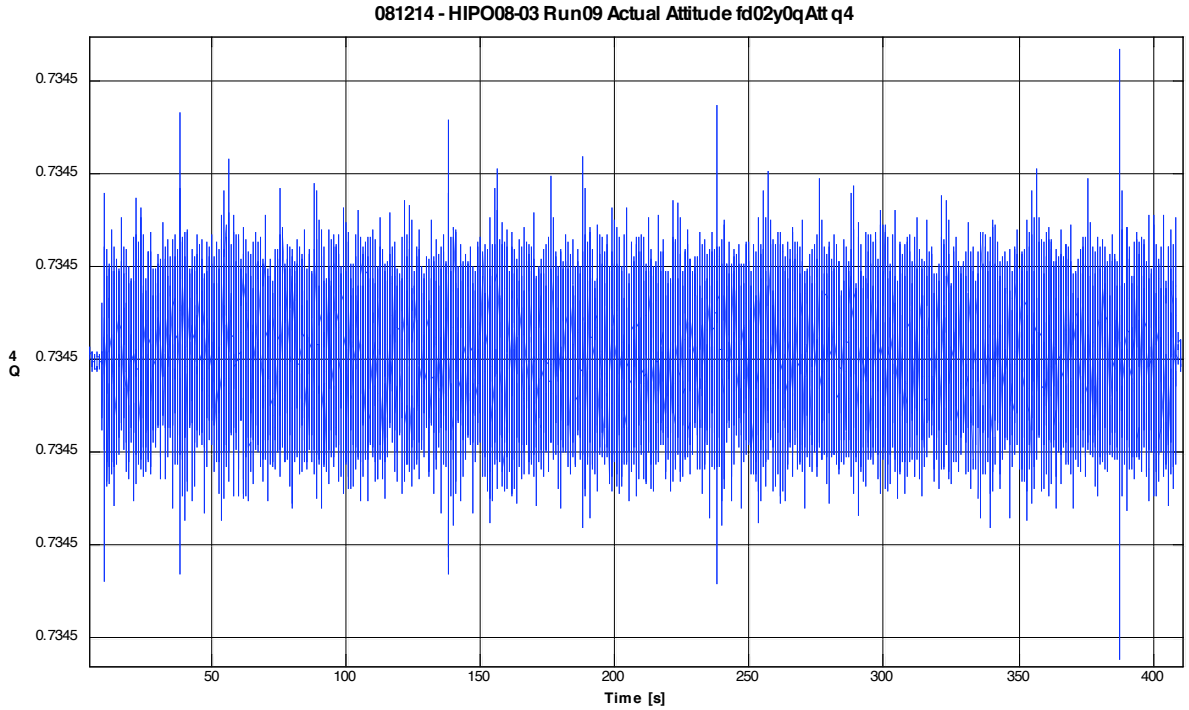

Figure 29

It shows peaks, and this is the reason for the torque peaks we are seeing: the position controller sees a sudden change in the control deviation (error), which is passed through the controller and leads to a torque peak. The position error of the Fine Drive elevation axis controller is plotted in figure 30 below.

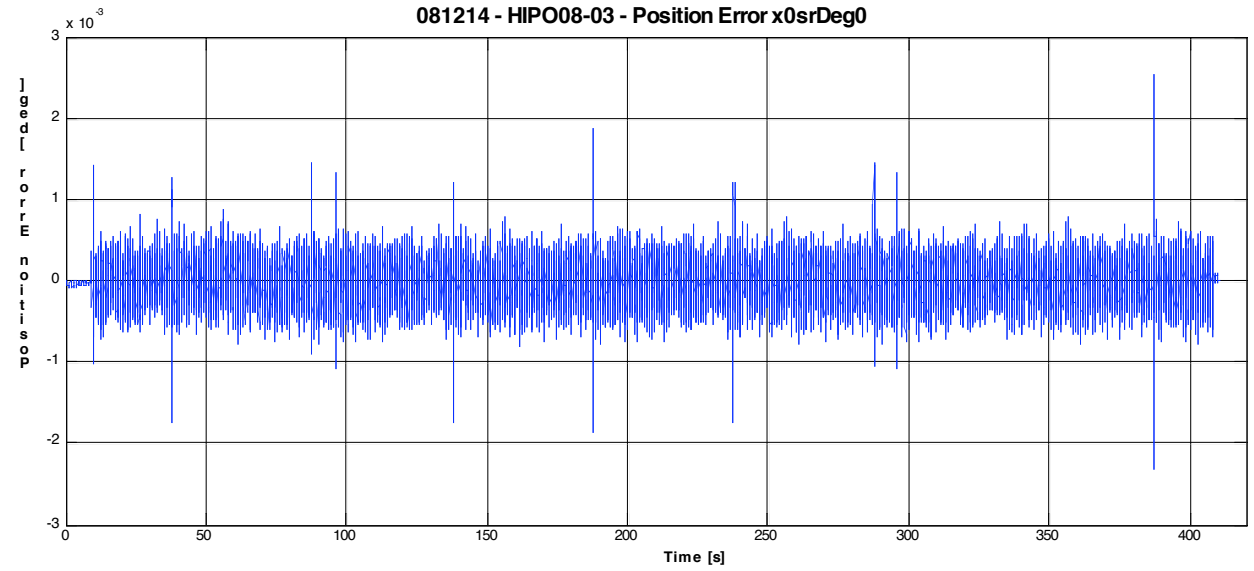

Figure 30

This means although the gyro rate looks okay, the gyro attitude is corrupted and the false information is passed on to the controller, which then slightly moves the telescope to compensate. Figure 31 shows the cumulative sum over the gyro elevation rate, which approximates integration. The peaks can now be seen clearly in the integrated signal.

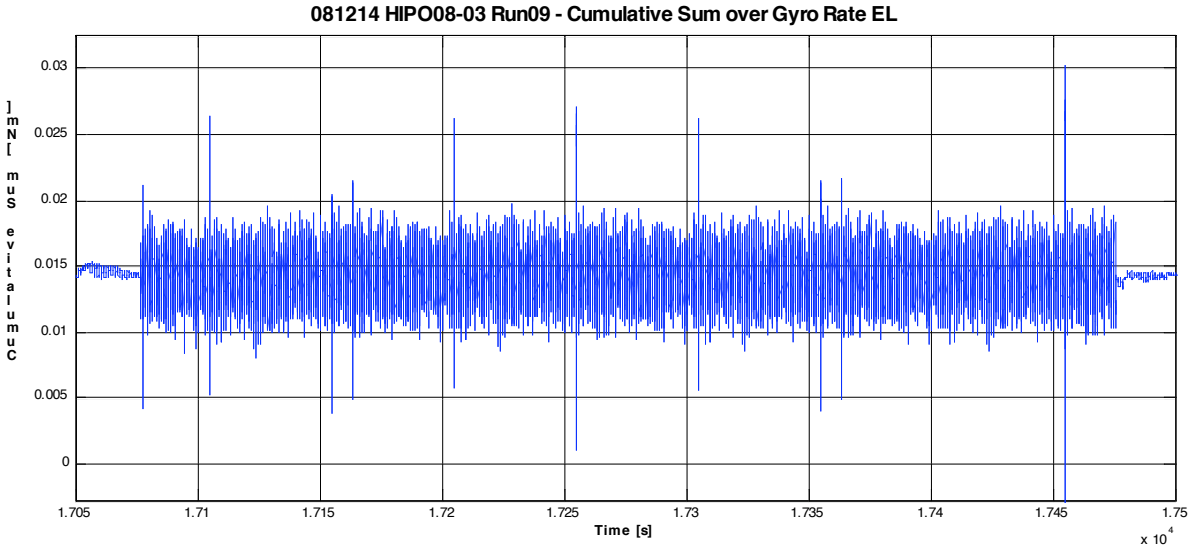

Figure 31

Whenever a "GyroUnitFault" occurs, the gyro signal of this cycle is ignored and the old value from the previous is being used. If the signal changes significantly from one cycle to another, this can lead to a significant error. This error is then being integrated and causes a peak in the "measured" TA position. The controller does what it was designed for and tries to compensate for this. Hence, it commands a move, which then moves the star on the imager.

Reason for the Observed Image Jumps

A new random signal is applied in each cycle, which means we are exciting the structure with a 400Hz signal. With the scaling applied, the torque difference between two 2.5ms cycles can be in the order of 400-500 Nm, which results in a significant difference in the rotational acceleration of the TA. If the Gyro Unit ignores the value of the respective cycle and takes the value from the previous cycle (see figure 32), where, say, a negative torque led to a fast negative rotation, and instead uses the value from the previous cycle, where a high positive torque created a fast positive rotation, this leads to a significant integration error. Since we operate in a closed loop system, this false actual position is reported to the position controller which commands a correction signal. This in turn leads to a torque spike, which moves the image.

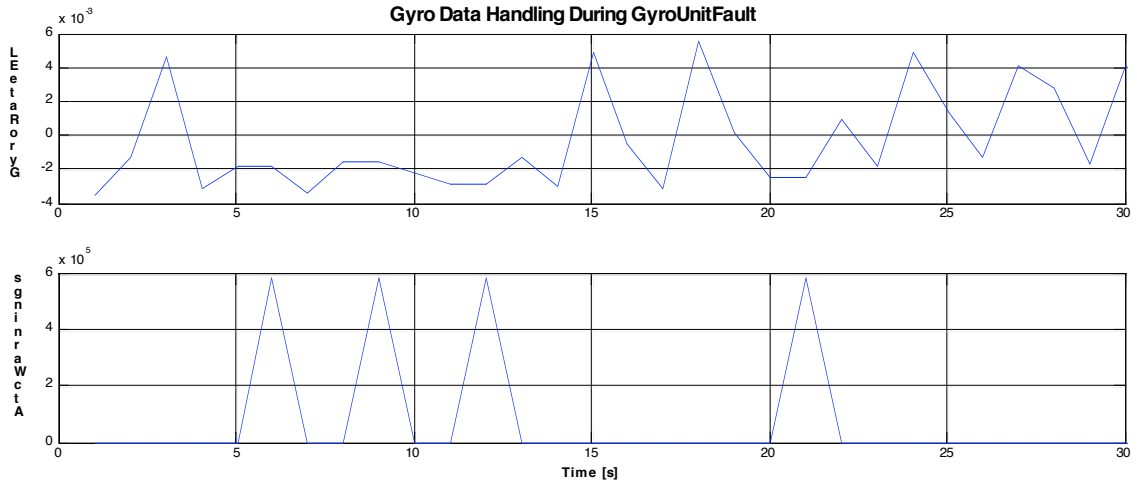

Figure 32

To be more precise, the value that is actually used by the ATCU for the quaternion integration is not the gyro rate per second (which GyroRateEL represents), but a so-called "delta" rate, which is the rate of one cycle rather than averaged over a whole second. But the effects described above still apply, i.e. the torque spikes are caused by ignoring actual gyro deltas in the case of a GyroUnitFault, and taking the values from the previous cycles instead. However, the cumulative sum over the gyro deltas contains not only the spikes visible in the gyro rates, but the actual position steps which are also observed in the imagers. Once the deltas are processed to subtract gyro drift, the cumulative sum over the deltas correlates very well with the image jumps observed in the imagers (see software report on the image jumps by H. Jakob).

Behaviour of the Cross-Elevation Axis

Figure 33 below show the effect of GyroUnitFaults on the XEL axis. TA movements in XEL cause an image motion in w-direction. It is clearly visible that the image motion, as well as the torque peaks, are significantly smaller compared to the EL axis case (with a respective image motion in v).

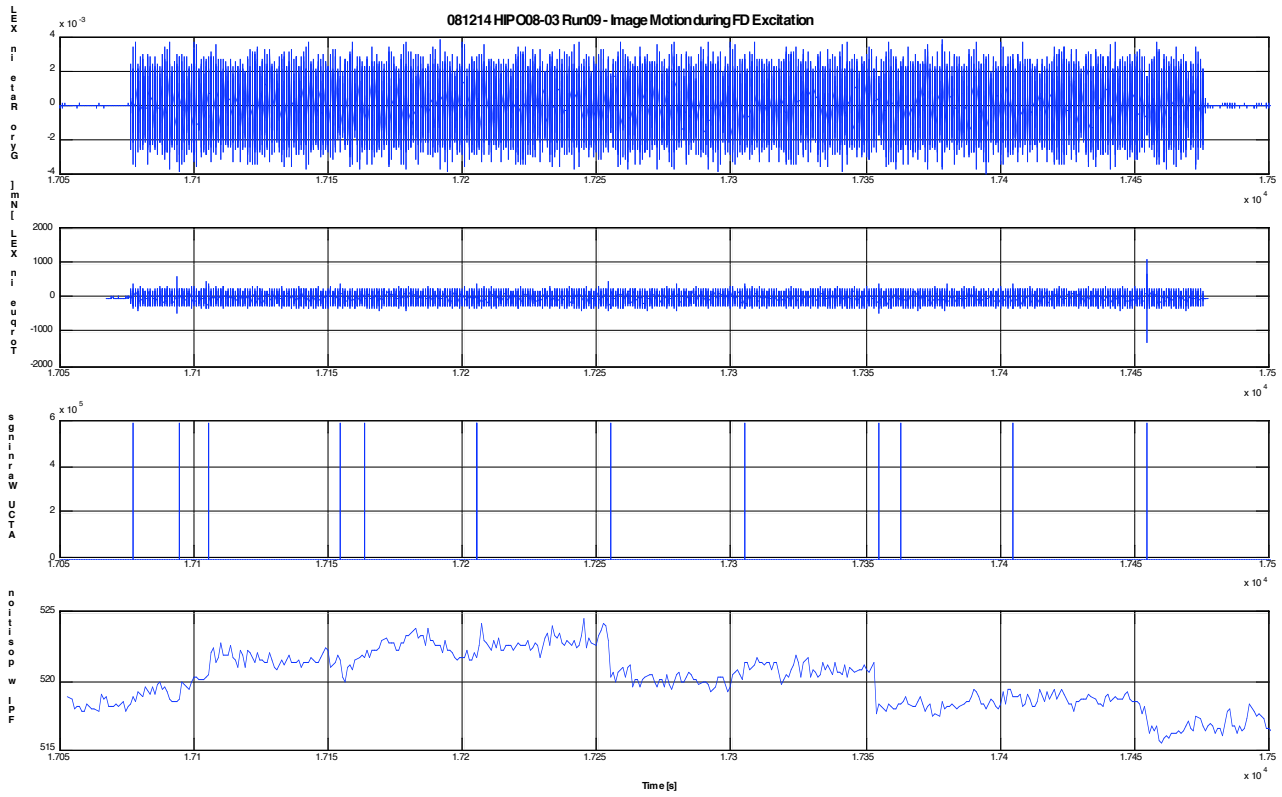

Figure 33

In both, elevation and cross-elevation, the same torque signal was injected during Run 09. However, the rigid body inertia of the TA is a lot higher in XEL:

$$J = \begin{pmatrix} 11390 & 0 & -8021 \\ 0 & 37459 & 0 \\ -8420 & 0 & 40139 \end{pmatrix} kg \cdot m^2$$

This means a given torque results in a smaller TA motion in cross elevation. Hence, the position error is smaller and the integrated position error that is being fed into the position controller is smaller as well. In turn, the commanded position correction and the torque peaks are smaller, thus creating a much smaller image motion. Figure 34 contains the cumulative sum over the gyro rate in XEL. It shows that the integrated error is smaller, as expected.

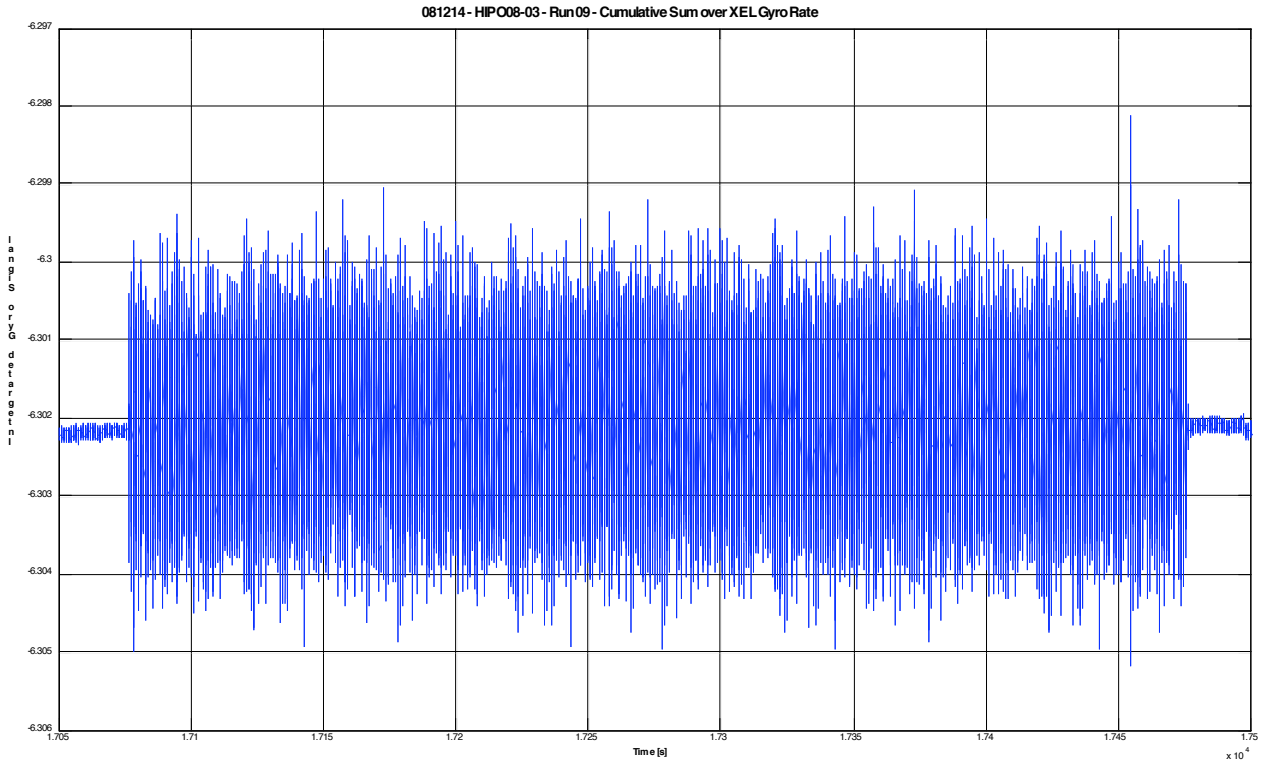

Figure 34

Why does the Gyro show the GyroUnitFault Warnings?

This question still remains to be answered and we are waiting for inputs from the manufacturer IXSEA. A possible solution to the image jump issue would be to use rate and deltas from the gyroscopes even when they are flagged as degraded due to a GyroUnitFault. However, this needs a thorough understanding of what causes the gyros to set this warning flag. But generally using the flagged values seems to work fine and could possibly eliminate image jumps (see software report on the image jumps by H. Jakob).

Looking at unfiltered Gyro unit accelerometer acceleration data from shaker runs on Dec 10 points on a correleation between acceleration and the GyroUnitFault in the respective axis (analysis by Franziska Harms). Figure 35 shows the accelerations measured by the gyro accelerometers and the GyroUnitFault in the v-axis. Data analysis revealed that the warning flag is set mainly due to a degradation of v-axis data. The acceleration data shows that the acceleration amplitude in this axis was significantly larger than in the others. Furthermore, the occurrence of the GyroUnitFault seems to correlate well with the amplitude of the acceleration: the higher the acceleration, the more often the warning flag is set. At the highest amplitudes it gets constantly set.

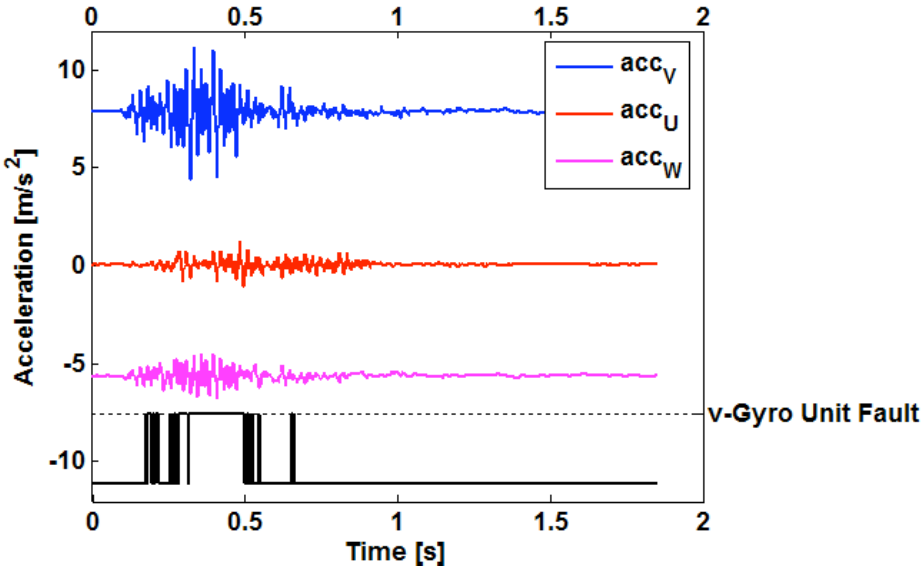

Figure 35

The idea of using gyro data even though it is flagged with a GyroUnitFault warning was analyzed in more detail by Franziska Harms. Figure 36 compares the raw gyro data (blue) to the data that was processed based on the warning flag (red). The red data is used for the quaternion integration in the current ATCU software implementation. When no warning flag is set the red and the blue are on top of each other, otherwise they differ significantly. However, the signal quality of the blue data does not seem to be significantly different from the red data, so the question is whether it is really required to ignore the flagged data.

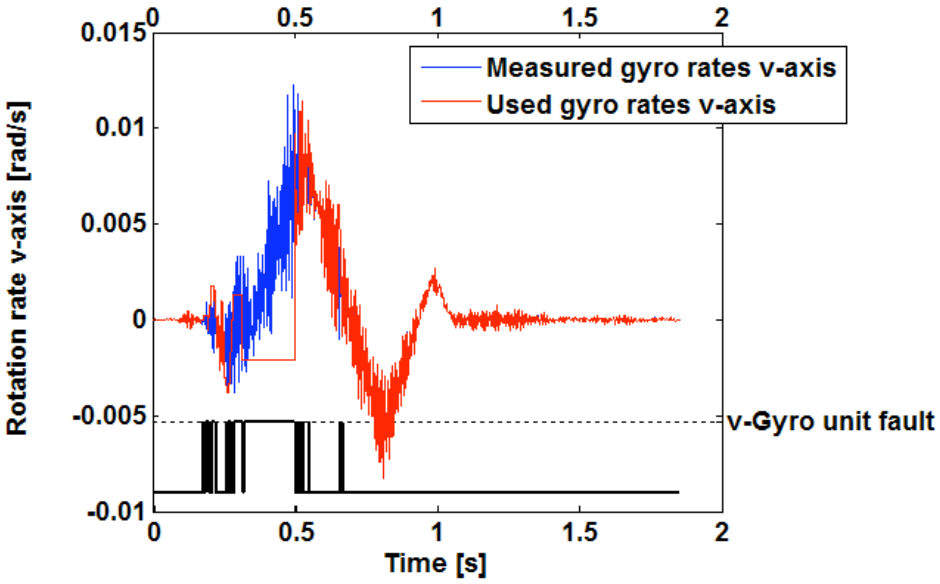

Figure 36

Figure 37 shows the difference between the red and the blue line in figure 36 after the data got integrated. This approximates the quaternion integration performed by the ATCU. The plot shows a step that is qualitatively comparable to what we see in the imager data, and the size of the step is in the same order of what we see in the imagers. If it is possible to reconstruct the image jump from the raw gyro data this proofs that the GyroFault warning is the source of the problem, but it also prrofs that the jumps could be avoided using the gyro data even when it is flagged.

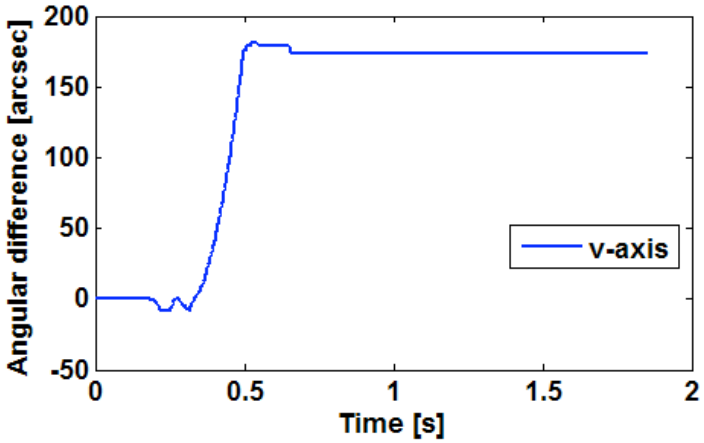

Figure 37

Unfortunately we do not have imager centroid data for the case shown in figure 37 above, but for a less prominent event we do, and the following plots show an estimation of image motion based on the gyro warning flag, along with a comparison with the image motion that was measured by HIPO at the same time.

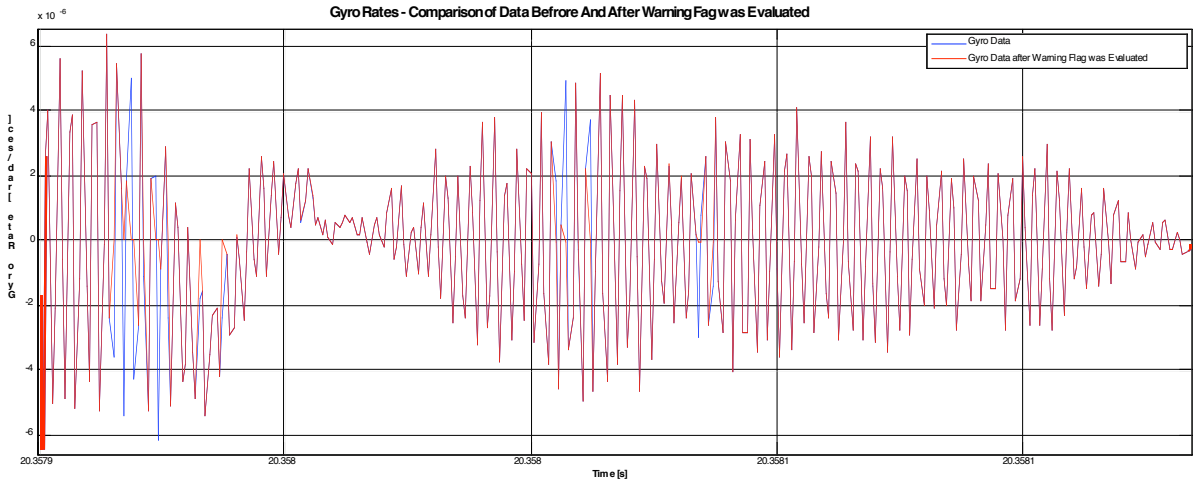

Figure 38

Figure 38 shows a timeframe similar to the one in figure 36. Wherever the blue line becomes visible the gyro warning flag caused the ATCU to set the rates used to zero.

Figure 39 shows the result when those two signals are integrated, just like it is done by the ATCU to calculate the TA attitude. It can be seen that both positions differ significantly. Figure 40 presents the delta between both integrated position signals.

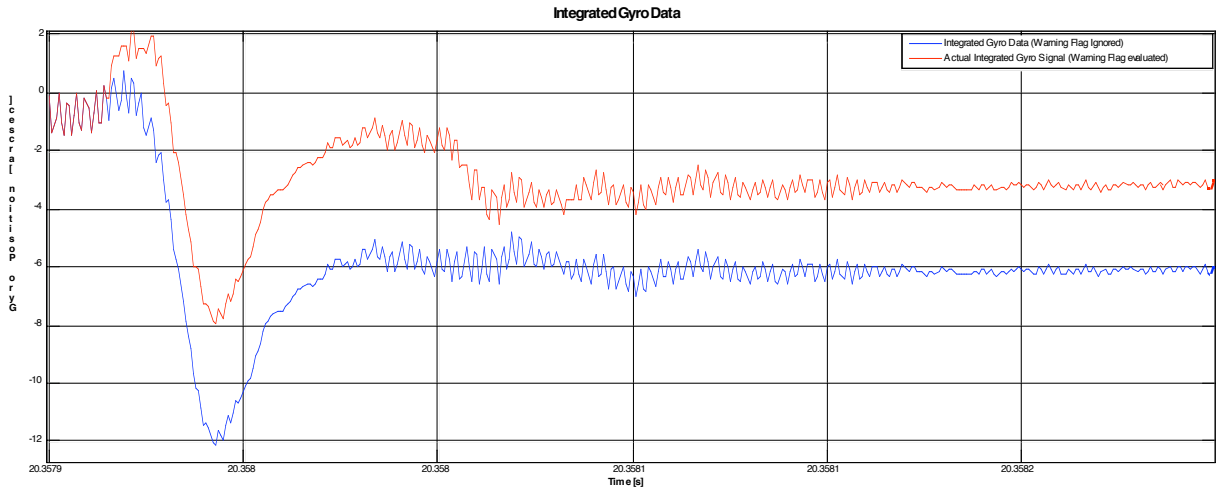

Figure 39

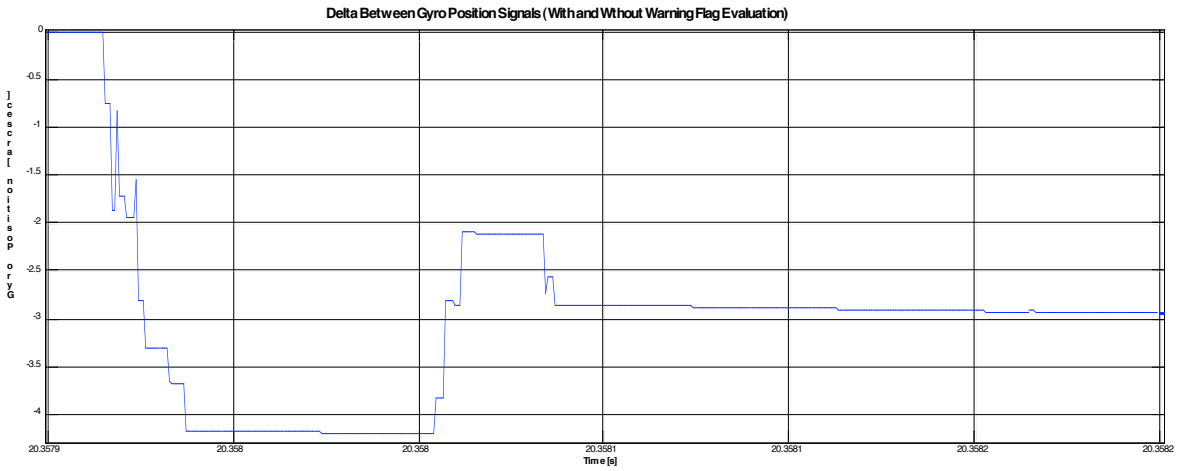

Figure 40

A comparison with HIPO centroid data (see figure 41) shows that the amplitude of the jump is about the same. However, the profile of the jump looks only slightly similar. This is due to the fact that the gyro data was sampled with 400 Hz, whereas HIPO images were taken with a frame rate of 12 Hz. In order to get a better comparion the gyro data was filtered by averaging 33 samples at a time, which effectively reduced the 400 Hz sampling rate to 12 Hz. The results is shown in figure 42. There are still differences to the HIPO centroid positions, but qualitatively the data looks very similar (given the fact that we used fairly crude methods to estimate image motion from Gyro data). The step size of about 3 arcsec measured by HIPO is a bit higher in our estimation (~3.7 arcsec), but at

this point we also relate this to estimation errors. The conclusion is that we were able to reproduce the image jumps well enough and it was possible to determine the handling of the gyro warning flag as the cause of the problem. However, the gyro data looks good enough so that we could use it despite the warning flag and this will likely eliminate the image jumps. See the suggestions below on how to proceed from here.

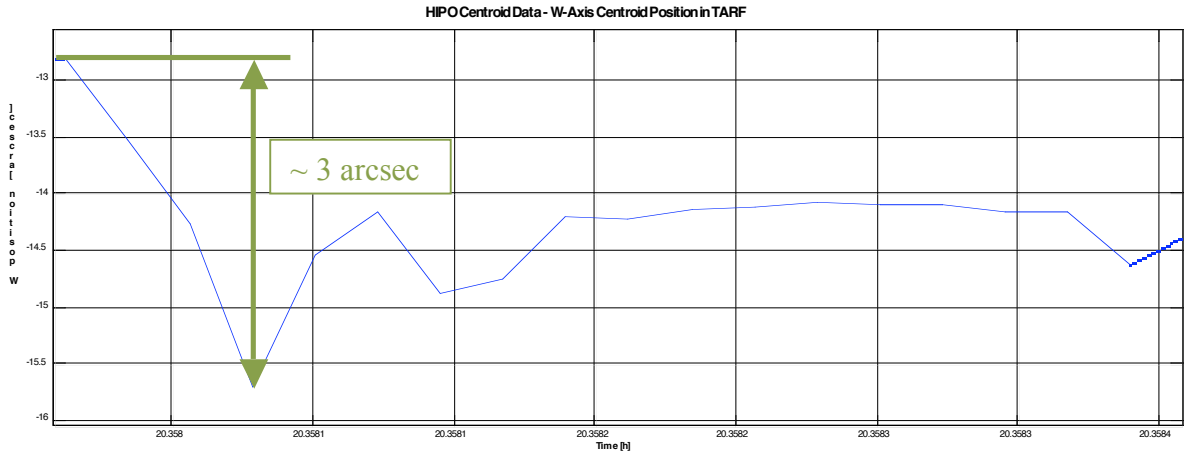

Figure 41

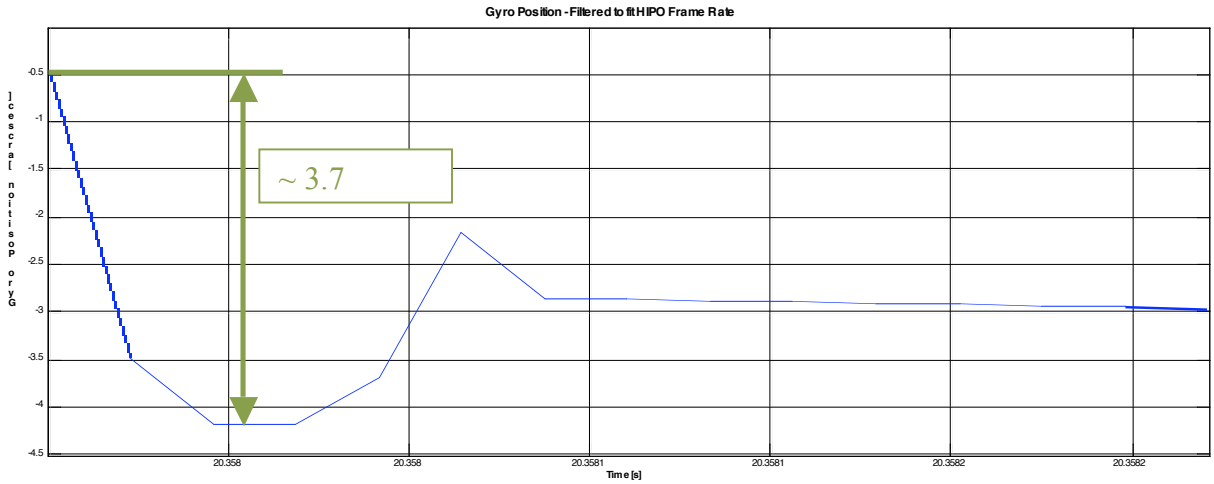

Figure 42

Next Steps:

1. The gyro behavior and the size of the delta rate jumps need to be analyzed in more detail by applying random signals with different amplitudes and also with smaller bandwidths to the Fine Drive. We should approximate the expected rigid body rotation of the TA during observation as much as possible in amplitude and bandwidth – since right now we are probably looking at a worst case scenario with a random signal of 400 Hz bandwidth and rapid changes in torques.

2. Changes to the handling of gyro warning flags in the ATCU software should be implemented and tested in the hangar.
3. The results from 1 and 2 should be combined and it should be verified during a night time line operation that the image jumps were eliminated.
4. Get a detailed explanation from IXSEA about what causes the gyros to set warning flags. On which values are those flags based? What are the thresholds?

TC-HIPO-08 Part 4: Nod Settling Time

Introduction:

This part of the HIPO 08 tests is the only one that aims on verifying a performance criterion from SOF – 1011. The following paragraph quotes section 3.5.8 of SOF-1011, Rev. 7:

"The TA shall be capable of nodding operation with amplitudes from 0 to ≥ 20 arcminutes p-p in any direction. **Settling time to a stability of ≤ 1.0% of the nod amplitude shall be ≤ 2.0 seconds for a ≤5.0 arcminute nod**. For larger nod amplitudes, settling time to a stability of ≤1% of nod amplitude shall be ≤ (0.4 x amplitude in arcminutes) seconds, within the FOV limits of the tracker imager in use. The TA shall be capable of performing nod maneuvers with times between initiations of nod commands as short as the required settling times associated with the respective nod amplitudes. This shall not preclude nod motions to be commandable more frequently for system setup. However, the TA will not be expected to meet the specific nodding requirements herein when these commands are imposed prior to the end of the first imager-based tracking subsystem update following TA settling to the 1% of nod amplitude error band. Nod performance shall be possible at the tracking stellar magnitude limit specified for the imager which is providing the tracking error signals. For image stability determination purposes, measurement shall be initiated at the end of the first imager-based tracking subsystem update following TA settling to the 1% error band, and continued for at least one hour or until the onset of the next nod (this nod onset occurring no sooner than the second imager-based tracking subsystem update), whichever occurs first."

This test measures the settling time of the TA by observing the image trajectory as nod motions of various distances are executed under tracker control. Images will be obtained at 5 Hz, substantially faster than the 2-4 second settling time requirement.

As we prepared to do this test it was clear that the exact TA commands used to execute a nod would affect the settling time. It also became clear that the nod settling time that really matters for early science is the time between generation of a nod command to the MCCS and when the TA is stable so data acquisition can commence. There is no way that we could simulate that and time was short so we decided to use repeated move-to-boresight commands to effect the equivalent of a nod rather than the much more complex TRC_NOD_EXECUTE command envisioned in the test plan.

Procedure:

1) Move a star to the FPI boresight.
2) Start a 4 arcmin / 5Hz chopping in XEL with the TCM (2 "stars" will appear on the FPI).
3) Define two AOIs containing these stars.
4) Execute multiple moves to boresight commands (TRC_MTBS_CENTROID) and take turns in moving AOI 1 and AOI 2 to boresight. This corresponds to a 4 arcmin nodding.
5) Take images with HIPO, frame rate 5 Hz, 3x3 binning

Figures 43 and 44 below show the RSS of the centroid deviation from boresight in pixels. Each nod leads temprorarily to a large deviation, and we define the nod settling time as the time period where the centroid is more than 1% of the nodding amplitude away from boresight. 1% of the commanded 4 arcmin nod amplitude is 2.4 arcsec, and taking 3x3 binned images (0.975 arcsec/pixel) this corresponds to 2.5 pixels. So, the threshold we are looking for is 2.5 pixels, which is marked with a dashed grey line in the plots. A nod fulfills the SOF-1011 requirement when the settling time is within a 2 second window (dashed rectangles) – in fact, the settling time we are measuring must be significantly smaller since it does not include any additional overhead added by MCCS. Nods that are well within specification are marked green, those close to 2 sec are marked brown, and the once that violate SOF-1011 are marked red.

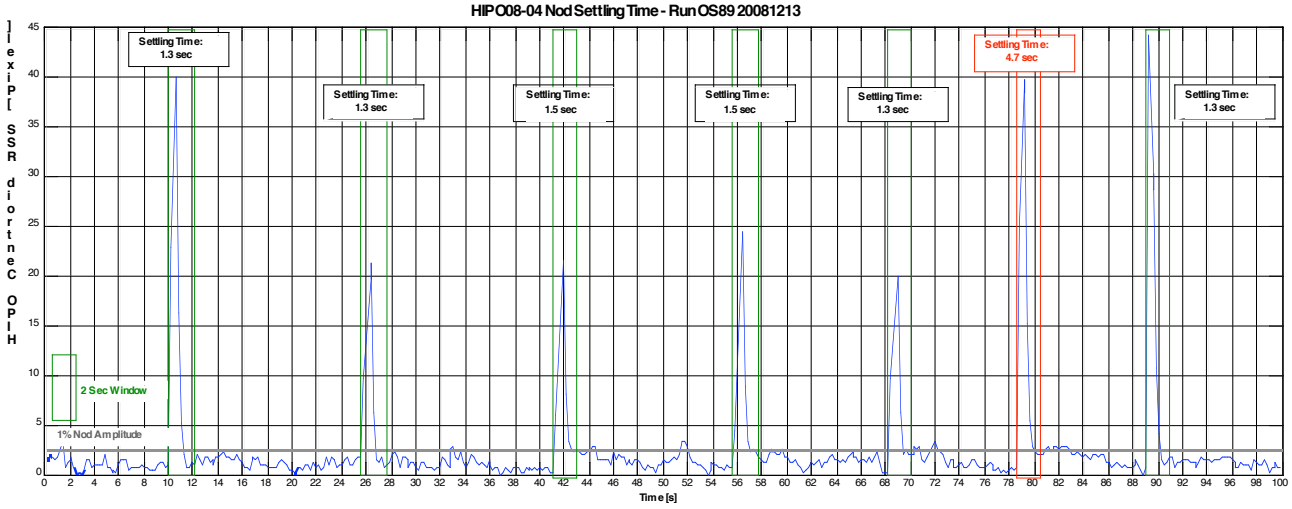

Figure 43

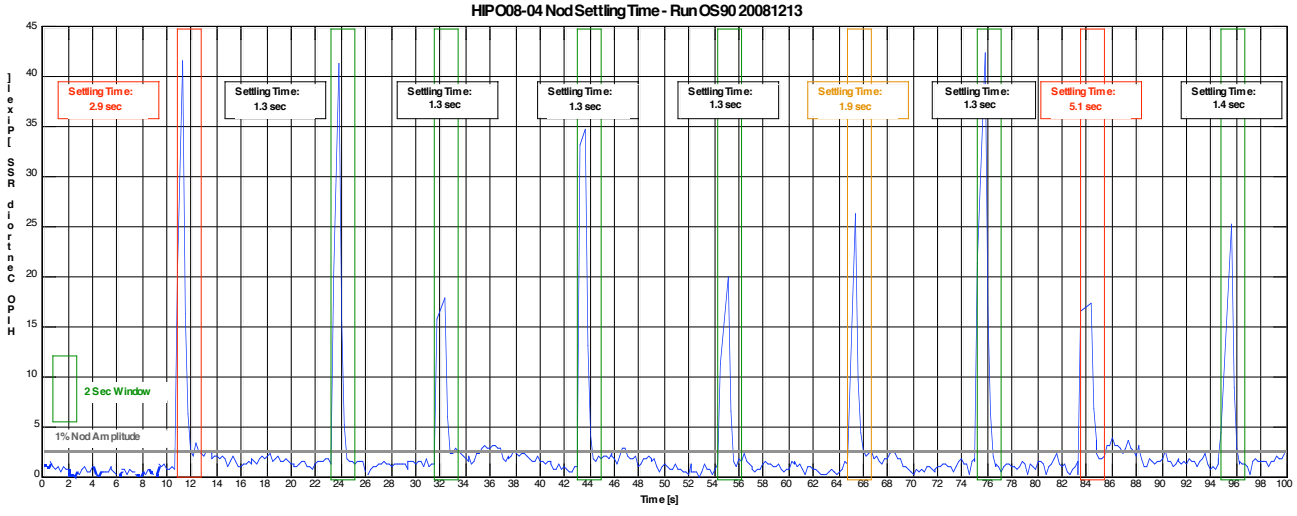

Figure 44

Discussion

Most of the nods are within specification and in nine out of 16 cases the settling time is 1.3 sec (see also table 1). The rest of the values are higher, but only four are larger than 2 sec. Image quality is heavily affected by seeing during ground operations, and this could be one explanation for the, in some cases, extremely long settling times.
Assuming that MCCS will add a couple hundred milliseconds, even the 1.3 sec nod settling time measured during this simplified test will bring us close to the 2 sec specified in SOF-1011.

Run	*Nod No.*	*Settling Time [s]*
OS 89	*1*	*1.3*
	2	*1.3*
	3	*1.5*
	4	*1.5*
	5	*1.3*
	6	*4.7*
	7	*1.3*
OS 90	*1*	*2.9*
	2	*1.3*
	3	*1.3*
	4	*1.3*
	5	*1.3*
	6	*1.9*
	7	*1.3*
	8	*5.1*
	9	*1.4*

Table 1

The conclusion is to keep an eye on the nod settling time. Improvements to the FD controller will reduce it a little bit, but if necessary we need to look into possibilities to minimize overheads by the tracker and the trajectory generator. Making a measurement using MCCS with the actual TRC_NOD_EXECUTE command is mandatory in order to get a full picture of the nod settling time.

Next Steps:

Redo this using the MCCS with FORCAST

TC-HIPO-09: TA Scanning

Introduction:

This test verifies the TA (but not MCCS) scanning functionality and assesses the astrometric performance of the scanning function at the level required by GREAT for Early Science. From the testing point of view the early science requirement can be broken into three parts: 1) scanning at rates from 2-20 arcsec/sec with 2" rms pointing error for durations of 40-100 seconds; 2) repositioning the telescope to repeat these scans as slightly displaced, parallel lines; and 3) scanning at 1-2 degrees/sec in elevation with position accuracy of one degree. HIPO can be used to test cases 1 and 2, but not case 3, which is better tested with the WFI or the TA attitude sensors.

Due to schedule pressure case 2 (offset parallel tracks) was not tested, the long exposure single frame part of the test, both unchopped and chopped, was skipped, and no tracking for gyro drift compensation was done once the scanning tests commenced.

The scans were set up by setting the TA so the images of HD5914 and BD+88°005 were placed at the center of the SI mounting flange in turn by moving the AOI for each star to the boresight of the FPI. The TA attitude quaternion (atc_q_att) for each position was then read out from the EGSE and the scan set up to scan from a starting location near HD5914 in the direction of BD+88°005 at the requested scan rate for 125 seconds. The starting location was corrected for the scan ramp-up, which was calculated by extrapolating the great circle to -2 seconds of scan time relative to the HD5914 position. The first two points defining the scan, 1 second apart, resulted in the TA crossing the nominal start position (HD5914) at the selected scan velocity at 2.00 seconds into the scan. No ramp-down was executed at the end of the scan.

Because of the empirical manner in which the scans were set up it is to be expected that the scan direction will not be exactly correct. This will be seen in the data as a linear deviation of the observed scan track on the sky compared to the desired track. Also, no tracking corrections were made during the entire test and therefore the absolute positions of the two stars are expected to differ slightly for each scan.

For completeness the adopted coordinates of these two stars are given in Table 9-1. Both of these stars, particularly BD+88 005, have significant proper motions.

Table 9-1: Adopted Great Circle Defining Star Coordinates
(J2000 Equinox, 2008.96 Epoch)

Star	RA	Dec
HD5914	1:33:52.9344 (23.47056)	+89:00:56.016 (89.01556)
BD +88° 005	1:38:21.2136 (24.58839)	+88:58:49.08 (88.98030)

Data Acquired:

The first fully successful scans were obtained on our last night on the sky, 14 December, 2008 UT. We obtained five scans as shown in Table 9-2. The HIPO images were all

2000 frame 4x4 binned basic occultation runs with 80 ms frame interval lasing 160 seconds. It is worth noting that there was a 3° LOS reset between OS 162 and OS 163.

Table 9-2: Scan Parameters

HIPO Observation Sequence	HIPO Observation Start time (UT)	Unix time (and UT) of TA scan start*	Scan Rate (“/sec)	Comments
161	11:09:47	30107400 (11:10:00)	2	
162	11:14:47	30107700 (11:15:00)	2	Repeat of OS161
163	11:20:07	30108020 (11:20:20)	5	3° LOS reset before this OS
164	11:25:17	30108330 (11:25:30)	10	
165	11:31:08	30108670 (11:31:10)	20	

* The old IRIG-B standard does not include a year in the time string so the TA systems use seconds since the beginning of the year. Unix time is normally seconds since the beginning of 1970, so effectively the TA thinks it is 1970. This is likely to cause a shift of one day since 2008 was a leap year and 1970 was not.

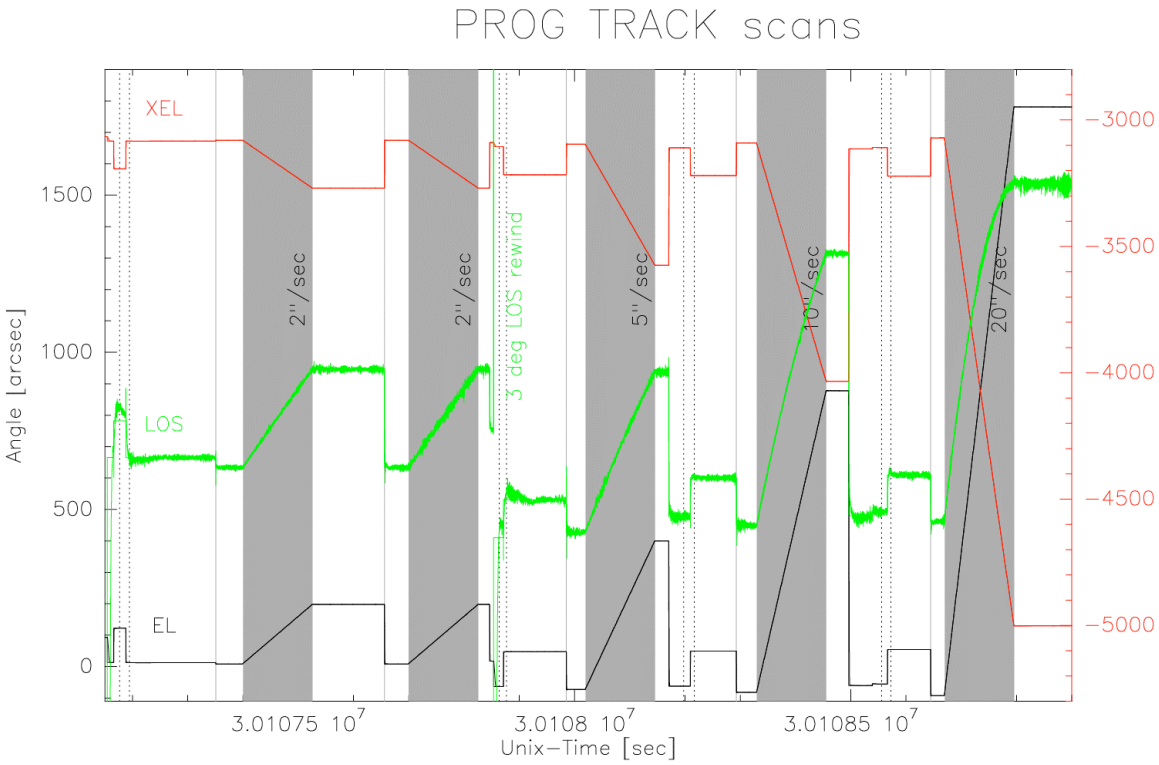

Figure 9-1: Gyro data showing the motion of the TA during the entire scanning test period encompassing HIPO OS161-165. The plot shows measured rotation angles of EL-axis (black), the XEL-axis (red), and the LOS-axis (green). The EL and XEL angular scales are denoted at the left and right side of the plot. The LOS data from before and after the rewind were combined into the same plot and are shown with a full angular scale of 7". The gray areas indicate the beginning and ending of a scan and are labeled with the respective scan rate.

On the TASCU side, 50 Hz housekeeping data were acquired. These data include the commanded and actual attitude quaternions. The scanning test was done with the improved FD controller settings. Figure 9-1 shows the commanded attitudes in all three axes for the entire scanning activity as a function of Unix time.

Data Analysis:

TASCU:

Figure 9-1 shows the commanded attitudes in EL, XEL, and LOS from the beginning to the end of the scanning test. In between two scans the TA was moved to HD5914 and BD+88°005 to acquire the actual quaternions and then placed at the initial scan position. This initial position was calculated to be on the Great Circle close to HD5914 and in the opposite direction from BD+88°005. The distance of the starting point from HD5914 was chosen to be 2 time seconds away in order to allow the telescope to ramp-up to the full scan rate. As the TASCU handles the first two positions and two last positions in a special way they are supposed to be used for the ramp-up and ramp-down phase of the scan. Therefore, the telescope may start and end slightly off-track to satisfy the constraints of the maximum rate and acceleration. Another 0.5 seconds was added internally by the TASCU interpolation code. This just means that the TA starts slightly earlier than commanded with a start offset that is adjusted accordingly. With the chosen time distance of 1 second per position the TA starts moving at -0.5 seconds and passes the first position roughly at the commanded start time and finished the ramp-up after +1 seconds. Between seconds +1 and +2 the TA is expected to stay at the commanded rate and it passes the actual starting point (the position of HD5914) at a constant rate at 2.00 seconds into the scan. Because no special ramp-down at the end of the scan was commanded the TA is expected to stop the scan close to the last position of the track program. The move will come to a stop 0.5 seconds after the last position in the program.

Table 9-3 shows details of the five scans. The first two scans, corresponding to HIPO OS161 and 162, were done with the same quaternions. The TA was set up on the two stars as described above for OS161 but no star setup was done for OS162. The result is that accumulated gyro drift over the 300 second between the start times of the two scans produced an offset in the starting position of the second scan.

The gyro drift rate can be determined by looking at the accumulated gyro drift noted in the last block of data for OS163 through OS165. The zero point for this was the position of each star for OS161. There is no gyro drift data for OS162 because no setup on the stars was done. The average drift rate is 0.011”/s ± 0.001”/sec. For completeness, the gyro drift rate corrections in place in the TASCU during the scanning tests were based upon previous tests results.

The actual great circle distance between the two stars is 145.13 arcsec. The “Distance between positions” value in Table 9-3 is the separation measured by the TA by differencing the quaternions derived from after carrying out the Move-To-Boresight command for each star. The differences between this empirically derived separation and the correct value derived from the positions given in Table 9.1 are given in Table 9-3.

Table 9-3: Quaternions Parameters

HIPO OS	Description	Data
161	Time / Quaternion HD5914	30107194.8441 2.81118765090428E-05 -0.00703784377502076 0.562558311025267 0.826727654467371
	Time / Quaternion BD +88° 005	30107176.8449 0.000278118540908571 -0.00728809617484111 0.562559192350246 0.826724840201661
	Distance between positions	145.9". Error (O-C) = +0.8”
	TA commands first move	30107399.5160
	TA commands last move	30107525.4909
	Relative gyro drift (sum)	0/0 (reference point)
162	Time / Quaternion HD5914	The same quaternions used in OS161were used here.
	Time / Quaternion BD +88° 005	The same quaternions used in OS161were used here.
	Distance between positions	The same quaternions used in OS161were used here.
	TA commands first move	30107699.5040
	TA commands last move	30107825.4989
	Relative gyro drift	NA. No star setup was done for OS162.
163	Time / Quaternion HD5914	30107863.8174 -0.000144194627084473 -0.00704848648396117 0.584007726687247 0.811717483620865
	Time / Quaternion BD +88° 005	30107876.8169 0.000106159085208664 -0.00730192945545984 0.584008196579083 0.811714911089432
	Distance between positions	147.0'". Error (O-C) =+1.9”.
	TA commands first move	30108019.5112
	TA commands last move	30108145.4861
	Relative gyro drift (sum)	7.09" for HD5914 after 669s 8.66" for BD +88° 005 after 700s
164	Time / Quaternion HD5914	30108197.8040 -0.000142558217329859 -0.00705894543235591 0.58400792820806 0.811717248034479
	Time BD +88° 005	30108216.8033 0.00011125245800511 -0.00730834375733921 0.584008370822611 0.811714727317137
	Distance between positions	146.8'". Error (O-C) = +1.7.”.
	TA commands first move	30108329.4988
	TA commands last move	30108455.4937
	Relative gyro drift (sum)	10.96" for HD5914 after 1003s 11.79" for BD +88° 005 after 1040s
165	Time / Quaternion HD5914	30108555.7897 -1.264972539538342E-4 -7.056447418595956E-3 5.840081334625453E-1 8.117171247410437E-1
	Time / Quaternion BD +88° 005	30108572.7890 0.000123521859250565 -0.00731420463763535 0.584008497022805 0.811714581954786
	Distance between positions	148.1'". Error (O-C) = +3.0”.
	TA commands first move	30108669.5052
	TA commands last move	30108795.5001
	Relative gyro drift (sum)	14.83" for HD5914 after 1361s 17.37" for BD +88° 005 after 1396s

Problems:

The setup of the scan was done by using the atc_q_att HK-parameter. This method caused two issues:

1. atc_q_att shows the real time attitudes and during the test the EGSE received an updated quaternion every second. However, it is unknown when the quaternions for the two positions were copied to the program setup tool. In order to verify the desired positions calculated by the TASCU the two quaternions were restored in a maximum likelihood analysis where all possible pairs of quaternions were compared with the desired quaternion from TASCU. The solution is listed in Table 9-3.
2. The setup tool did not keep the LOS-axis constant but instead interpolated/extrapolated this axis as was done with the EL and XEL axes. Therefore a small LOS component is visible in all scans and is most prominent in the faster scans because of the larger extrapolation.

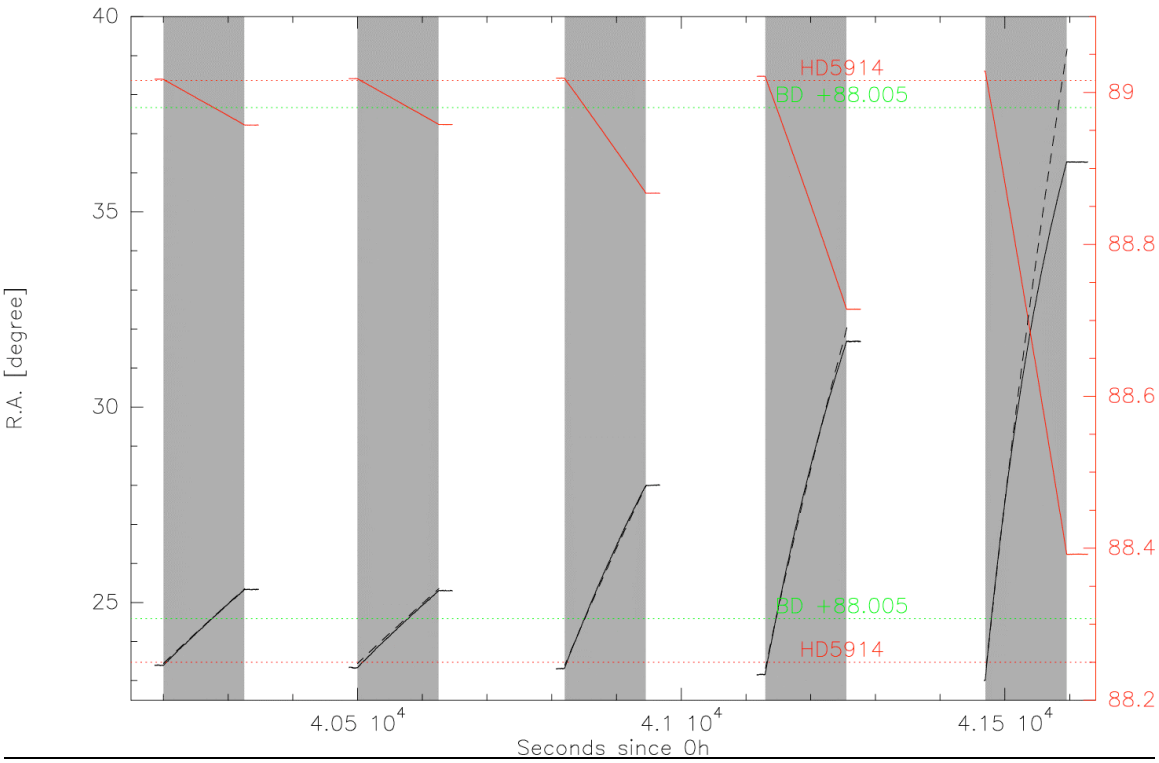

Figure 9-2: Overview showing the RA/Dec position of the SI mounting flange as measured by HIPO. The positions of HD5914 and BD +88° 005 are indicated in red and green. The dashed curves show the desired trajectory. The large deviations seen especially in the RA for the last (20”/s) scan are due to two factors: 1) no account has been taken for the error in the pole of the great circle of the scan, which is derived empirically, and 2) the proximity of the scan to the celestial pole results in very large RA errors for small great circle errors. The detailed scan comparisons done later are in the great circle coordinate system, which makes the comparison more straightforward.

HIPO:

In broad overview, the analysis of a HIPO occultation run was to find stars in each frame, match them with catalog positions, fit a plate solution to each frame, and then derive the RA and Dec of the position of the center of the SI mounting flange for that frame. These positions were then transformed into the coordinate system of the desired great circle (GC) scan trajectory. Finally, deviations along, and perpendicular to, the GC were found.

The catalog used for the plate solution was based on the USNO B1.0 catalog (Monet, et al., 2003), obtained from the Vizier service of the SIMBAD database, operated by CDS in Strasbourg, France. The final star positions were at equinox J2000, epoch 2008.96.

The process used is outlined in more detail below:

1. For each frame, estimate the position of the plate center and its orientation.
2. Subtract a bias frame derived from a median filter of the occultation run
3. Find and centroid on all the targets in the frame to produce an X/Y position list
4. Project the catalog onto the tangent plane using the estimated plate position and orientation from step 1 to produce a catalog X/Y position list.
5. Correlate the target list with the catalog list. This produces an X/Y offset correction, a small rotation correction, and a list of matched coordinates. If this process fails, manual intervention is required.
6. Perform a least squares fit between the catalog and target positions to determine the plate scale, rotation, and coordinates of the center of the flange.
7. Transform the RA/Dec trajectory of the center of the TA flange to GC "latitude" (perpendicular to the great circle) and "longitude" (along the great circle). The nominal zero point of the scan is the position of HD5914, and the scan direction is determined by the position of BD +88° 005, with both positions being defined in Table 9-1. A GC relative longitude is also found based on the time at which the scan passed the position of HD5914 and rate of the scan. It is the difference between the observed GC longitude and the desired GC longitude.

The correlation and plate fitting processes needed to be iterated with manual editing of some frames in order to reach the goal of 90% success. Eventually all the scans had fit success rates of 95-99% with no long gaps in the scans. One of the most problematic factors was the presence of ghost reflections from bright nearby stars.

To the degree that the great circle scan is imperfectly set up there will be a trend in the GC latitude, and a much smaller trend in relative longitude, through the scan. Gyro drift will also result in linear trends in latitude and relative longitude. Some glitches should be expected due to residual badly fitted frames and also some lumpiness due to the fact that different frames are fit to different catalog stars (all of which have imperfect positions). In addition seeing will produce noise in the HIPO determination of the scan position.

The final output of the reduction process is a table and corresponding set of plots of RA, Dec, rotation angle, GC latitude, longitude, and relative longitude as a function of time along the scan. The assessment of the performance of the scan is done by fitting and subtracting a linear trend to the GC latitude and relative longitude and finding the rms of these values. As a side effect the HIPO image scale is also well determined.

Results:

TASCU:

The TASCU analysis consists of comparing the commanded and actual attitude quaternions. The following series of plots in Figure 9-3 show the angular differences in EL, XEL, and LOS between these two quaternions.

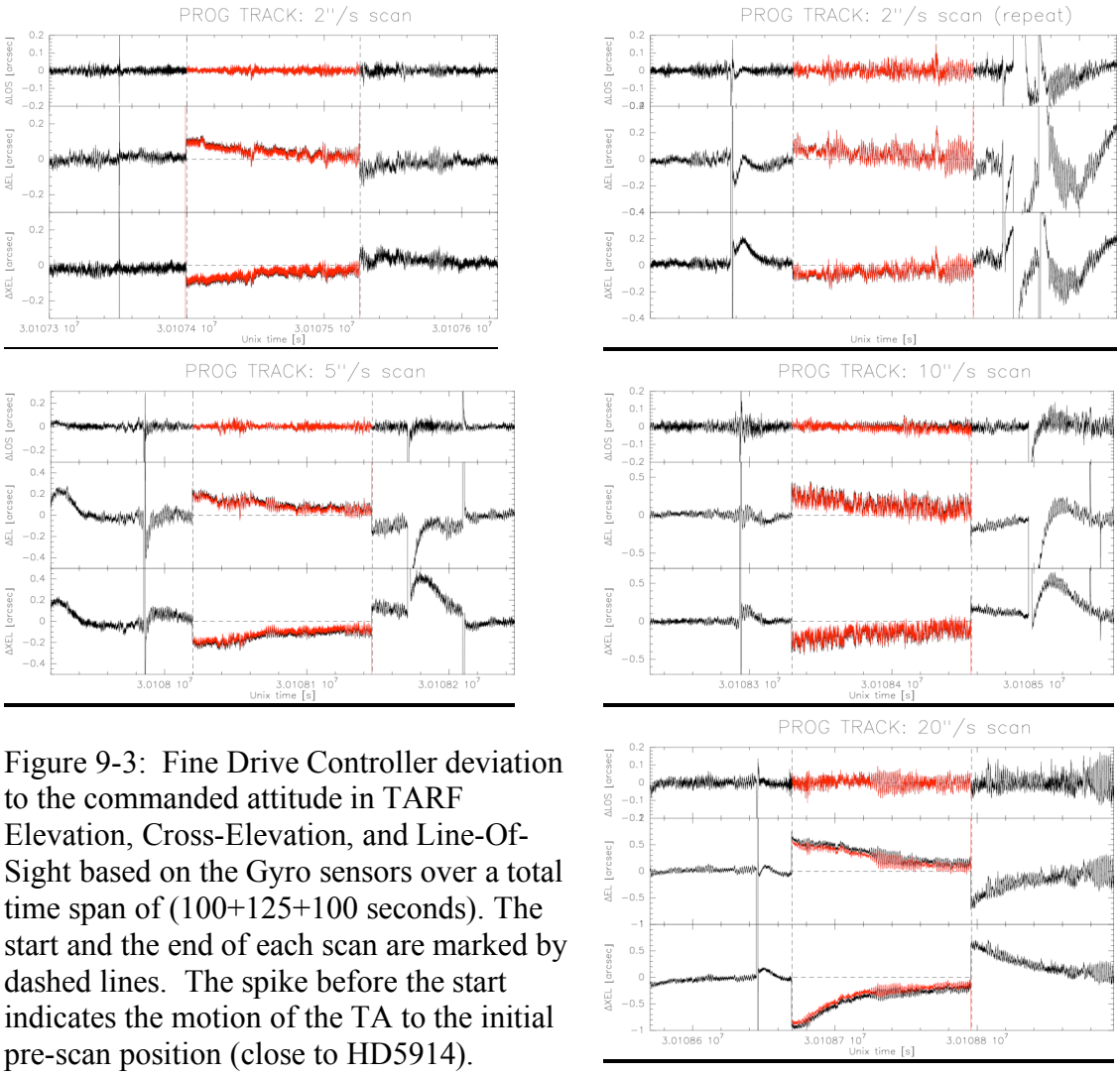

Figure 9-3: Fine Drive Controller deviation to the commanded attitude in TARF Elevation, Cross-Elevation, and Line-Of-Sight based on the Gyro sensors over a total time span of (100+125+100 seconds). The start and the end of each scan are marked by dashed lines. The spike before the start indicates the motion of the TA to the initial pre-scan position (close to HD5914).

Each scan was commanded from the second star BD+88°005 which typically happened 10-20 seconds before the starttime. In red the plot also shows the offset that the telescope had with respect to the pre-calculated program. The difference between this offset and the actual control deviation is negligible small (5 ms) and indicates the correct implementation of the timing within TASCU.

The gyro data indicate a bias in the scan position of 0.4” or less toward the end of a scan. This behavior was expected from previous tests and is due to slow fine drive settling

when the TA is close to the commanded attitude (less than ±1”). No additional scanning-related lag was observed in the gyro data. The deviation between desired attitude and the position in the program was 5ms. This difference is negligible small (cf. offset between red and black curves in Figure 9-3). The pointing error due to control deviation seen in the gyro data was always below the required 2” rms limit. Note that the pointing error within a scan is comparable to the pointing error when the telescope is not scanning.

A few informational points should be noted for reference in case this scanning procedure is used again. The fine drive maximum rate was 1 degree/sec. With this rate and its associated acceleration the 1 sec ramp-up period is far longer than the TA needs for the scan rates used. From the HIPO data the actual acceleration time is on the order of 15 ms. The 125 second scan was made up of Program Track points separated by 1 second. These quaternions were transferred by four successive PROG_TRACK commands with the same ID. Because of a current MCP limitation the processing time for each command is about 1 second so it is recommended not to stack up too many of these commands to keep the upload time from being excessive. The second 2”/sec scan (OS162) was initiated by supplying a new time stamp with the PROG_TRACK_CONTROL command, demonstrating that a program already executed can be reused.

HIPO:

Typical HIPO scan analysis plots are shown in Figure 9-4. The GC latitude has a relatively large slope due to the setup inaccuracies outlined earlier. This slope is proportional to the sine of the GC pole error. The longitude depends on the cosine of the GC pole error so it is less affected by setup errors. No evidence of an error in start time of the scan is evident. For example, at the 10”/s rate of the scan seen in OS164 an error of a single 80ms frame would be 0.8”, resulting in a deviation from the overall scan behavior of almost one major division in the GC relative longitude plot in the lower right frame of Figure 9-4. The rotation angle has relatively high noise due to the sparseness of the star field.

The overall results of the HIPO analysis are presented in Table 9-4. The first four columns contain the same information as in Table 9-2. Note that the scan start time is 2.00 seconds before the time at which the TA moves through the position of HD5914 at the requested velocity. The TA actually starts the motion 0.5 seconds earlier than this from an extrapolated offset point. The Time Offset column is the scan start time minus the HIPO start time. The time difference between the HIPO start time and the time at which the scan passes HD5914 would be 2.00 seconds larger than the Time Offset column values. The next three columns are the derivative of the GC latitude with time, GC latitude with GC longitude (this is the GC pole error in radians), and GC relative longitude with time. The next two columns are the GC latitude and longitude of the scan at the time the scan passes the location of HD5914. Next we find columns for the rms deviation of the scan from the linear fits alluded to earlier, in GC latitude and relative longitude. The final column, labeled “Setup error”, is the relative GC latitude error occurring during the scan setup process that would result in the observed dlat/dlong value. The setup error is equal to the observed dlat/dlong value multiplied by the angular separation of the two setup stars, 145.13”. Part of the dlat/dlong value is due to gyro drift and control devation so the setup error values are approximate – depending on the sign of

the other factors relative to the actual setup error the values could be larger or smaller. The fact that the values in columns 6, 7, 9, and 10 have the same sign for all scans presumably reflects some systematic offset related to the scan setup process followed.

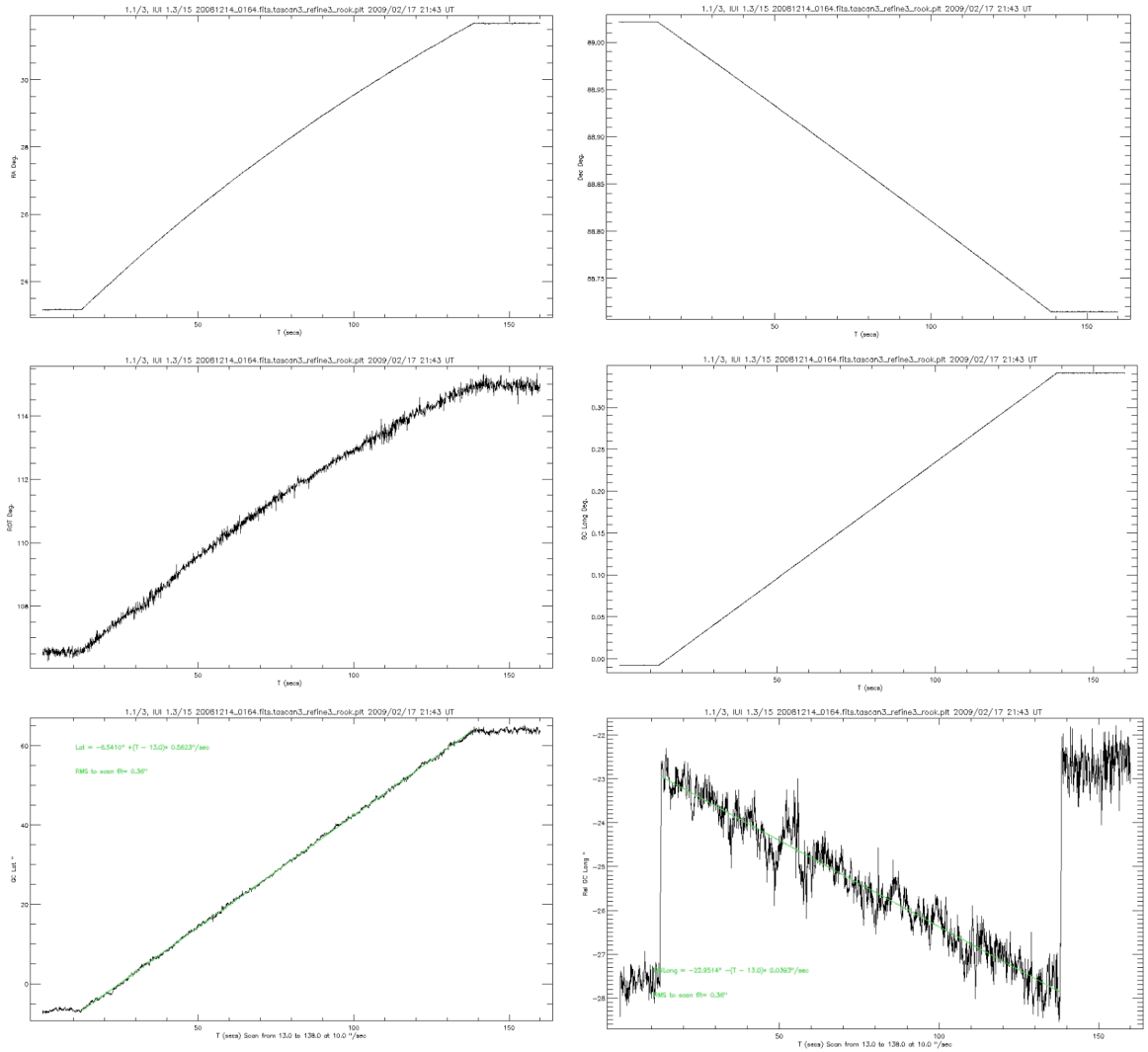

Figure 9-4: HIPO scanning analysis plots for OS164, the 10”/s scan. The upper two plots are RA (left) and Dec (right) tracks of the location of the center of the SI mounting flange. The center row shows rotation angle (left) and GC longitude (right). The bottom row shows the GC latitude (left) and relative longitude (right).

Table 9-4: HIPO Scan Analysis Results

HIPO OS	Rate "/s	UTCSTART	UTC (sec) since 0h UT	Scan Start since 0h 1/1	Time Offset	dlat/dT ("/s)	dlat/dlong (rad)	dlong/dT ("/s)	Lat(0) (")	Long(0) (")	Lat rms (")	Long rms (")	Setup error (")
161	2	11:09:47	40187	30107400	13	0.036	0.018	-0.019	-1.0	-3.3	0.34	0.35	2.6
162	2	11:14:47	40487	30107700	13	0.044	0.022	-0.013	-2.5	-7.2	0.35	0.32	3.2
163	5	11:20:07	40807	30108020	13	0.209	0.042	-0.023	-2.4	-2.7	0.41	0.39	6.1
164	10	11:25:17	41117	30108330	13	0.562	0.056	-0.039	-5.4	-2.2	0.36	0.36	8.2
165	20	11:31:08	41468	30108670	2	0.650	0.033	-0.052	-1.0	-3.0	0.51	0.40	4.7

It is interesting to note that the difference between the Lat(0) and Long(0) values for OS161 and 162, which should be due to gyro drift over the 300 sec interval between the scan start times, corresponds to a gyro drift value of 0.014”/s. The ~2” uncertainty in the setup positions corresponds to a drift rate uncertainty of 2/300 = 0.007 ”/sec, so this value is in good agreement with the better determined value of 0.011 ”/s presented in the context of Table 9-3 earlier.

This suggests that a correction to the Lat(0) and Long(0) values could be made by factoring in the gyro drift accumulated between the time the last star was set up on and the time the scan crossed the position of HD5914. For the purpose of this investigation we assume that the ratio of the latitude drift to the longitude drift is in the ratio of the drifts seen between the Lat(0) and Long(0) values for OS161 and 162, but with the drift values scaled to match the well-determined 0.011”/s total drift rate. This corresponds to a latitude drift rate of -0.004”/s and a longitude drift rate of -0.010”/s.

Table 9-5 shows the result of this investigation. The “Star time” column contains the least significant digits of the latest time of a star setup quaternion given in Table 9-3, the “Scan time” is the same for the first TA move time in Table 9-3, but with 2.5 sec added to correspond to the time the scan passes HD5914, the two drift columns are the accumulated drift at the rates just defined, the Lat(0) and Long(0) columns are copied from Table 9-4, and the last two columns are the differences of Lat(0)-Lat drift and Lon(0)-Lon drift, i.e. drift corrected Lat(0) and Long(0) values. Clearly the bulk of the offsets seen in the Lat(0) and Lon(0) values in Table 9-4 are due to gyro drift. The only scan that shows an excessive corrected offset at the HD5914 position is the OS164 (10”/s) scan with a 5” corrected Lat(0) value. All the others are between -2” and zero. The fact that they are still all negative suggests a systematic effect, perhaps controller deviation, is at work.

Table 9-5: Correction of Scan Initial Positions for Gyro Drift

OS	Star Time	Scan Time	Delta Time (s)	Lat. Drift	Long Drift	Lat(0) (")	Long(0) (")	Lat(0) - Lat Drift	Lon(0)-Lon Drift
161	7176.8	7402	225.2	-0.9	-2.3	-1.0	-3.3	-0.1	-1.0
162	7176.8	7702	525.2	-2.1	-5.3	-2.5	-7.2	-0.4	-1.9
163	7876.8	8022	145.2	-0.6	-1.5	-2.4	-2.7	-1.8	-1.2
164	8216.8	8332	115.2	-0.5	-1.2	-5.4	-2.2	-5.0	-1.1
165	8572.8	8672	99.2	-0.4	-1.0	-1.0	-3.0	-0.6	-2.0

The drift in GC latitude with time (dlat/dT in Table 9-4) is mainly due to the error in the GC pole due to setup errors. The 0.011”/s gyro drift and control deviation shown in Figure 9-3 are small additional contributors. The drift in relative longitude is partially gyro drift, partially control deviation, and partially the term proportional to the cosine of the GC pole error. The effects of the pole error and gyro drift are shown in Table 9-6. For the slower scans the pole error is not significant but it is comparable to the gyro drift for the faster scans. Column 5 of Table 9-6 is the dlong/dT value due to GC pole error and column 6 is this value with the -0.010”/s longitude gyro drift component discussed above added. The observed dlong/dT value is copied in from Table 9-4 and the remaining dlong/dT value is given in the final column. Examination of Figure 9-3 indicates that the slope in the control deviation is comparable to the pole error effect. We

have not projected the control deviation into the GC latitude/longitude coordinate system to see if the residual drift is fully explained by this. We leave this topic at present with the conclusion that the observed relative longitude drift is reasonably consistent with the GC pole error cosine effect, gyro drift, and control deviation.

Table 9-6: GC Pole Error and Gyro Drift Effect on Relative Longitude Drift

OS	GC Pole Error (PE; rad)	1-cos(PE)	Scan rate ("/s)	dlong/dT due to PE	PE effect + Gyro drift	Observed dlong/dT	Residual dlong/dT
161	0.018	0.00016	2	0.000	-0.010	-0.019	-0.009
162	0.022	0.00024	2	0.000	-0.010	-0.013	-0.003
163	0.042	0.00087	5	-0.004	-0.014	-0.023	-0.009
164	0.056	0.00158	10	-0.016	-0.026	-0.039	-0.013
165	0.033	0.00053	20	-0.011	-0.021	-0.052	-0.032

The rms deviations from the linear fits to GC latitude and relative longitude (columns 12 and 13 of Table 9-4) are very small compared to the Early Science requirement of 2". However, this is with a linear fit being made to the relative longitude, and the residual dlong/dT value seen in the last column of Table 9-6 for the 20"/s scan will result in an in-track error exceeding 2" across the 125 second duration of the scan.

The HIPO image scale derived from the scans is 0.3264 arcseconds per pixel (unbinned). This value is very close to the 0.327 "/pixel value measured in Waco in 2004 with the aluminum secondary mirror. There is a systematic difference between the horizontal and vertical scales of 0.04% that is probably due to keystone distortion in the HIPO red camera lens.

Conclusions:

1. The TA followed remarkably well the commanded track. The functional performance of the TSC_FD_PROG_TRACK and TSC_FD_PROG_TRACK_CONTROL commands are fully sufficient to handle the scanning requirements anticipated by GREAT. The approach for setting up the scans was sufficient to demonstrate the scanning functionality of the TA. The degree to which this could be tested was limited by gyro drift and the empirical nature of the definition of the scan's great circle pole position.
2. With the used maximum Fine Drive rate (initial rate of 1 deg/sec) and the derived FD acceleration (not settable), the ramp-up time window of 2 second was by far more than what would have been needed to get the TA accelerated to the scanning rate. In order to keep the ramp-up time short and the ramp-up points close to the start position, two neighboring points in the track program had a time separation of 1 time second. Because of the constant velocity assumption the scan resulted in a track length of 125sec*rate arcseconds. A scheme close to the one exercised during this test is suggested for Early Science scanning. A recommendation about how to setup a scan has been generated for the MCCS and SI software developers.
3. The absolute quaternion program consisted of 3*40+5=125 points and was transferred by four subsequent PROG_TRACK commands, all with the same program ID. Because a PROG_TRACK command needs at least 5 quaternions,

the program length had been slightly adjusted from before 122 positions. Otherwise the last command would have been rejected. Because of a current limitation within the MCP the response time for each PROG_TRACK command is about 1 second. It is recommended not to stack up too many of these commands or the upload of the whole program will become very inefficient.

4. The repeated 2 "/sec scan demonstrated that an already executed program can be reused if a new timestamp is supplied with the PROG_TRACK_CONTROL command.
5. The pointing error stayed generally below the required 2" rms limit. The 10”/s scan had a latitude offset in excess of this value, and the 20”/s scan’s residual dlong/dT value resulted in an in-track error in excess of this value. This is assumed to be due to the relatively large control deviation at the higher scan rates that is being worked on at present. Within the tested scan rates the pointing error was not significantly increased by the scanning mode. An in-flight pointing performance test could possibly be done without explicitly testing scanning.
6. The small offset between program and actual telescope position is indicating, when ignoring the always present control deviation, that the telescope is running ahead by not more than 5 milliseconds. Within the rates tested here it was not possible to verify this anti-lag with HIPO, which is good, because it will then be not an issue for Early Science either. However, considering that the control deviation can cause a lag of up to 1" it is advisable to subscribe to HK data of the commanded and the actual TA attitude and correct the offset offline.
7. The HIPO rms deviation from the linear fits to the great circle latitude and relative longitude was less than 0.5 arcsecond, well within the 2 arcsecond Early Science requirement.
8. The HIPO image scale is 0.3264±0.0001 “/pixel (unbinned).
9. A slow convergence has been identified as a minor issue when getting close to the settling point. This behavior is unrelated to the scanning test and discussed elsewhere.
10. Based on this test the maximum bias or lag was always below 7% of the commanded rate. Because most of the deviations were contributed from the settling issues of the FD controller the lag is probably much less. However, with the assumption of a linear relation the maximum anticipated error at 1deg/sec would be less than about 4' and sufficient for GREAT to measure the airmass. Note that no coupling between FD and CD is considered in this assumption. Also vignetting by the Aperture Assembly may be an issue.

Next Steps:

1. It will be much easier to meet the 2" rms pointing error Early Science requirement on the ground than in flight. It would be highly desirable to find a way to verify this in flight using FORCAST or a TA imager.
2. It may be desirable during a future test to acquire the necessary gyro data during the test to allow inter-comparison of the desired scan, the scan as indicated by the TASCU, and the observed optical track of the scan. The necessary gyro data were not collected during this test.
3. Future scanning tests should be formulated with an eye toward keeping track of the gyro drift, pole error, and control deviation.

TC-HIPO-10: Verification of Flexible Body Compensation (FBC) implementation

Introduction:

This test is a rough verification of the FBC implementation by means of static flexure. The implementation should be tested in regard to the quasi-static FBC coefficients. The basic approach is to measure the location of the LOS axis turning point as a function of elevation angle with the FBC active and inactive to see if the turning point stays fixed (within the error of the procedure).

There are six possible FBC coefficients. Previous studies suggest using only two coefficients for the feed forward FBC filter design [1]. This test procedure can verify and quantitatively assess only one of these FBC coefficients.

Current FBC implementation and filter design:

This section provides an overview of the current FBC implementation and the expected theoretical results.

FBC corrections are calculated based on ray trace equations and FE model calculations [2]. The predicted image motion is described by two angles ϕ_V and ϕ_W, which correspond to a negative telescope rotation about the u-axis (-ΔEL), respectively to a negative rotation about the v-axis (-ΔXEL). The image motion depends on the acceleration acting on the structure. There are in total six FBC coefficients that are used to calculate the image motion: One for each acceleration component per image motion direction. The image motion is given by:

$$\phi_V \ [arcsec] = \frac{0.455}{g}(a_{el} - a_{el,0}) + \frac{-2.107}{g}(a_{xel} - a_{xel,0}) + \frac{0.612}{g}(a_{los} - a_{los,0}) \quad (10\text{-}1)$$

$$\phi_W \ [arcsec] = \frac{8.594}{g}(a_{el} - a_{el,0}) + \frac{-0.061}{g}(a_{xel} - a_{xel,0}) + \frac{-69.902}{g}(a_{los} - a_{los,0}) \quad (10\text{-}2)$$

The three measured accelerations a_{el}, a_{xel} and a_{los} are referring to the reference acceleration vector [$a_{el,0}$ $a_{xel,0}$ $a_{los,0}$] measured during the gyro alignment at about 35° centered in the operational elevation range. The gravitational constant is $g = 9.81$ m/s^2.

In first order, the image motion in EL-direction can be neglected. Most image motion takes place in XEL. The acceleration acting in the LOS-direction contributes the most but also the acceleration acting in the EL-direction is not negligible. The according two FBC coefficients are the coefficients of interest for FBC tuning.

The image motion in the head ring imagers can be predicted using solely the FE model as ray tracing is not necessary. The according equations for the image motion are given in [3]. These results can be combined to predict the test results for the centroid position in

the imagers and HIPO over the elevation range. The predicted image motion for the two head ring imagers and the gyro LOS axis (turning points measured with HIPO) with respect to the focal plane is shown in Figure 10-1.

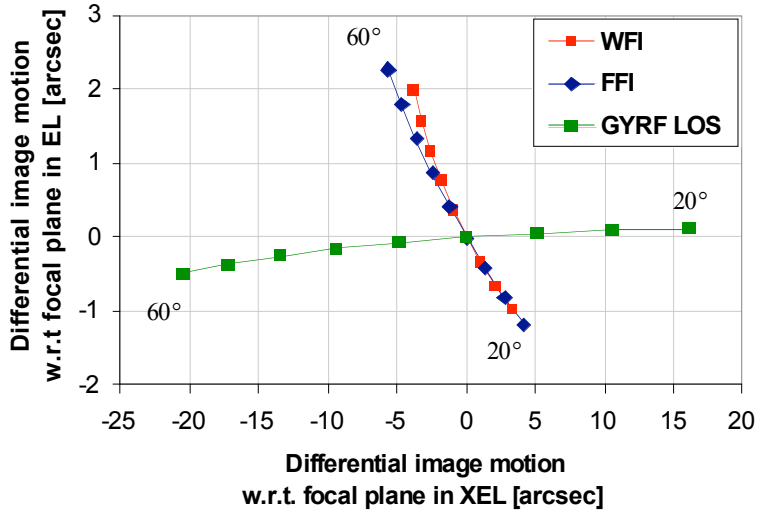

Figure 10-1. Projection of the gyroscope LOS axis (turning points) with respect to the focal plane. As well the differential image motion between FFI and WFI with respect to the focal plane. The alignment is performed at 35° where all boresight positions coincide.

The quasi-static FBC correction is applied within the FD loop. The corrections are calculated as quaternion from simultaneous rotation angles in EL and XEL:

$$q_{TARF,GYRF} = quatFromSimRot\begin{pmatrix}\phi_V\\ \phi_W\\ 0\end{pmatrix} \quad (10\text{-}3)$$

This FBC correction quaternion is then added to the telescope attitude (based on the gyro measurements):

$$q_{TARF,IRF} = q_{GYRF,IRF} \cdot q_{TARF,GYRF} \quad (10\text{-}4)$$

The accelerometer data are low-pass filtered by means of a chain of filters. The 400 Hz data are first averaged over the last four samples. Then the signal is further processed by a PT2 filter with a time constant equivalent to 0.48 Hz and a damping factor of 0.7. The Imager displacement correction on the other hand is filtered by the same PT2 filter but with a time constant of 3 Hz. Due to a software error the filter for the first case was applied twice and this resulted in an effective up-sampling of the input signal by a factor of two. The filter time constants are not optimized for flight conditions.

Data Acquired:

The data for this test were obtained on 13 December, 2008 (UT). For each Coarse Drive elevation angle and each FBC setting (ON and OFF), a sequence of six LOS rotations is performed. The rotation angle was reduced to 3.75° (compared to 4° for TC-HIPO-06) to avoid the LOS motion limit during the rotation sequence at higher and lower elevations than Polaris. This usually means observing with the telescope that is not centered within the inner cradle. Table 10-1 shows the UT date and start time of the tests, the HIPO image numbers, the coarse drive elevation, the FBC activation status and the star identifier of the star observed in HIPO.

Table 10-1. FBC verification test summary.

Date UT	UT Start	HIPO OS	CD [°]	FBC ON/OFF	Star ID
20081213	05:40:55	97-103	24.9	OFF	HD 141652
20081213	05:57:35	109-115	24.9	ON	HD 141652
20081213	06:34:49	128-134	35.7	OFF	HD 5914
20081213	06:40:10	137-143	35.7	ON	HD 5914
20081213	06:53:11	145-151	43.0	OFF	HD 24126
20081213	06:58:03	154-160	43.0	ON	HD 24126
20081213	07:22:11	162-168	52.0	OFF	BD +72238
20081213	07:27:06	171-177	52.0	ON	BD +72238

Following parameters/operation conditions were chosen for the entire test time:

- The implemented alignment matrix during the entire run is alignment matrix #5 (see TC-HIPO-06).
- The rotation angle for all LOS rotation is 3.75°, while 6 moves are performed per elevation and per FBC status.
- All HIPO images were taken with a 2 sec exposure time.
- FPI images at 25°, 43° and 52° were taken with a 1 sec exposure time, at 35° with 2 sec. FFI and WFI images were taken with a 2 sec exposure time. All imager filters were set to filter position 6 (open).
- The reference acceleration vector that was implemented during the run is [-0.17 8.00 -5.61]. The acceleration vector is measured during a previous LOS alignment maneuver at a Coarse Drive elevation of 35°. The orientation of TARF with respect to the telescopes inner cradle was not considered during its read out.

The selected stars were too faint for the WFI. No centroids were calculated and recorded for the selected stars. However, the FBC correction is not significant for WFI.

Data Analysis:

The data analysis is performed analogue to the LOS gyroscope alignment analysis in TC-HIPO-06. A detailed description of the analysis approach can be found in [4]. There are four steps in the data processing scheme for which LOS turning points are calculated:

5. Raw centroid data
6. Apparent drift is corrected
7. Existing control deviation added to raw data
8. Existing control deviation added to raw data and residual drift corrected. The drift value for each axis is estimated such that the RSS of the centroid standard deviations at each LOS motion limit is minimized.

The first two steps were evaluated on-site shortly after the test to provide quick look analysis and sanity check of the measurements. The later two were added in order to find explanations for the apparent high drift values.

Results:

In order to verify proper functionality of the FBC algorithm, measured accelerations and the applied corrections are verified when FBC is turned on.
The measured accelerations which reflect on ground the components of the gravity vector are shown in Figure 10-2. They are compared to the expected accelerations which are calculated using the telescope's Coarse Drive elevation and the Spherical Sensors read out (orientation with respect to the Inner Cradle).

As expected, the XEL and LOS components of the acceleration vector are changing greatly when changing the telescope's elevation. The EL component of the acceleration vector does not change over the elevation range but changes can be clearly seen over the 3.75° LOS rotations.

The results show that there are minor differences in the measurements and the simulated values due to small calibration errors and misalignments of the accelerometers, the Coarse Drive and the Spherical Sensors. In addition, it was assumed for the calculation that the airplane is leveled. The average values of the acceleration offsets for each axis are approximately:

EL	-0.077 m/s^2
XEL	0.036 m/s^2
LOS	0.060 m/s^2

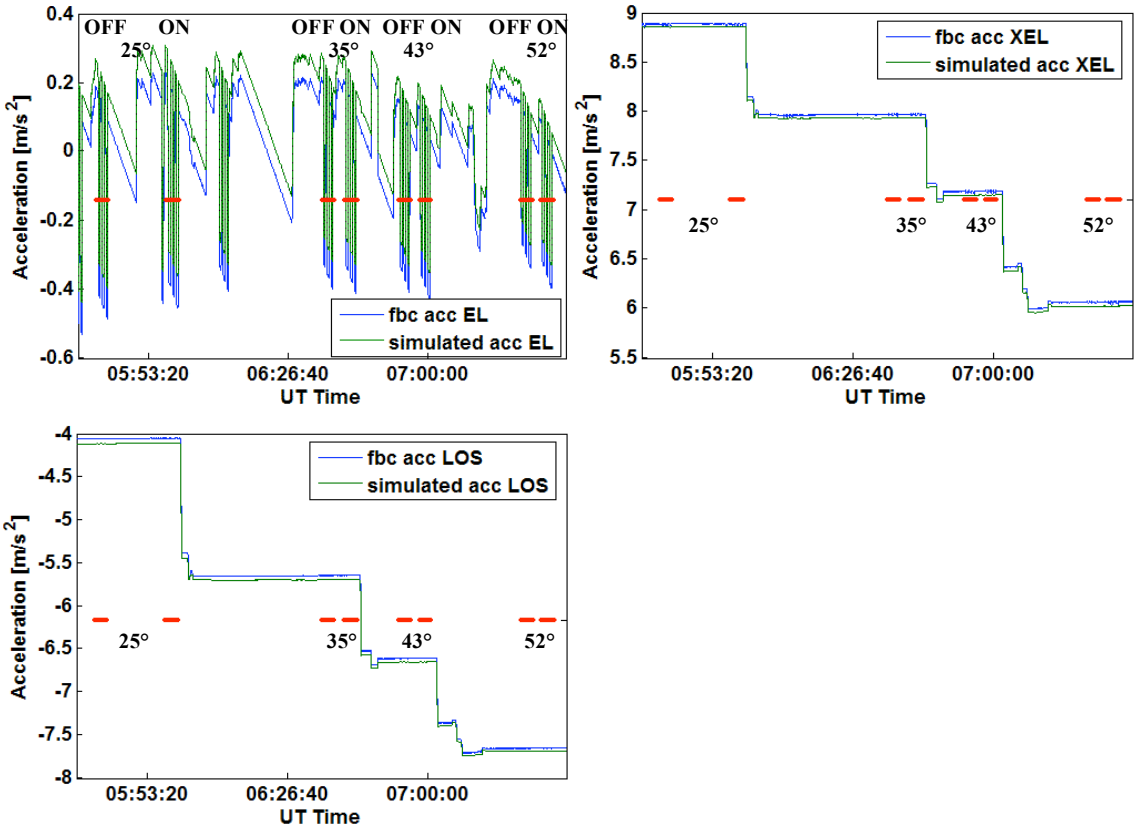

Figure 10-2. Measured and simulated accelerations in EL, XEL and LOS during FBC test. Red points indicated the time at which HIPO images are taken.

The according FBC corrections that were applied when FBC was turned on are based on the measured accelerations (orientation of gravity vector) and the equations (10-1) and (10-2). The corrections that were applied during the entire test at different elevations to the Fine Drive position loop are shown in Figure 10-3. As mentioned before, the major part of the correction takes place in XEL-direction.

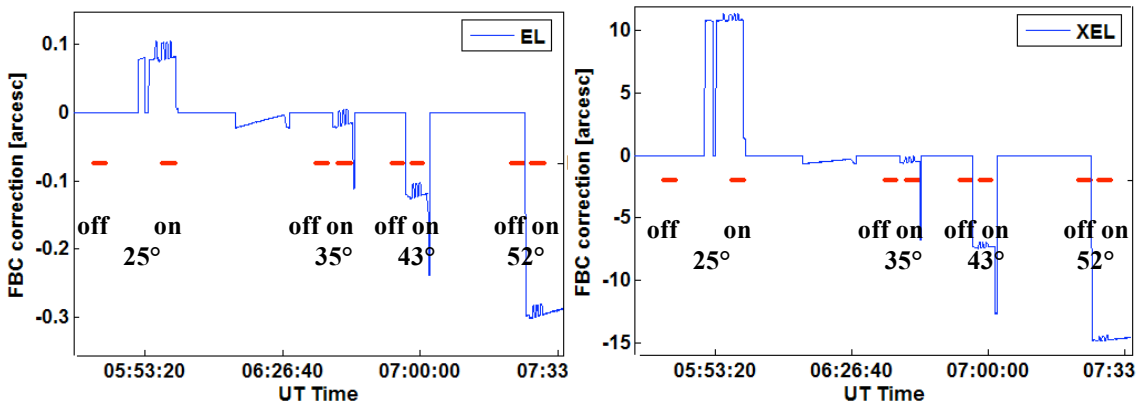

Figure 10-3. Applied EL (left side) and XEL (right side) correction during FBC test.

It is noticeable that pointing errors are introduced when performing LOS rotations within the Fine Drive motion range. Figure 10-4 shows the applied FBC corrections (and thus the theoretically expected image motion) for the LOS alignment maneuver at 35.7°. The corrections (respectively image motion) are caused by the above mentioned change of acceleration in EL during the 3.75° LOS rotation.

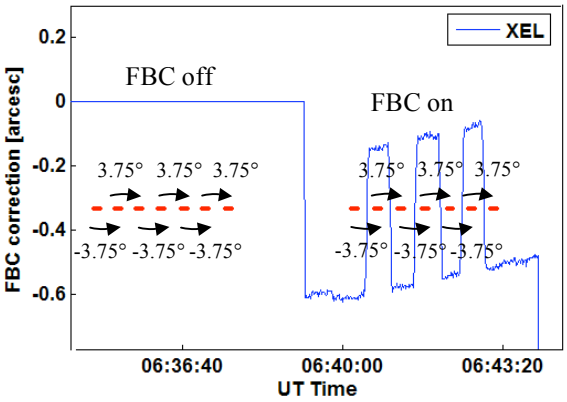

Figure 10-4. Applied XEL correction during FBC measurement at 35.7°. The FBC correction is based on the FE model. When FBC is off, no correction is applied. When FBC is on, a correction of about 0.5 arcsec is applied when performing the 3.75° LOS maneuvers.

This leads to a different pointing correction at the two LOS motion limits. For this example, the pointing difference in XEL is about 0.5 arcsec which equals about 1.5 pixels in HIPO. A difference of 1.5 pixels of the centroid location at the LOS limits is interpreted within these test evaluations as a misalignment of the gyroscopes. In addition to the measurement noise, this might be an explanation why the LOS gyro alignment in TC-HIPO-06 did not converge to a consistent result.

Table 10-2 lists the calculated LOS turning points for the FBC measurements. The results that are corrected for control deviation and drift are shown in Figure 10-5 and 10-6.

Table 10-2. LOS turning points in HIPO pixels with standard deviations for different elevations while FBC ON and OFF. The lower section of the table shows the differences of these turning points to the flange center in EL and XEL-direction in arcsec.

CD [°]	Data processing status	FBC OFF Turning points [pixel]		FBC OFF Std dev [pixel]		FBC ON Turning points [pixel]		FBC ON Std dev [pixel]	
		X	Y	σ_X	σ_Y	X	Y	σ_X	σ_Y
24.9	Raw data	554.7	490.8	30.6	15.1	528.6	462.9	22.0	18.5
	Drift corrected	554.5	488.9	28.1	15.0	525.5	460.8	17.8	12.6
	Control deviation added	547.3	493.2	32.8	16.0	523.4	464.7	22.9	20.4
	Control dev added and drift	547.0	491.2	30.0	15.6	520.2	462.5	18.0	14.1
35.7	Raw data	566.0	467.7	21.2	30.9	546.8	450.5	14.5	25.0
	Drift corrected	563.5	467.4	20.6	30.6	543.6	451.1	12.2	19.2
	Control deviation added	557.2	469.6	18.2	30.2	536.1	453.7	13.6	23.6
	Control dev added and drift	554.6	469.0	17.7	30.1	533.1	454.4	11.2	17.5
43.0	Raw data	586.5	453.6	22.4	8.1	543.3	452.3	10.4	15.5
	Drift corrected	584.7	454.9	18.8	2.1	541.5	451.7	9.6	14.7
	Control deviation added	571.5	461.6	20.4	9.1	525.8	461.0	14.3	14.8
	Control dev added and drift	569.6	462.7	17.3	3.3	523.8	460.2	13.4	13.7
52.0	Raw data	575.9	423.8	17.2	25.8	551.6	446.6	16.9	18.5
	Drift corrected	575.4	423.2	17.4	25.7	553.6	450.4	17.9	18.8
	Control deviation added	559.3	434.0	14.2	25.6	537.1	457.2	15.7	22.4
	Control dev added and drift	558.7	433.1	14.4	25.4	535.0	457.9	15.4	17.8

CD [°]	Data processing status	FBC OFF Delta to center [arcsec]		FBC OFF Std dev [arcsec]		FBC ON Delta to center [arcsec]		FBC ON Std dev [arcsec]	
		ΔEL	ΔXEL	$\sigma_{\Delta EL}$	$\sigma_{\Delta XEL}$	ΔEL	ΔXEL	$\sigma_{\Delta EL}$	$\sigma_{\Delta XEL}$
24.9	Raw data	-5.2	-0.8	7.4	8.3	7.3	-0.1	6.5	6.7
	Drift corrected	-4.6	-1.1	7.0	7.7	8.5	0.3	4.9	5.2
	Control deviation added	-4.2	1.6	8.0	8.9	8.0	1.6	7.0	7.2
	Control dev added and drift	-3.6	1.3	7.4	8.2	9.2	2.0	5.2	5.4
35.7	Raw data	-1.7	-8.5	8.9	8.4	6.6	-7.2	7.0	6.4
	Drift corrected	-1.1	-7.9	8.8	8.2	7.1	-6.3	5.4	5.0
	Control deviation added	-0.4	-5.8	8.5	7.8	8.0	-3.9	6.6	6.0
	Control dev added and drift	0.3	-5.3	8.4	7.7	8.5	-3.0	5.0	4.6
43.0	Raw data	-2.5	-16.5	5.1	5.9	6.9	-6.0	4.5	4.2
	Drift corrected	-2.4	-15.8	4.0	4.7	7.4	-5.6	4.2	3.9
	Control deviation added	-1.3	-11.1	4.8	5.5	8.4	0.3	4.8	4.7
	Control dev added and drift	-1.2	-10.4	3.7	4.4	9.0	0.6	4.4	4.4
52.0	Raw data	7.2	-20.1	7.4	6.9	6.6	-9.3	5.8	5.7
	Drift corrected	7.5	-20.1	7.4	6.9	5.2	-9.0	6.0	6.0
	Control deviation added	8.2	-13.8	7.1	6.4	7.0	-3.4	6.5	6.1
	Control dev added and drift	8.5	-13.8	7.1	6.4	7.2	-2.7	5.5	5.4

Figure 10-5 shows the calculated LOS turning points as projected on the HIPO CCD. The data is corrected for control deviation and drift (data analysis step 4). The flange center at the designated HIPO pixel (TC-HIPO-01) is indicated as a small black cross at X_0=542.8 and Y_0=480.2. This is the desired location for the LOS turning point. For consistency check, the result of the LOS alignment measurement with 3.5° that was performed after the FBC test series is shown in light grey. Assuming a centroid measurement error of about one pixel (1σ), the alignment error of the procedure is approximately 7 arcsec, respectively 20 HIPO pixels. However, repeating the maneuver six times should reduce this number to 3 arcsec, respectively 9 HIPO pixels.

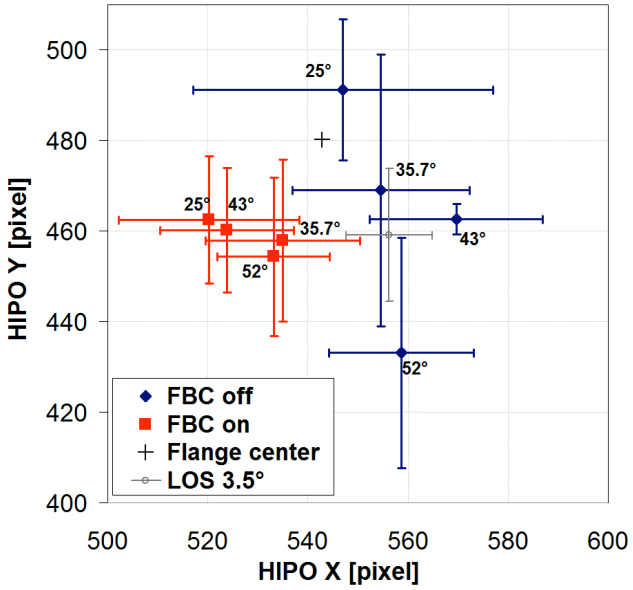

Figure 10-5. LOS turning points in HIPO pixels while FBC is turned on and off at different Coarse Drive elevations, data are corrected for control deviation and drift.

The spread of the LOS turning points over the elevation range when FBC is turned off is reduced greatly when FBC is turned on. This indicates that the implementation of the quasi-static FBC is working properly.

If the system would have been perfectly aligned at 35°, all LOS turning points (FBC on) and the turning point at 35°(FBC off) should be projected at the flange center location. However, the turning points are offset despite the fact that various alignment iterations at 35° were performed before the FBC tests. One reason for these offsets is the slowly converging control deviation which was not accounted for during the on-site analysis. Another reason is the pointing difference caused by differential flexure over the 3.75° maneuver rotations which are corrected when FBC is turned on.

Figure 10-6 shows the differences of the turning points to the flange center in EL- and XEL-direction in arcsec. When FBC is turned on, the average difference of the turning points to the flange center is about ΔEL = 8.5 arcsec and ΔXEL = -0.8 arcsec.

The measurements are compared to the expected test results of the FE model. In Figure 10-6, the FE prediction data is offset such that the sum of the squared differences to the measurement points (FBC off) is minimized. For an alignment at 35°, the offset of the FE prediction curve is at ΔEL_0 = 0.9 arcsec and ΔXEL_0 = -4.1 arcsec. The data suggest very crudely that the telescope structure is slightly stiffer than reflected in the FE model as the image motion seems to be smaller than predicted.

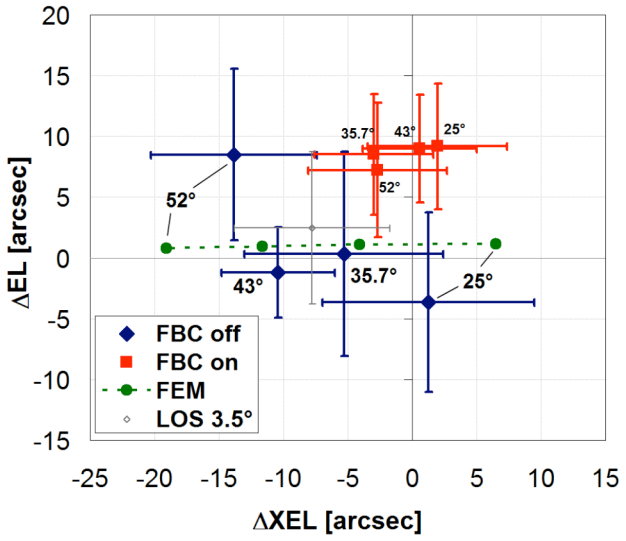

Figure 10-6. LOS turning point differences to flange center in arcsec, data are corrected for control deviation and drift. The FE model predictions are shown in green.

Conclusions:

The test results show that in first order, the quasi-static FBC is working properly. One of two usable FBC coefficients could be quantitatively assessed. However, FBC coefficient calibration is not recommended with the measured data set as the calibration capability is limited by the error of the procedure. In addition, the test analysis revealed that differential flexure over the LOS rotation within the Fine Drive motion limit affects the LOS gyro alignment.

Next Steps:

The following steps are suggested in no particular order.

1. Calculate FBC coefficients with updated FEM model.
2. Use only two of the six coefficients in the implementation to avoid complication.
3. Re-align accelerometers (data might be already available).
4. Check FFI centroids for quality and if not useable, repeat measurement for FFI. Defocus FPI and take much brighter stars. Ignore corrections for WFI in implementation.
5. Test the FBC in flight.

References:

[3] SOF-SPE-MG-5200.0.04 Appendix G, FBC analysis, 30.06.2000

[4] Martin Süß: SOFIA: Implementation of quasi-static FBC, Technical Note, 08.06.2004

[5] Martin Süß: SOFIA: Implementation of the imager displacements values, Technical Note, 25.05.2004

[6] Franziska Harms et al.: On sky testing and preliminary sensor alignment for the SOFIA telescope, Astronomical Telescopes and Instrumentation, Proceedings SPIE Vol. 6267, May 2006